THE THESIS COMMITTEE FOR REBEKAH ELIZABETH SIMON
CERTIFIES THAT THIS IS THE APPROVED VERSION OF THE FOLLOWING THESIS:

SYNDEPOSITIONAL FAULT CONTROL ON DOLOMITIZATION OF A STEEP-WALLED CARBONATE PLATFORM MARGIN, YATES FORMATION, RATTLESNAKE CANYON, NEW MEXICO

APPROVED BY
SUPERVISING COMMITTEE:

Supervisor:

Charles Kerans

Co-Supervisor:

Christopher Zahm

Daniel Breecker

SYNDEPOSITIONAL FAULT CONTROL ON DOLOMITIZATION OF A STEEP-WALLED CARBONATE PLATFORM MARGIN, YATES FORMATION, RATTLESNAKE CANYON, NEW MEXICO

BY

REBEKAH ELIZABETH SIMON, B.S.

THESIS

Presented to the Faculty of the Graduate School of

The University of Texas at Austin

in Partial Fulfillment

of the Requirements

for the Degree of

MASTER OF SCIENCE IN GEOLOGICAL SCIENCES

THE UNIVERSITY OF TEXAS AT AUSTIN

DECEMBER, 2014

ACKNOWLEDGEMENTS

I owe the completion of this thesis to the support and patience of advisors, family, and friends. First, I would like to extend heartfelt thanks to my advisors, Charlie Kerans and Chris Zahm, for sharing their wealth of experiences, both in life and in geology, and for their tireless efforts to help me define and complete a fulfilling research project. They have both provided me with tremendous opportunities to advance my geologic knowledge and introduced me to a world-class research organization that I both respect and admire. I also owe thanks to the members of the RCRL research consortium for their financial support, to Renee West and the National Park Service for facilitating research in Carlsbad Caverns National Park, and to the familiar faces at the BEG, including Harry Rowe and company, Stephaine Lane, and the CRC Crew for making all the dirty work a little bit easier.

I benefitted from technical conversations with Rob Forkner, Ned Frost, and John Humphrey, and appreciated being able to brainstorm with my peers including Ben Tanner, Ben Smith, Maren Mathisen, Andrea Nolting, Reed Roush, Katie Fry, Kris Voorhees, and Greg Hurd, as well as the entire student membership of the RCRL consortium.

Lastly, family and friends were welcome distractions during the most intense moments, offering jokes, consolation, encouragement, and funny YouTube videos as the situation demanded. I am eternally grateful that they leant a helping hand, and they will forever have my gratitude.

ABSTRACT

SYNDEPOSITIONAL FAULT CONTROL ON DOLOMITIZATION OF A STEEP-WALLED CARBONATE PLATFORM MARGIN, YATES FORMATION, RATTLESNAKE CANYON, NEW MEXICO

Rebekah Elizabeth Simon, M.S. Geo. Sci.

The University of Texas at Austin, 2014

Supervisors: Charles Kerans, Christopher Zahm

Syndepositional deformation features are fundamental components of carbonate platforms both in the subsurface and in seismic-scale field analogs. These deformation features are commonly opening-mode, solution-widened fractures that can evolve into extensional faults, and reactivate frequently through the evolution of the platform. They also have potential to behave as fluid flow conduits from the earliest phases of platform growth through burial and uplift, and can be active during hydrocarbon generation. As such, diagenetic alteration in the margins of these carbonate platforms is often intense, may demonstrate a preferential spatial relationship to the deformation features rather than the depositional fabrics of the strata, and may impact the permeability development of reservoir strata near deformation features.

This study focuses on a syndepositional graben known as the Cave Graben fault system in the Yates Formation of Rattlesnake Canyon in the Guadalupe Mountains, and

investigates the distribution of dolomite around the faults and associated opening-mode fractures, in an effort to understand the control the Cave Graben faults exert on fluid flow through the platform margins. Two generations of dolomite are identified on the outcrop: a fabric retentive dolomite located in the uppermost facies of the platform, and a fabric destructive dolomite that forms white, chalky haloes around syndepositional deformation features. The first generation of dolomite is dully luminescent and has very small crystal sizes, as well as a low trace element concentration and an ^{18}O-enriched stable isotopic signature compared to Permian marine carbonate ratios. This dolomite is interpreted to have formed from penecontemporaneous refluxing of a concentrated lagoonal brine, and shows little fault control on its distribution. The second generation of dolomite is brightly luminescent and has much larger crystal sizes, as well as a higher trace element concentration and a slightly ^{18}O-depleted isotopic signature compared to the first generation of dolomite, though it is still enriched in ^{18}O compared to Permian marine carbonate. This dolomite is interpreted to have formed in a burial environment due to the transport of concentrated brines from the overlying evaporites through syndepositional deformation features. Overall, this study suggests that, once open, syndepositional deformation features may become the primary fluid conduit through otherwise impermeable strata, and may control the distribution of diagenetic products over a long period of geologic time. It provides valuable insight into the interaction of syndepositional faults and fractures and fluid flow, and may improve understanding of diagenesis in analogous subsurface carbonates reservoir intervals.

TABLE OF CONTENTS

LIST OF TABLES

LIST OF FIGURES

CHAPTER 1 — INTRODUCTION

Carbonate rocks, due to their susceptibility to fluid-rock interaction, commonly exhibit diagenetic histories that can be attributed to a unique diagenetic history, and that may strongly impact their reservoir quality. This study, using outcrops of the Permian Reef Complex in Rattlesnake Canyon, Guadalupe Mountains, New Mexico, examines one example of a complex porosity network in the margin of a steep-walled carbonate platform that can be largely attributed to the presence of margin-parallel syndepositional faults and fractures. The study makes an effort to understand the effects these faults and fractures have on fluid flow and diagenesis through geologic time, with a particular focus on dolomitization across a shelf and reef outcrop window approximately 500 meters wide. This outcrop window was chosen specifically because it contains a 150-meter-wide syndepositional graben with hundreds of associated syndepositional fractures. It is also a unique opportunity to observe the interplay between syndepositional deformation, facies with a wide variety of depositional fabrics and textures, and the distribution and timing of dolomitization.

Using a combination of field mapping, petrographic determination of cement paragenesis, cathodoluminescence microscopy, stable istotope analysis, and trace element analysis, a qualitative model for the dolomitization of the Yates Formation shelf and reef strata is proposed. This model will be compared to two existing models for dolomitization in other Guadalupian strata, including Tansill age strata in Dark Canyon (Frost et al., 2012), and Seven Rivers to Yates age strata in the southern portion of the Guadalupe Mountains (Melim, 1991). These comparisons will contribute to a quickly growing body of knowledge surrounding the impacts of syndepositional deformation on fluid flow, and will determine whether faults and fractures control dolomitizing fluids in

the Yates Formation in a similar manner as proposed for other strata in the Guadalupe Mountains, despite differences in stratigraphic architecture and facies proportions.

Recognition of syndepositional fault and fracture systems in numerous classic platform outcrops spanning diverse geologic settings has proliferated in the last three decades. Key examples include the Devonian (Frasnian, Fammenian) reefs of Australia's Canning Basin (Frost, 2007; George et al., 2009; Frost and Kerans 2009, 2010), the Upper Carboniferous Cantabrian Mountains of Northern Spain, (Della Porta et al., 2004) the Permian (Guadalupian) Guadalupe Mountains of West Texas and New Mexico (Hunt et al., 2002; Koša et al., 2003; Stanton and Pray, 2004; Koša and Hunt, 2005, 2006a, b; Frost et al, 2012; Jones, 2012; Budd et al., 2013, this study), the Triassic (Carnian) buildups of northern Italy's Dolomite Range in the Southern Alps (Cozzi, 2000), and the Pleistocene to Holocene of the Bahamas (Daugherty, 1986; Smart et al., 1987; Aby, 1994, Whitaker and Smart, 1997) and the Turks and Caicos Islands (Guidry et al., 2007). The prolific nature of such faults and fractures makes it increasingly apparent that early deformation is a fundamental component of platform margin development, and many recent studies have thus begun to investigate the role this deformation plays in the diagenetic evolution of carbonate platforms.

In the Guadalupe Mountains, Melim and Scholle (1989) and Melim (1991) identified pervasive dolomitization of the forereef slope facies in the southern portion of the range, and attributed this dolomite to the transport of mesosaline brines through the impermeable reef via syndepositional fractures and solution-widened fault zones, while Frost and others (2012) and Budd and others (2013) documented similarly fractured and dolomitized outer shelf strata at the northern portion of the range. The northern portion of the Guadalupe Mountains also boasts solution-widened faults, many of which contain

variable fill and show multiple episodes of karstic dissolution, cementation, and dolomitization. These features are commonly expressed as paleocaverns, such as those in Slaughter Canyon (Hunt et al., 2002; Koša and Hunt, 2005, 2006a, 2006b; Koša et al., 2003; Koša et al., 2000), and it is suspected that the Carlsbad Caverns themselves are the result of Tertiary preferential dissolution along syndepositional (Permian) faults and around dolomitized strata (Hill, 1996, 1999; Kerans et al., 2012). Structural control on cave formation is not uncommon; karstic dissolution of fractures has also resulted in cave formation in several modern analogs including islands of the Turks and Caicos (Guidry et al., 2007) and many islands on the Bahamas (Aby, 1994; Whitaker and Smart, 1997).

With the understanding that syndepositional structural elements can exert a strong control on the diagenesis of platform margins, in several ways and across a geologically significant period of time, one must consider the implications these features create for reservoir quality. Several major hydrocarbon-producing carbonate platforms, including the Tenghiz platform of Kazakhstan, are syndepositionally fractured, and the fractures exert strong control on reservoir production (Carpenter et al., 2006; Narr et al., 2008). While this study will not directly examine the relationship of reservoir properties to syndepositional deformation, it will address the spatial and temporal relationships between diagenetic products around a syndepositional graben in the Yates Formation of Rattlesnake Canyon which will serve as a proxy for the porosity and permeability network through time, and may act as an analogue for subsurface reservoirs in similar strata.

GEOLOGIC SETTING

The mixed carbonate-clastic Leonardian to Guadalupian age platform that makes up the Guadalupe Mountains has been of interest to carbonate geologists for over sixty years following the seminal works of Philip B. King (1942, 1948). The Guadalupe Mountains are located on the northwest margin of the Delaware Basin (Figure 1), following deposition at roughly 5° paleolatitude, and exhumation by Basin and Range uplift and NNW-SSE normal faulting. Many high angle extensional faults currently define the southwestern border of the range, which wraps around the perimeter of the Delaware Basin for approximately fifty kilometers, however, the north and east sides of the Guadalupe Mountains remain largely unmodified by tectonic structures. Instead, numerous erosional dip-oriented canyons bisect the shelf margin, providing outstanding access to continuous, kilometer-scale shelf-to-basin exposures that, in total, represent approximately twenty million years of platform growth and development (Kerans and Kempter, 2002). Across the shelf, a slight, 1-2° regional dip to the northeast conveniently exposes increasingly younger strata towards the north (King, 1948).

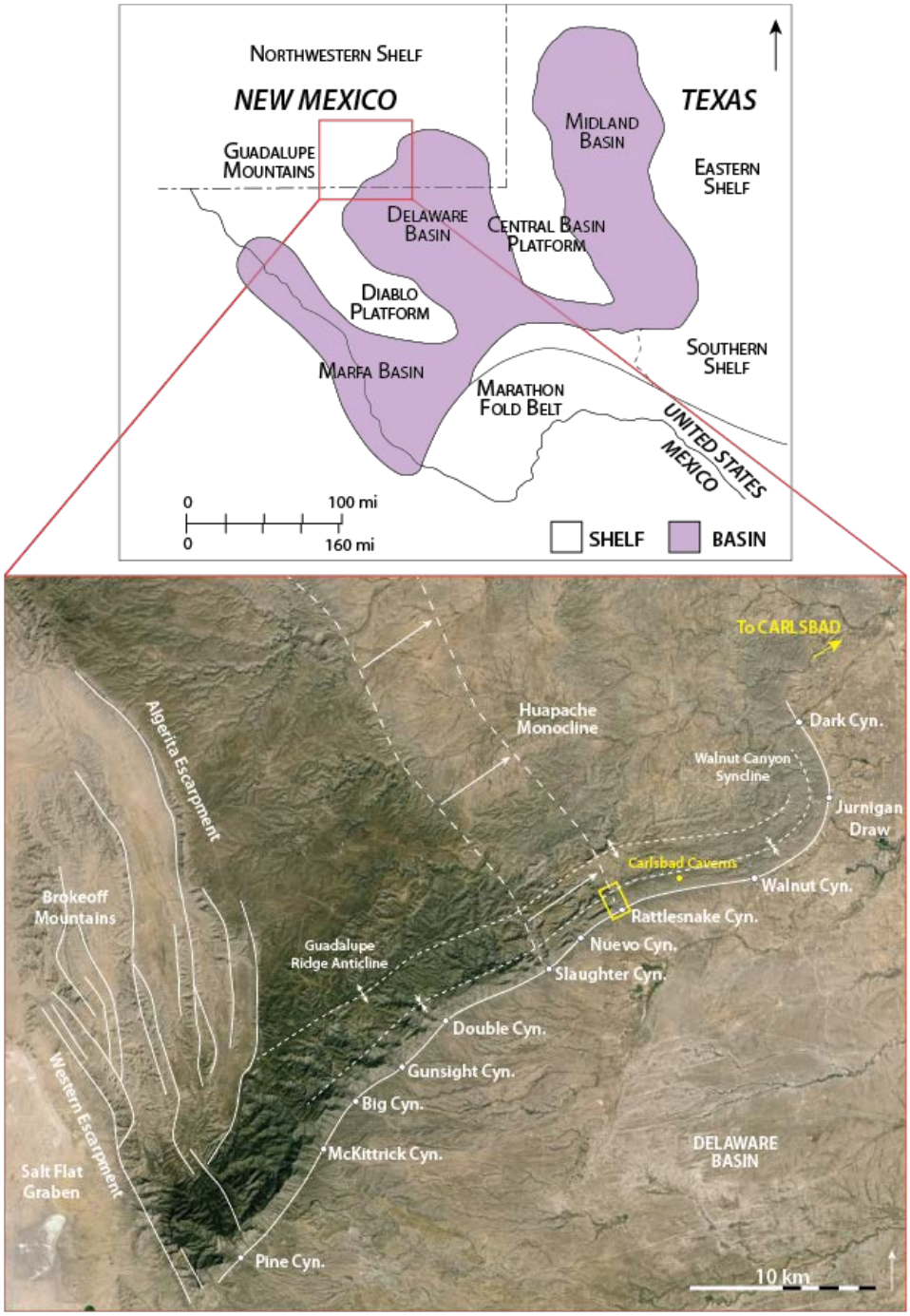

Figure 1: Location map for the Guadalupe Mountains. (Top) Permian Basin map, with approximate extent of Guadalupe Mountains outlined in red. After Saller et al. .(1999). (Bottom) Guadalupe Mountains satellite photo. Major structural elements are outlined in white, and major canyons ("Cyn.") denoted by white dots. Study area boxed in yellow. After Frost et al., (2012), photo from Google Earth (2014).

The Delaware Basin is the western sub-basin of the Permian Basin, a complex foreland basin system that developed during the late Mississippian Marathon-Ouachita orogeny along pre-existing basement thrust faults and lineaments. During the orogeny, the Central Basin Platform lifted relative to both the Delaware Basin and its eastern partner, the Midland Basin, until the cessation of motion in mid-Wolfcampian time; however, by Late Guadalupian time, bathymetric relief in the Midland Basin had disappeared beneath substantial sedimentation, and the Delaware Basin deepened asymmetrically to the east making its shallow western rim a prime environment for platform/reef growth (Ye et al., 1996). Throughout the duration of platform growth, the depositional profile in the Guadalupe Mountains progressed from a shallowly dipping, ramp-like geometry of the San Andres and Grayburg formations in Leonardian to early Guadalupian time, to the well-developed, reef-rimmed Capitan platform with extensive syndepositional fault and fracture networks of the Seven Rivers, Yates, and Tansill Formations in the middle to late Guadalupian (Kerans and Kempter, 2002; Kerans and Tinker, 1999). For the purposes of this study, two high-frequency sequences, the G24 (Corral) and G25 (Hairpin), in the reef-rimmed Yates Formation will be studied (Figure 2). These high frequency sequences represent the Capitan during a time when it was a shallow, open marine system with a combination of marine environments, and restricted zones of siliciclastics and evaporites inland of the reef itself.

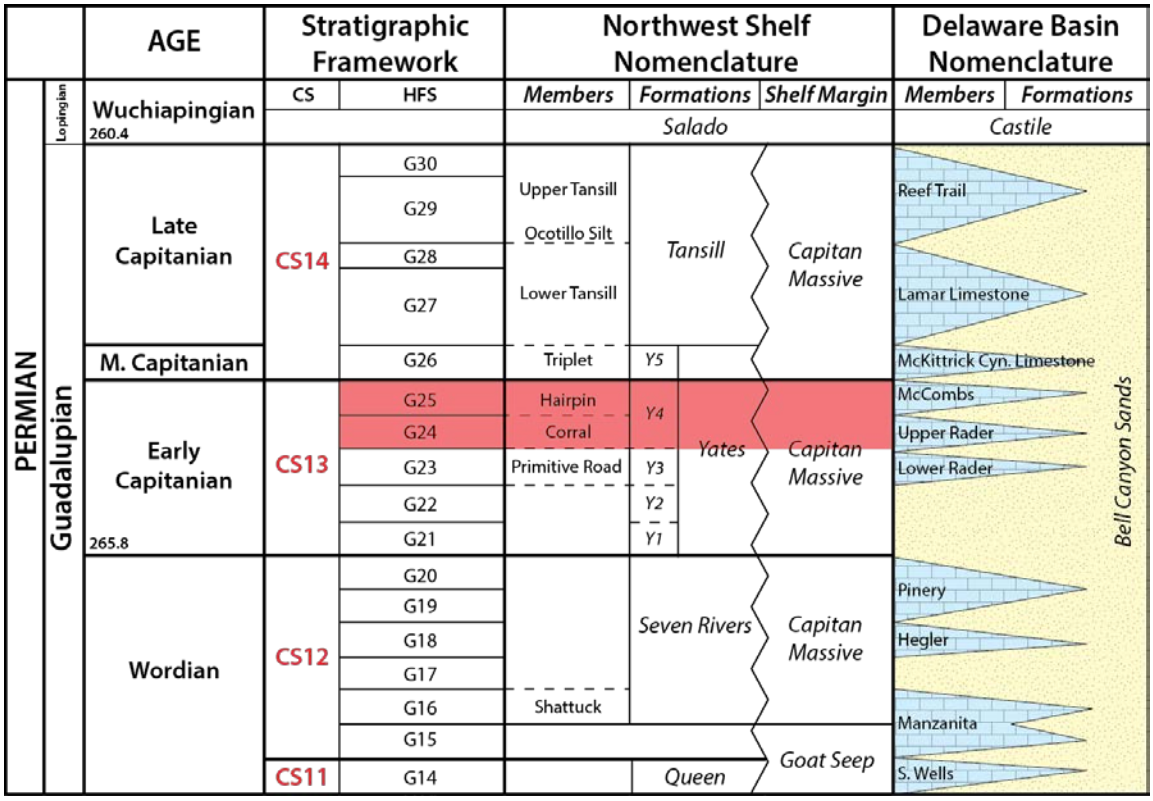

Figure 2: Simplified stratigraphic chart for the Guadalupe Mountains (Northwest Shelf) and the equivalent basinal members. This study will focus on two high frequency sequences, the G24 "Corral" and G25 "Hairpin" members of the Yates Formation (highlighted in red). Composite sequence (CS) and high frequency sequence (HFS) stratigraphic framework after Kerans and Tinker (1999), Rush and Kerans (2010); member nomenclature after Esteban and Pray (1977); figure modified from Rush and Kerans (2010), Harman (2011), Frost et al. (2012). Depositional Environment

The Permian Reef Complex in the Guadalupe Mountains is a unique, mixed carbonate/clastic environment that is generally accepted to represent a marginal mound depositional setting (Dunham, 1972), though certain aspects of that particular argument are still in question—for a brief summary on controversies about the Guadalupe Mountains, see Saller et al., (1999), and Tinker (1998). The marginal mound model, as portrayed schematically in Figure 3 below, transitions from a very shallow lagoon containing fine clastics and evaporites, through a shelf crest belt of elevated peritidal

algal/pisolitic “tepee” structures, into a shallowly dipping outer shelf zone of local ooids, coated grains, and skeletal debris, and finally over the shelf margin reef into megabreccia slope deposits and basinal muds/clastics. Most of these facies tracts have been described in detail in previous works (Assereto and Kendall, 1977; Dunham, 1972; Neese, 1989; Yurewicz, 1976). Exposures of the G24 (“Corral”) and G25 (“Hairpin”) members of the Yates Formation in Rattlesnake Canyon contain the shelf crest, foreshore/outer shelf, and reef portions of the depositional profile.

These carbonate facies dominate the platform top during the highstands and transgressions of sea level. However, sedimentation in the Guadalupe Mountains is cyclic: during sea level lowstands, siliciclastic material that had been trapped in the platform interior/”middle shelf” behind the raised tepee belt prograded across the shelf via a process that has been termed “reciprocal sedimentation” (Meissner, 1972). In the Yates Formation, this has resulted in high frequency cycles bounded by beds of sand, the thicknesses of which may indicate constructive interference of Milankovitch-scale sea level cycles (Borer and Harris, 1989, 1991). Eustacy is not the only control on facies partitioning, however. Though previous studies have argued that the dip of the shelf is depositional and that facies tracts are controlled by sea level (Kerans and Tinker, 1999), recent work provides evidence to suggest that syndepositional deformation exerts strong control on the stratigraphic architecture of the shelf as well (Harman, 2011; Hunt et al., 2002). The following sections will summarize the current understanding of syndepositional faulting and fracturing, and how they influence stratigraphy, platform morphology, diagenesis.

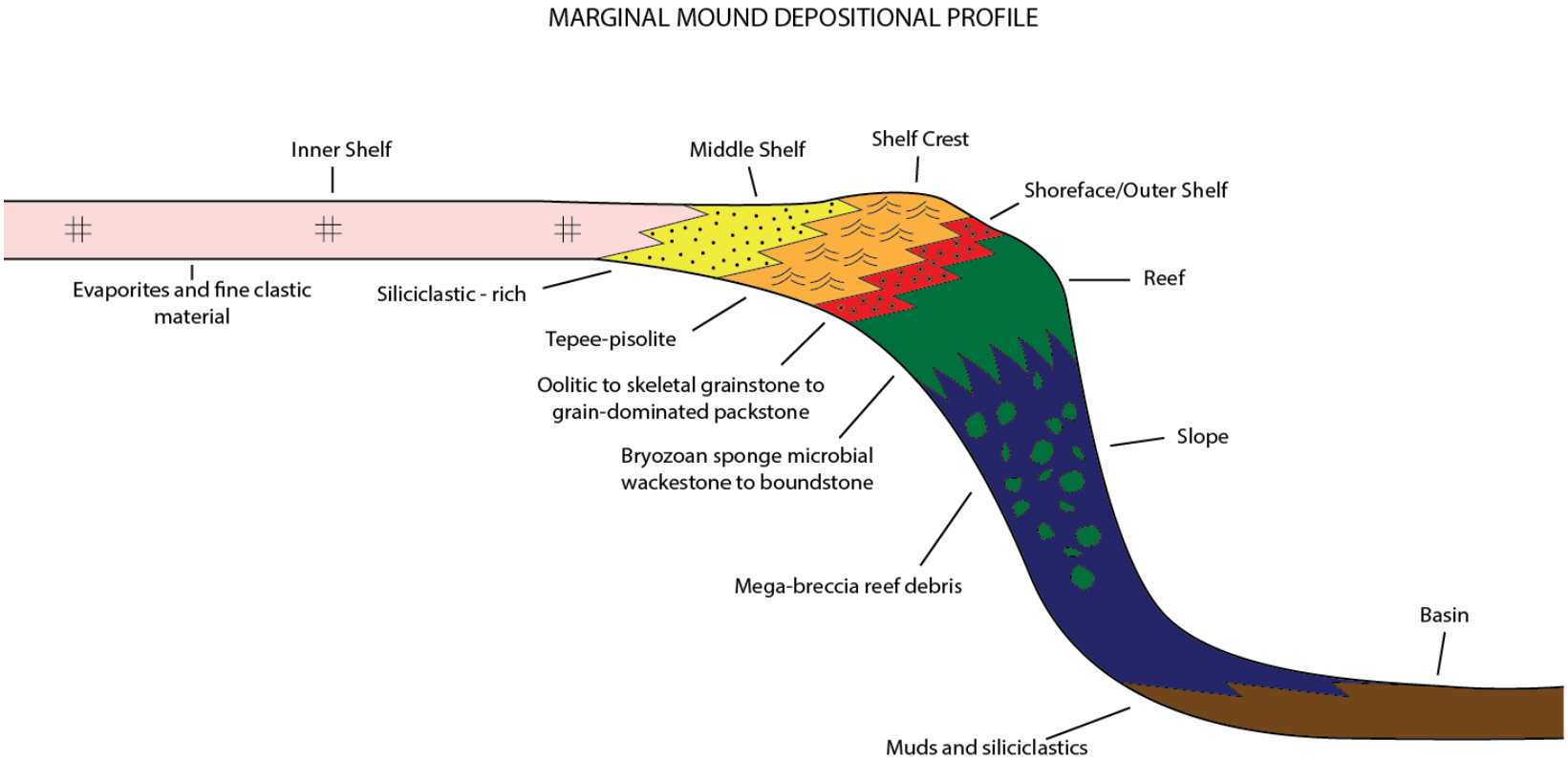

Figure 3: Schematic representation of a marginal mound depositional profile, modified to reflect the constituent grains observed in Rattlesnake Canyon. After Kerans and Tinker (1999).

SYNDEPOSITIONAL DEFORMATION

Syndepositional faults and fractures are common in a variety of steep-walled carbonate platforms in both modern settings and ancient outcrops, and their formation is a fundamental aspect of the development of carbonate platforms. Substantial research has been done over the last several decades on the formation of syndepositional deformation features and the impact they have on platform geometry, facies distribution, and mechanical evolution.

Deformation Mechanisms and Stratigraphic Relationships

Three such examples include recent work on the relationships between syndepositional deformation and sequence stratigraphy in the Devonian (Frasnian/Fammenian) reefs of Australia's Canning Basin (Frost, 2007; Frost and Kerans, 2009, 2010). Using shelf-margin trajectory as an approximation for stratigraphic architecture, Frost (2007) identified a statistically significant relationship between fracture development and highly progradational strata, which are generally early cemented and behave as a single mechanical unit with the potential for bed-scale heterogeneity. The same study also proposed three mechanisms for syndepositional fracturing: (1) gravity-driven instability and compaction, (2) differential compaction over antecedent topography, and (3) active tectonic deformation (Figure 4). It is noted that external drivers are not necessary for fault and fracture development, (Frost and Kerans, 2009) and that syndepositional deformation can occur via gravity-driven instability and/or compaction over antecedent topography alone. The graben in this study likely formed due to a combination of these two factors, as it is located immediately basinward of the G24 platform margin and is oriented roughly parallel to it; this placement suggests that the early-cemented, rigid G24 margin acted as an antecedent topographic high.

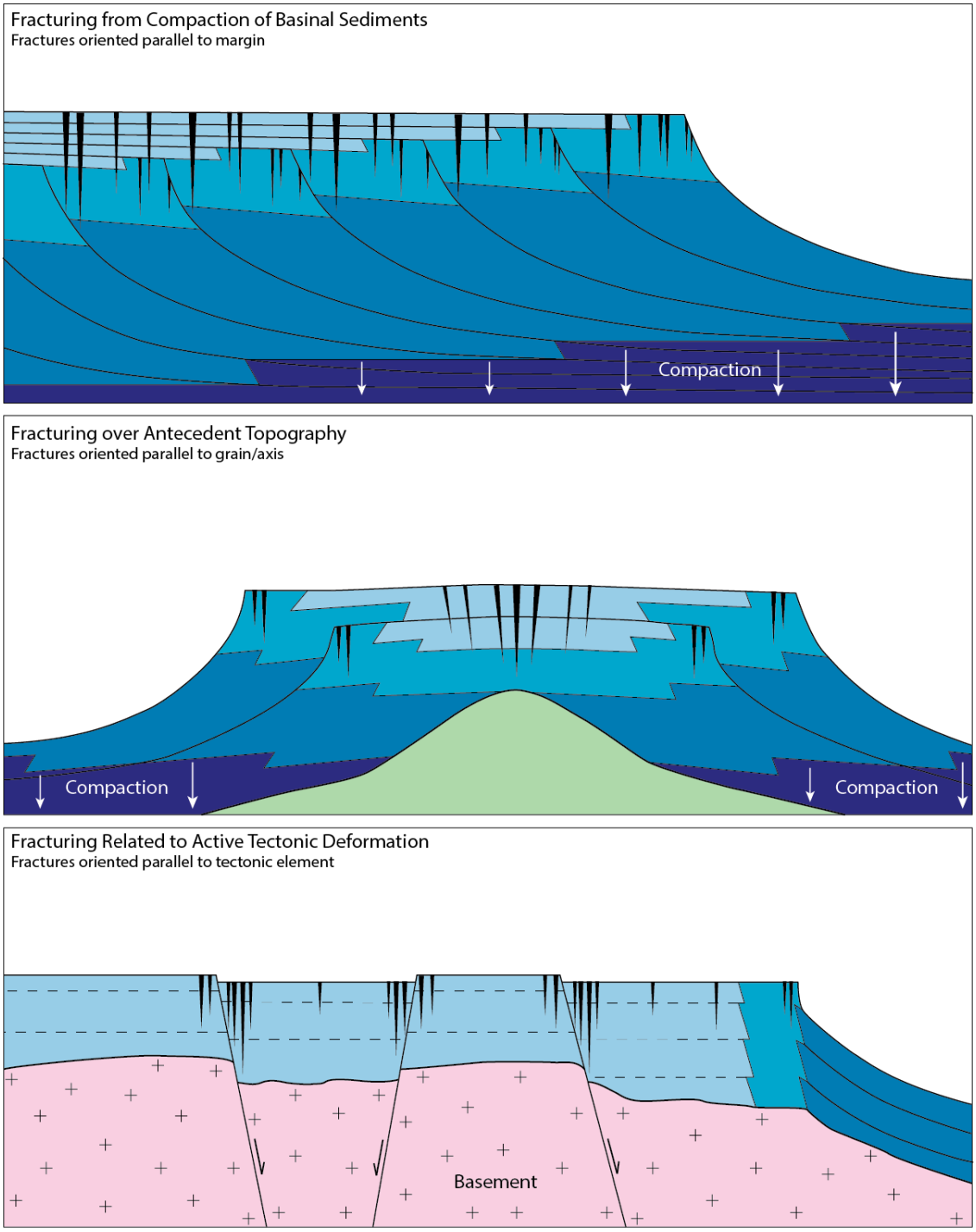

Figure 4: Conceptual models for syndepositional fracture development. (Top) Gravitational compaction of slope and basin sediments. (Middle) Flexure over antecedent topography. (Bottom) Fracturing around zones of active tectonic deformation. Modified from Frost and Kerans (2010).

In syndepositionally deformed strata, facies distribution and cycle thicknesses may be impacted by placement of syndepositional faults and fractures. Consider again the Guadalupe Mountains: in the G23-G26 of Slaughter Canyon, thickening and tilting of Yates strata were locally influenced by syndepositional faults (Hunt et al., 2002), though there was not a significant enough amount of bathymetric relief to dramatically modify the location of facies tracts (Harman, 2011). Similar facies thickening and tilting have been observed in the Yates Formation around syndepositional faults in Rattlesnake Canyon (Mathisen, in progress), and modified sedimentation patterns have also been attributed to syndepositional offset in the Tansill strata of Dark Canyon (Frost et al., 2012). This regionally extensive sedimentation response and modification of stratigraphic architecture suggests that even minor syndepositional deformation can have an impact on the stratigraphic development of the carbonate platform.

Syndepositional deformation can also create mechanical weaknesses that may modify the stratigraphy of the platform; a wide variety of platforms in both ancient and modern settings contain mass failure deposits that can be directly linked to the presence of syndepositional deformation features. In the Guadalupe Mountains, Tansill strata in the mouth of Walnut Canyon are one example of a major mass failure deposit, where oversteepened, failure-prone portions of the Capitan margin suffered mass wasting. These portions ultimately became zones of mechanical weakness that were reactivated over time and filled with siliciclastic material and breccias beyond what an uncompromised portion of the platform margin should contain (Rush and Kerans, 2010). Similarly, platform margins in both the Bahamas and Turks and Caicos Islands have orthogonal margin escarpments, where entire portions of the platform margin have not only tilted, but completely cleaved off along solution-dissolved syndepositional fractures (Aby,

1994). In both instances, what likely began as minor syndepositional offset evolved into a catastrophic event in the evolution of the platform that impacted future stratal geometries.

Syndepositional Deformation and Diagenesis

Stratigraphic modification to platform geometries due to syndepositional faulting and fracturing has the potential to influence porosity and permeability conditions of the margin, in addition to the enhanced fluid flow potential created by the faults and fractures themselves. Several recent studies have investigated the relationship between the morphology, mechanical character, and susceptibility to weathering and diagenesis in Slaughter Canyon, located in the Guadalupe Mountains nine miles southwest of Rattlesnake Canyon. Hunt and Koša studied clusters of syndepositional faults in various high frequency sequences of the Yates Formation, and determined that syndepositional faults in the Yates have a variety of expressions ranging from buried faults with no surface exposure to solution-widened paleocaverns containing multiple generations of the cementation and fill (Hunt et al., 2002; Koša and Hunt, 2005; Koša et al., 2003; Koša et al., 2000). These faults have been shown to influence speleogenesis in the Guadalupe Mountains (Hill, 1999; Koša and Hunt, 2006b; Koša et al., 2003).

Faults in Slaughter Canyon also have evidence for multiple episodes of diagenesis. Faults may be filled with clast-dominated or matrix-dominated breccias, and the clasts may be composed of siliciclastic material, carbonate material, or a combination of the two (Koša and Hunt, 2006a). Solution-widening, dolomitization, and late-stage spar precipitation of syndepositional fault zones are also visible to a varying degree across the outcrops (Koša and Hunt, 2006a; Koša et al., 2000). In many places, the diagenetic modification of the fault zones is so intense that fault properties are no longer

related to the orientation, aperture, or displacement of the faults; instead, fault properties are directly correlative to the dominant fill lithology (Koša and Hunt, 2006a).

Evidence of diagenetic modification of syndepositional fault zones can also be seen in Rattlesnake Canyon, in Yates and Tansill aged strata basinward from the location of this study. Here, many of the reef margins form "ridge-groove" couplets, which reflect a lower and higher fault and fracture intensity, respectively (Jones, 2012). These ridges and grooves are not depositional—rather, they reflect a relationship between early formed faults and fractures and geologically significant subsequent weathering and diagenesis.

Dolomite haloes up to several meters wide around syndepositional faults are also very common, both in shelfal and reef strata in Dark Canyon (Budd et al., 2013; Frost et al., 2012), and throughout the Capitan forereef in McKittrick Canyon, Bear Canyon, and Pine Canyon (Melim, 1991). These studies both provide evidence for fluid flow through syndepositional faults and fractures over a significant period of geologic time, suggesting that syndepositional faults and fractures are active permeability conduits through burial and hydrocarbon generation. The studies also note that the presence of syndepositional faults and their types of fill may become the dominant control on dolomitization, even more so than the original depositional fabric of the rocks themselves.

Controls on Fluid Flow

In addition to qualitative studies of fault and fracture controlled diagenesis, geochemical studies on modern fractured banks have given quantitative constraints to fracture controlled diagenesis. Research from South Andros Island of the Bahamas noted dissolution widening and cavern formation related to syndepositional fractures along the margin, attributed to enhanced tidal pumping and groundwater mixing in zones of deformation up to 200 meters away from fracture edges (Whitaker and Smart, 1997). The

authors identified salinity contrasts and variability in the dissolved fraction of CO_2 along the fracture walls and in the surrounding rock as the dominant control on dissolution, and measured rates of aragonite loss at up to 0.35% per thousand years, which is nearly twice the rate observed for normal freshwater lens mixing zones. Additionally, the study identifies a halo of diagenesis around the fractures that is remarkably similar in geometry to those observed in ancient strata (Whitaker and Smart, 1997). Both of these conclusions provide quantitative evidence that suggests syndepositional faults and fractures do create preferential fluid flow pathways nearly as soon as they open.

In combination, work done over the previous decades demonstrate that syndepositional deformation is a fundamental aspect of carbonate platform development, and may have influence on everything from facies distribution, to mechanical properties, to the evolution of porosity and permeability networks, to the distribution of both early and late diagenetic products. This study will contribute to this body of knowledge by studying the impact of syndepositional faulting and fracturing on dolomitization of a portion of the Yates Formation, and comparing the interpreted dolomitization model to existing dolomitization models for both older and younger strata that have different depositional characteristics.

DOLOMITIZATION MODELS

Before relating dolomite distributions to syndepositional faults and fractures, however, the four most widely-accepted mechanisms for dolomitization will be introduced. Dolomitization is widely recognized in the ancient rock record, and the Guadalupe Mountains are no exception, with dolomite-focused studies dating as far back as 1960 (Adams and Rhodes) and recognition of regional dolomitization even earlier (King, 1948; Newell et al., 1953). However, despite decades of field observations and

experimental laboratory work, a consensus has yet to be reached in the scientific community on the chemical and thermodynamic processes responsible for large-scale regional dolomitization, such as what can be observed in the Guadalupe Mountains. This "Dolomite Problem" is exacerbated by the lack of extensive dolomitization anywhere on the planet in modern carbonate settings. Despite lack of consensus, several hydrological mechanisms for regional dolomitization have been proposed and supported using field geometries, superposition relationships, isotopic signatures, and trace element geochemistry in ancient carbonates, including: (1) dolomitization by normal marine water, (2) dolomitization by refluxing brine, (3) dolomitization within a freshwater-seawater mixing zone, and (4) dolomitization from hydrothermal and basin-derived fluids. It is likely that one or several of these mechanisms are responsible for the extensive dolomitization in the Guadalupe Mountains and each will be introduced shortly below, preceding an in-depth evaluation in Chapter 4.

Normal Marine Dolomitization

Normal marine dolomitization operates on the condition that marine seawater is naturally oversaturated with respect to dolomite, and at a slightly elevated temperature, could be sufficient to generate large volumes of dolomite in carbonate platforms (Saller, 1984). One hydrologic mechanism for this dolomitization process, termed Kohout convection, was first identified in the Floridian Plateau; there, cold marine water flows into the side of the Floridian platform, where it is subsequently heated by the geothermal gradient, provided thermal buoyancy, and rises until it meets with the freshwater lens and is circulated back out the side of the platform (Kohout, 1967; Kohout et al., 1977). This half convection cell has the potential to transport magnesium ions through large volumes of carbonate and is unlimited in supply, making the issues of insufficient magnesium and

calcium removal irrelevant. Tidal pumping of marine water down through platform sediments is also known to provide additional hydrologic influence for dolomitization by normal marine waters (Carballo et al., 1987).

Normal marine dolomite can be recognized by the correlation of its geochemical signature to that of the appropriate paleo-oceanic conditions. Strontium isotope ratios and Sr/Ca molar ratios should match seawater signatures, as should carbon and oxygen isotope ratios with the appropriate considerations for climatic variation over geologic time. Dolomite distribution and geometries should also correspond to the patterns created by the convection cells, including their interaction with other fluid systems such as refluxing groundwater or a freshwater lens, or depositional permeability contrasts such as grainstone beds or early-cemented reefs.

Seepage Reflux

Seepage refluxion, or “reflux”, was proposed early on as a regional dolomitization mechanism for the Permian strata of the Guadalupe Mountains (Adams and Rhodes, 1960; Newell et al., 1953) and confirmed as a potential mechanism via numerical modeling later (Garcia-Fresca, 2009). Adams and Rhodes propose that the reef margin of the Capitan platform grew to a vertical extent such that it restricted fluid flow out of the inner shelf lagoon, creating a pond of warm evaporated seawater with elevated salinity and density. Once the salinity increased beyond the saturation point for gypsum (between 112% and 120% as saline as seawater), evaporites precipitated out of the fluid in the lagoon, thus removing Ca^{2+} from the brine, and elevating the Mg/Ca ratio to an appropriate level for dolomitization to occur. The warm, heavy fluids then sank into the platform strata, displacing connate waters and dolomitizing the limestone through which

they percolated. Such an engine has the ability to continue generating brine for as long as the hypersaline environment of the lagoon exists.

Indicators for seepage reflux include the presence of a triple-component mineralogical system, which generally grades from evaporites in the far inner shelf, to dolomite basinward of the evaporitic zone, and finally to limestone near the shelf edge and slope (Adams and Rhodes, 1960). Stable isotope ratios may be variable, depending on the sea conditions and surface temperatures, but should generally have oxygen isotope ratios slightly more positive than those predicted for equilibrium with paleo-sea water, and the ratios should increase with increasing evaporative concentration. Fluid inclusion data, when available, will preclude deep burial temperatures, while petrographic character will rule out mixing-zone characteristics (such as alternating calcite and dolomite cements). Finally, field geometries will reflect the downward and basinward movement of fluid through the shelfal strata.

Mixing Zone Dolomite

Mixing zone dolomitization, or the “Dorag” model, requires a combination of marine water and a freshwater lens, following the assumption that certain combinations of these waters may be undersaturated with respect to calcite and oversaturated with respect to dolomite (Badiozamani, 1973; Hanshaw et al., 1971). Solutions of between 5% and 30% seawater have a reduced ionic strength compared to seawater, which causes undersaturation with respect to calcite, but steadily increasing saturation with respect to dolomite. As such, dolomites precipitated from these waters do not require an elevated Mg/Ca ratio to precipitate dolomite over calcite and evaporites, as most other models do. Ordovician dolomites from Wisconsin are considered the type locality for this mixing-

zone model (Badiozamani, 1973); however, there is still question as to whether or not the evidence truly supports a mixing-zone event (Luczaj, 2006).

Mixing-zone dolomite is also plagued by contradictory geochemical evidence, and has no true "signature". Carbon and oxygen isotopic records have been noted to vary wildly in dolomites attributed to mixing-zone fluids, with $\delta^{13}C$ values as light as -15‰ (Humphrey, 1988) and as heavy as +2‰ (Land, 1973a), and $\delta^{18}O$ values between -4‰ (Badiozamani, 1973) and +2‰ (Humphrey, 1988; Land, 1973b). The depleted values for carbon have been attributed to soil gas involvement, which suggests meteoric waters, but could also be due to bacterial breakdown of organic matter regardless of fluid composition or inherited from the precursor material. Similarly, depleted oxygen values could reflect meteoric water, but require additional data to rule out the influence of higher temperature fluids. Trace elements have also been used in support of mixing-zone dolomitization (Folk and Land, 1975), but most of the examples have been widely criticized (Hardie, 1987; Machel, 2004).

Field relationships may present more consistent evidence for mixing-zone dolomitization. Examples from the Illinois Basin show dolomite that is located immediately below a zone of meteoric diagenesis (Choquette and Steinen, 1980), as have dolomites from Barbados (Humphrey, 1988). While these situations do not preclude dolomitization from mixing-zone fluids, without additional consistent evidence, it is difficult to decisively affirm.

Burial/Hydrothermal Dolomitization

Burial dolomitization was first proposed as the circulation of basin-derived pore waters, which circulate due to large scale regional compaction dewatering (Illing, 1959; Mattes and Mountjoy, 1980); however, fractured reservoirs that allow for penetration of

hydrothermal brines also frequently show dolomitization (Gisquet et al., 2013; Luczaj et al., 2006). Burial fluids are typically warmer than 60°C and rich in magnesium, though concern has been expressed that burial fluids are not an infinite source of magnesium and will eventually bottleneck the formation of dolomite. Burial dolomite crystals typically have characteristic scalenohedral boundaries in thin section from their "saddle" habit, as well as commonly being much larger than shallow fluid dolomite, as temperatures facilitate dolomitization reactions and fluid locations below the active phreatic zone allow for long term crystal growth (Sibley and Gregg, 1987).

Field relationships are unique for burial dolomites. Often, dolomite post-dates stylolitization, and shows distributions that reflect the fluid migration out of the basin and up fault and fracture zones (Gisquet et al., 2013; Kurz et al., 2012; Mattes and Mountjoy, 1980). Additionally, burial dolomites have unique geochemical signatures, with low trace element concentrations, an evolution of fluids with distance from the basinal source (Machel and Anderson, 1989), and negative $\delta^{18}O$ ratios due to elevated fluid temperatures. Assuming that there is no neomorphism of earlier surface dolomite, these features can represent the conditions of the dolomitizing fluid relatively well.

Dolomitization Models and Syndepositional Deformation

Each of the aforementioned dolomitization models could be modified to include influence from syndepositional deformation features. If faults and fractures do in fact behave as fluid flow conduits, the distribution of dolomite in the field should show a positive correlation to the presence of deformation features, either alone or in combination with the distribution expected from one of the four standard models. Frost and others (2012) present a prime example of a mixed distribution, where bed-parallel dolomitization is overprinted by fracture-controlled dolomitization of a later age. Similar

"combination" models for dolomitization are expected in this study, and will rely on both the field relationships and petrographic/geochemical data to provide evidence for the timing and source of fluid responsible for each portion of the combination (see Table 1 for a summary of appropriate characteristics). The following three chapters will evaluate each of these components—field relationships, petrographic relationships, and geochemical data—in turn, before compiling them to generate composite dolomitization models.

Table 1: Table of characteristic for four main dolomitization models

	Normal Marine	***Reflux***	***Mixing Zone***	***Hydrothermal***
Field Geometry	Increase in abundance basinward	Decrease in abundance basinward	Located near zones of meteoric diagenesis	Increase in abundance with depth
Petrographic Character	N/A	Very small crystals	Limpid crystals, alternating dol/cal	Scalenohedral "saddle" texture
Stable Isotopes	Same as seawater	Enriched ^{13}C and ^{18}O	Variable	Usually depleted in ^{18}O due to thermal fractionation
Trace Elements	Same as seawater	Low, due to oxidation in shallow strata	Variable	Variable
Fluid Composition	Seawater salinity conditions	Higher salinity than seawater	5-30% seawater volume	Variable
Temperature	Ambient to slightly elevated (~ 60°C)	~ Ambient temp	~ Ambient temp	Higher than ambient

CHAPTER 2 – FIELD RELATIONSHIPS

Because this study is designed to analyze diagenesis controlled by a seismic-scale structural feature, it necessarily combines field observations with micro-scale petrographic and geochemical analyses. The following chapter will discuss field observations and large-scale relationships between syndepositional structural elements and diagenetic products in the Corral (G24) and Hairpin (G25) members of the Yates Formation in Rattlesnake Canyon. The focus of the study is on a major syndepositional graben, referred to by Kerans, et al. (2012) and Jones (2012) as the Cave Graben Fault System due to its along-strike alignment with the main passages of Carlsbad Caverns. The Cave Graben is bounded by the landward and seaward faults, in addition to minor fault strands and syndepositional fractures.

DEPOSITIONAL SETTING

The Yates Formation, as it is exposed in the seaward segment of Rattlesnake Canyon, is comprised of a portion of the shelf to basin profile containing the reef and reef flat, outer shelf, foreshore/shoreface, and shelf crests facies tracts, the key facies of which were tabulated by Harman (2011). For additional details on Yates Formation facies, see Borer and Harris (1989), Tinker (1998), and Harman (2011). The classification scheme of Harman (2011) was used for field mapping in this study (Table 2), the results of which will be presented below (Figure 5).

Table 2: Facies characteristics, modified from Harman (2011). Facies observed in this study are colored.

Facies Tract	*Facies Name*	*Fabric*	*Dominant Grain Types*	*Sedimentary Structures*	*Diagenesis*	*Bedding Geometry*	*Interpretation*
Middle Shelf	Silty Fenestral Peloid Wackestone-Packstone	Wackestone-Packstone	Peloids, silt-sized quartz and feldspar, rare skeletal fragments	Sheet cracks, irregular microbial lamination, fenestrae	Extensively dolomitized, evaporite psuedomorphs after gypsum	Flat, sub-meter scale bedding, recessive	Intertidal flats and washover from the shelf crest
Shelf Crest - Low to Moderate energy	Tepee-Pisoid Rudstone	Rudstone	Pisoids, composite grains, superficial ooids, ooids, peloids	Meter-scale tepee-buckle structures, aragonite botryoids, fenestrae, irregular laminations	Displacive syn-depositional cement growth, dolomitization	Concave-upward buckled tepees, cliff-forming	Intertidal-supratidal island complex
Shelf Crest - Low to Moderate energy	Fenestral Coated Grain-Peloid Laminite	Mud-dominated Packstone to Rudstone	Peloids, coated grains, pisoids, ooids, skeletal fragments, rare sand	Fenestrae, irregular microbial laminations	Dolomitization, blocky isopachous cement rimming pores	Planar sub-meter scale bedding	Intertidal Flats
Foreshore - High Energy	Ooid-Fusulinid Grainstone/Rudstone	Grainstone/Rudstone	*Polydiexodina* fusulinids, ooids	Seaward-aligned (imbricate) tests, vertical rosettes of tests, seaward- dipping cross beds, beachrock intraclasts, fenestrae	Meniscus cements, isopachous radiaxial cement	Planar meter-scale bedding	Very high energy foreshore
Foreshore - High Energy	Ooid Grainstone	Grainstone	Ooids after peloids, skeletal fragments; peloids, pisoids, fusulinids	Shingled seaward-dipping cross beds	Extensively dolomitized, oomoldic porosity, isopachous to pore-filling blocky cement	Planar meter-scale bedding	Foreshore
Middle - Outer Shelf	Dolomitic Siltstone to UVFSS	Lower very fine to upper very fine sandstone/siltstone	Quartz, feldspars, peloids, rare skeletal fragments, fusulinids	HCS, planar thin bedded, ripple laminated, bioturbated to massive, fenestrae, LLH stromatolites	Dolomitization of peloids, dolomite and clay cements	Recessive, slope-forming	Aeolian transport, transgressive subtidal to intertidal reworking
Outer Shelf - High Energy	Skeletal-ooid Grainstone	Grainstone	Ooids, forams, fusulinids, peloids, gastropods, crinoid fragments	multi-directionally cross stratified, planar, massive	Dolomitization, micritized grain rims	Planar to seaward dipping meter-scale bedding	High energy subtidal shoal
Outer Shelf - High Energy	Skeletal-*Mizzia*-fusulinid Grainstone/Rudstone	Grainstone/Rudstone	*Polydiexodina* fusulinids, Mizzia, forams, crinoids, oncoids, peloids	Low angle cross stratification to massive	Minor dolomitization, micritized grains, isopachous bladed and radiaxial cements	Planar to seaward dipping meter-scale bedding	High energy subtidal intershoal
Outer Shelf - Low to Moderate Energy	Skeletal-Peloid-Oncoid Grain-dominated Packstone/Rudstone	Grain-dominated Packstone/Rudstone	Oncoids, peloids, bivalves, crinoids, forams	Massive, bioturbated	Minor dolomitization, blocky rim cement	Seaward dipping meter-scale bedding	Moderate energy subtidal
Outer Shelf - Low to Moderate Energy	Oncoid-foram-peloid Mud-dominated Packstone	Mud-dominated Packstone	Peloids, forams, small oncoids, crinoids, bivalves	Massive, likely bioturbated	Minor dolomitization	Seaward dipping meter-scale bedding	Moderate energy subtidal
Outer Shelf - Low to Moderate Energy	Foram-peloid Wackestone	Wackestone	Peloids, forams, crinoids	Massive	Minor dolomitization	Seaward dipping meter-scale bedding	Low energy subtidal
Reef Flat	Crinoid-*Collenella* Grain-dominated packstone	Grain-dominated Packstone	*Collenella* sponges, crinoids, bivalves, gastropods, peloids, bryozoan fragments	Massive	Minor dolomitization, patchy brecciated dolomite at exposure surfaces	Seaward dipping, poorly bedded	Moderate energy backreef to reef crest
Reef	Sponge-algal Boundstone	Boundstone	Sponges, *Tubiphytes*, internal sediment, brachiopods	Massive with internal cavities filled with aragonite botryoid cement, internal sediment	Aragonite botryoids, radiaxial fibrous cement	Massive, cliff forming, 10s of meters thick	Moderate energy shelf margin reef
Upper Slope	Interclast-skeletal Grain-dominated Packstone-to-Rudstone	Grain-dominated Packstone, Grainstone, Rudstone	Sponge/brachiopod/crinoid fragments, reef-derived clasts, fusulinids, forams, peloids, oncoids	Graded bedding, internal sediment in shells, slumping around large clasts	Minor dolomitization, blocky isopachous cement	Meter-scale bedding, steep basinward dip (>20 degrees)	Upper Slope with rock fall, grain flows, debris flows

METHODOLOGY

Field work for this study was divided into two phases. The initial phase involved acquisition of high-resolution photo panoramas of the south-facing canyon wall in Rattlesnake Canyon, and subsequent use of those photographs to locate and document individual syndepositional fault and fracture strands within and outside of the Cave Graben. Using a GigaPan EPIC Pro robotic mount with a Canon 5D Mark II SLR digital camera, 25 sequential shots were acquired from the opposite canyon wall. These photos were stitched together using the GigaPan Stitch software and turned into basemaps for fracture mapping, along with an additional GigaPan taken from a different angle (Kerans et al., 2012). During this mapping, fill types, orientation, and aperture of each fracture were documented. The second phase of field work involved identifying diagenetic phases—dolomite in particular—and their distribution with respect to the previously identified syndepositional deformation features, as well as sampling those phases both inside and outside the graben. Mineralogies were mapped onto the basemaps as far as there was visible exposure, and later extrapolated across patches of cover.

Sampling

In order to collect a representative suite of both types of dolomite in all facies tracts, sampling was performed within a total of seven regions (Figure 6), each including 15-20 samples. Three regions were sampled parallel to bedding, running up-dip, away from the Cave Graben. The first region (SA) blankets the G24 reef, and was selected because an anomalously large volume of dolomite can be observed in the reef compared to the equivalent strata elsewhere in the Guadalupe Mountains (Kerans, personal communication); typically the cryptic/muddy nature of the reef, along with syndepositional cementation, prevent substantial fluid flow through the reef itself and

dolomitization is rare. The second region (SC) crosses the outer shelf and shoreface facies tracts of the G25. This path was designed to test the fluid flow conductivity of grain-dominated facies (Table 2) that may have been more porous and permeable than the reef during dolomitization. The third region (SHC) is a transect along the top bench of the G25 shelf crest, and was designed as a "control" sample set for dolomitization that has historically been attributed to syndepositional reflux throughout the Guadalupe Mountains (Adams and Rhodes, 1960).

The remaining four regions were sampled vertically and extend from the reef upward through the shelf crest, parallel to the major structural features in the graben (Figure 6). The first region (SB) begins in the G25 reef outside of the Seaward Fault, and zig-zags across the fault up to the top of the G25 shelf crest. This transect was designed to test whether dolomite is confined to the graben, or if it continues to permeate down-dip outside of the Seaward Fault. The second region (SD) is located inside the Cave Graben, and covers the G25 reef, outer shelf, and the shelf crest. It was selected to test the extent of dolomitization in the G25 reef, and to determine if the dolomite volume can be attributed to the reef's proximity to the graben. A third vertical transect (RS) is located immediately updip from the Landward Fault, and extends from the G24 reef front up through the shelf facies of the G25, capturing the interface between a major syndepositional fracture strand related to the Landward Fault and the host strata. Finally, the fourth vertical region (SLFB) is located slightly updip of the landward fault, and captures the dolomitization of the reef nearest the fault as best as possible, filling in space not covered by the horizontal transects SA and SC.

RESULTS

Syndepositional fractures have been previously characterized in Rattlesnake Canyon, Slaughter Canyon, Walnut Canyon, and Dark Canyon. In general, fracture fills fall into the three categories: (1) clastic-dominated, (2) carbonate-dominated, and (3) mixed siliciclastic/carbonate (Frost et al., 2012; Jones, 2012; Koša and Hunt, 2006a; Koša et al., 2000). Fractures from this study show similar fill lithologies; however, the appearance and fill type of syndepositional fractures in this study are highly dependent on the facies tract in which the fracture is found (Figure 5) (Jones, 2012; this study).

On the GigaPan photos, 120 syndepositional fractures were identified and mapped (Figure 5, Appendix A). These fractures occurred in all facies in both high frequency sequences, and contained a variety of fills including brecciated wall rock; brick red to yellow, iron oxide-rich micrite; early marine cements; siliciclastic, very fine sand to silt; and sparry calcite. The syndepositional faults contain a mixture of all the above components, both heavily brecciated and otherwise, details of which can be found in Mathisen (in progress). Two distinct generations of dolomite are identifiable in the field area: one generation is a fabric-retentive dolomite that weathers gray to tan in the outcrop and is generally pervasive in the shelf crest and foreshore facies tract; and the second generation is fabric-destructive and weathers dusty white on the outcrop, especially when crosscutting limestone host rock. The latter is distinctly spatially related to syndepositional structures in the outcrop window and has been recognized by others (Budd et al., 2013; Frost et al., 2012) to form “chalky haloes” around syndepositional features in limestone Tansill strata in Dark Canyon (G27-29) as well.

Expression of syndepositional deformation in Rattlesnake Canyon varies from opening-mode, single- to multiple-generation-filled, centimeter-scale fractures, to solution-widened multi-generational, breccia-filled meters-wide normal faults. The main

structural features in this study are the two high-angle, margin-parallel normal faults that bound the Cave Graben, which is approximately 170 meters across and has a maximum offset of twelve meters (Kerans et al., 2012). However, individual and anastomosing syndepositional fractures are also considered, as they are abundant in both high frequency sequences and have been previously been proved to behave as fluid conduits throughout geologic time (Budd et al., 2013). Both will be discussed in detail below.

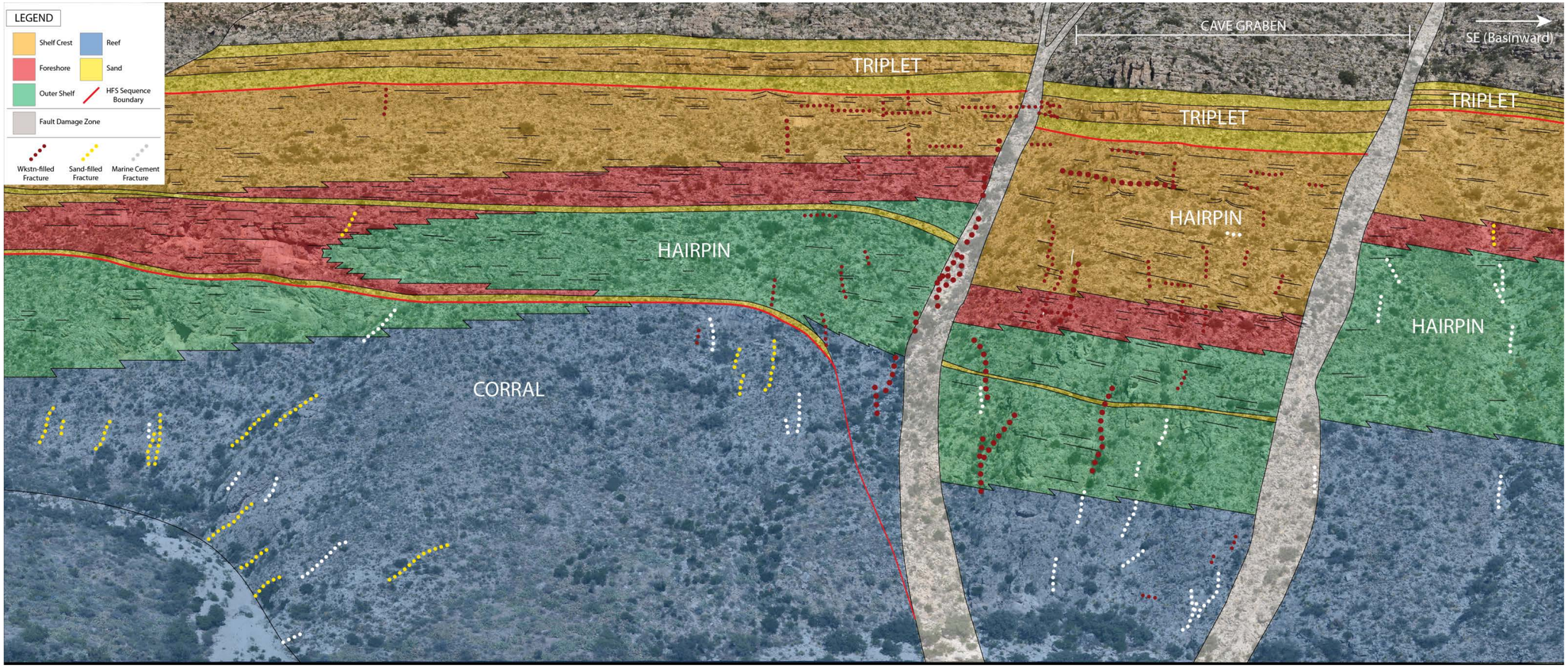

Figure 5: Digitized photopan of the south-facing wall of Rattlesnake Canyon with syndepositional fracture locations. The wall has been colored according to facies tract, and thick red lines indicate high frequency sequence boundaries. Fractures with small dots are less than 20 cm aperture, while fractures with large dots are larger than 20 cm aperture. Note that due to the extreme three-dimensionality of the outcrop, no consistent scale can easily be applied. For reference, the Cave Graben is approximately 170 meters wide, 150 meters tall to the base of the Triplet Member, and the overall dip length of the photopan is approximately 500 meters.

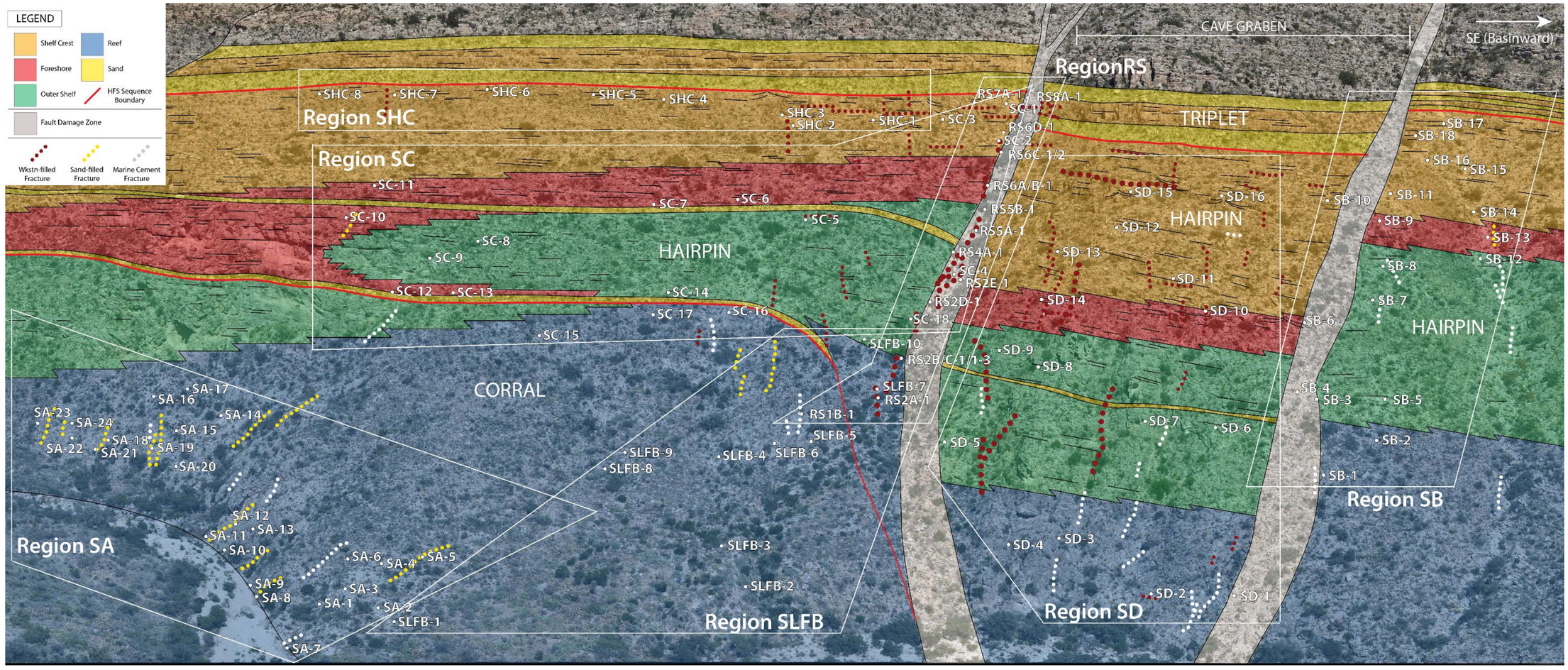

Figure 6: Digitized photopan of the south-facing wall of Rattlesnake Canyon with transect boundaries outlined (white boxes), and sample locations identified. Note that due to the extreme three-dimensionality of the outcrop, no consistent scale can easily be applied. For reference, the Cave Graben is approximately 170 meters wide, and 150 meters tall to the base of the Triplet member, and the overall dip length of the photopan is approximately 500 meters.

Syndepositional Fractures

In the G24 reef, many fractures are filled with very fine sand to silt-sized angular quartz sand (Figure 8). These fractures are five to fifteen centimeters wide, and may have a small amount of auto-brecciation around the fracture edges, as well as white fracture haloes of dolomite up to a meter wide. Alternatively, the fractures may be filled with isopachous marine cements and minor carbonate allochems, with an average aperture of four centimeters but a maximum of nearly twenty. Regardless of fill type or aperture, fractures in the G24 reef are oriented nearly vertical and parallel to the strike of the shelf margin. Primary growth cavities also exist in the G24 reef, and may be filled with variable proportions of either fill type, as well as centimeter-diameter botryoidal cements and microbial reef debris. Comparatively, in the G25 reef, siliciclastic-filled fractures are less abundant, but marine cemented fractures are common, but all have similar aperture and orientation to those in the G24 reef. The siliciclastic fractures again have meter-scale white haloes, while the marine cemented fractures have haloes several centimeters wide or none at all. Figure 7 shows all fracture orientations plotted on a rose diagram.

In the G25 outer shelf and shoreface facies tracts, siliciclastic-filled fractures are less common. Instead, fractures are filled with isopachous marine cements (Figure 9), skeletal debris including fusulinids, *Mizzia*, peloids, and oncoids, or brick red to bright yellow ostracod wackestone with abundant micritized four to eight chambered microcoprolites (Figure 10). These fractures range from 5 centimeters to 20 centimeters in aperture, and are most commonly oriented vertical and parallel to the strike of the shelf margin. Some of these fractures have white dolomite haloes, though they are less common and only a few centimeters wide. The only exception to this rule are several 30-40 cm aperture, wackestone-filled fractures immediately downdip of the landward fault—these fractures have dolomite haloes over a meter wide (Figure 5).

Brick red to bright yellow ostracod wackestones with microcoprolites are the most abundant fill for syndepositional fractures in the G25 shelf crest facies tract. Fractures in this facies are commonly three to four centimeters in aperture, and have a rim of botryoidal or isopachous marine cement around the margins with banded layers of red and yellow wackestone in the centers; very little siliciclastic material is present. Unlike in the preceding facies tracts, many of these fractures are bedding parallel, i.e. sheet cracks. Often, the red fills pinch out against pisoid shoals and tepee complexes, and connect in anastomosing networks that cross thin beds of fenestral laminite. However, some margin-parallel sub-vertical wackestone-filled fractures are present separate from the anastomosing sheet cracks, and both orientations were observed to have small white dolomite haloes.

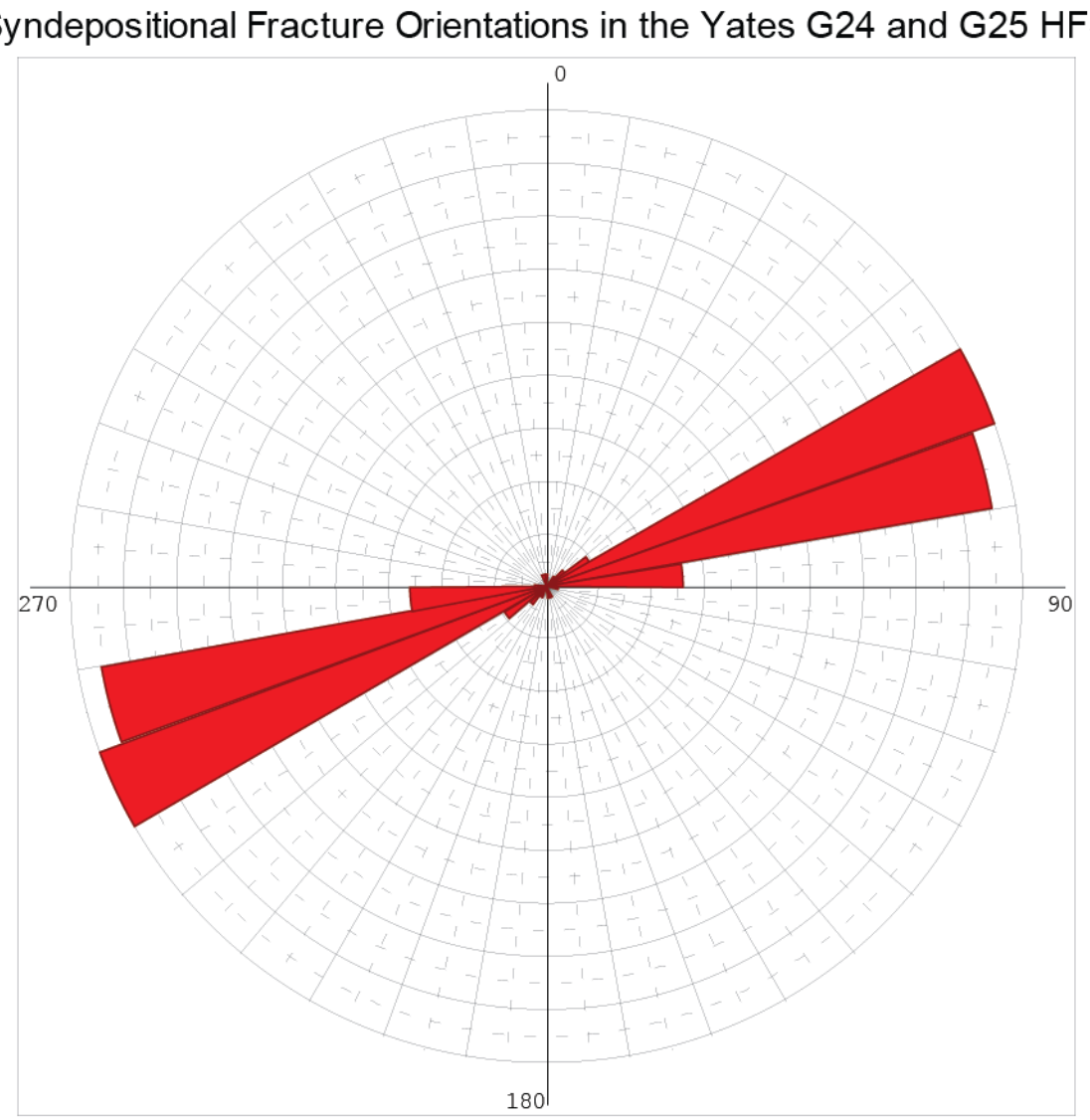

Figure 7: Rose diagram of the trend of all syndepositional fractures in the G24 and G25 high frequency sequences, excluding horizontal sheet cracks. N = 84.

Figure 8: Very fine quartz sand-filled syndepositional fracture from the G24 reef (white outline). To the left of the fracture is a dolomite halo (white dashed line) with a visible reaction front (red triangles) within the limestone host rock. Hammer is 28 cm (11 in.)

Figure 9: Marine cement-filled fracture in the G25 reef (white outline) with botryoidal aragonite lining on the fracture wall. Dolomite halo reaction front is beyond range of photograph.

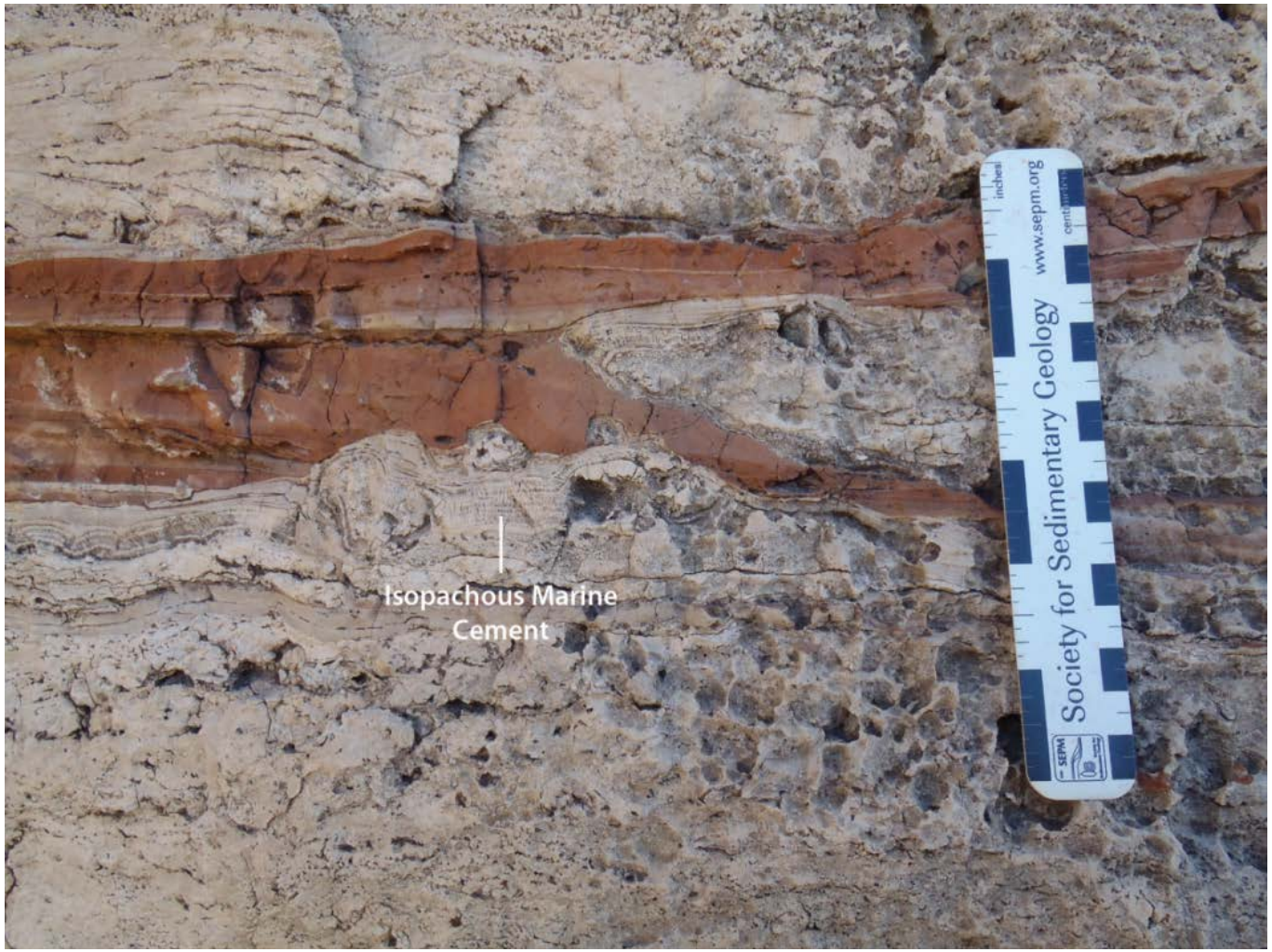

Figure 10: Red and yellow ostracod microcoprolite wackestone filling a horizontal fracture in the G25 shelf crest facies. Fracture edge is rimmed with three generations of isopachous marine cement, partially growing around pisoids.

The abundance of siliciclastic fills in the G24 reef is likely due to the close proximity of the overlying basal G25 sandstone bed, which lies directly on top of the G24 high-frequency sequence boundary (Figure 5). These sands are interpreted to have migrated down into the fractures during the end of G24 deposition and during the lowstand period in which sands bypassed the shelf (Hunt et al., 2002; Koša et al., 2003). A lack of shelf-derived skeletal allochems in these fractures supports this timing. Similarly, the decreased abundance of siliciclastic material in G25 reef fractures and cavities may be due to the lack of such a ready source of siliciclastic material. What minor siliciclastic components there are may be derived from the "middle Hairpin sand" (Mutti and Simo, 1993; Mutti and Simo, 1994), or from the sands of the Triplet member (Jones, 2012), however the maturity of the sand bodies in the Yates Formation makes distinguishing an individual source bed difficult from field observations alone.

A distinct lack of siliciclastics in the sheet cracks and vertical, wackestone-filled fractures of the G25 shelf crest poses an interesting dilemma. Based on the proximity of the top Hairpin to the thick sands of the Triplet member, there should logically be an abundance of siliciclastic material in the upper Hairpin fractures, and in fact, there is a noticeable percentage of sand in the beds of the shelf crest itself. However, only a very small amount of sand is present in either the vertical fractures, or the bedding parallel sheet cracks. This may simply indicate a lag in siliciclastic bypass of the shelf; if Triplet siliciclastics were trapped behind the tepee belt during initial stages of lowstand exposure, the ostracod wackestone may have preferentially infiltrated fractures before siliciclastics crossed the shelf.

Ostracod wackestone fracture fills were very rarely observed outside of the top of the Yates Formation in Rattlesnake Canyon (Appendix A). This suggests that they are related to the exposure event at the top of the G25, and percolated downward into the

open fractures. Within the Tansill Formation, in Rattlesnake, Walnut,, and Dark Canyons, fractures are either filled with siliciclastic sediment (presumably sourced from the Ocotillo siltstone), or with marine cementation, carbonate mud, and minor breccias (Budd et al., 2013; Frost et al., 2012; Jones, 2012).

Syndepositional Faults

Syndepositional faults in Rattlesnake Canyon also have a wide range of expressions, including matrix-supported and clast-supported breccias with carbonate-dominated, clastic-dominated, and mixed lithology fills. Koša and Hunt (2006a; 2003; 2000) provide detailed descriptions of fault geometry, fault fills, and fault-related paleocavern styles in Slaughter, while Mathisen (in progress) did the same in Rattlesnake Canyon and Slaughter Canyon specifically for the Cave Graben fault system. Her classification scheme and clast percentages were used to augment the descriptions below.

Clast-dominated breccias include crackle breccias, mosaic breccias, and chaotic breccias that contain 65-70% clasts. Crackle breccias include clasts larger than 2 mm that are separated by thin cement-filled fractures and show little rotation. These breccias are typically monomict, and are located largely in host rock around the edges of faults, and in between fault splays. Mosaic breccias consist of similarly sized monomict clasts, but show minor rotation and typically have wider zones between clasts, which may be filled with cement or sediment. These breccias also occur on the margins of fault zones, but were also observed in fault splays and fractures within the Cave Graben. Chaotic breccias are the most complex breccias, and show highly rotated clasts that may be monomict, oligomict, or polymict. These breccias make up a majority of the fault zones for the landward and seaward faults, and may contain clasts of siliciclastic clasts below the Triplet member, and carbonate clasts including reef boundstone, ooid grainstone, and

fusulinid packstone throughout the rest of the fault zone (Figure 11). Clasts greater than 2 mm are much less common in chaotic breccias, but where observed may be crackle or mosaic brecciated themselves.

Matrix-dominated breccias typically contain fewer than 30% clasts, and have fills including carbonate sediment, carbonate-cemented siliclastic sediment. Carbonate sediment breccias are comprised of a variety of material, including ostracod wackestone, ooid grainstone, and fossiliferous grainstone. These fills generally do not compose the main fault zone, but are instead located in fracture strands around the faults. Siliciclastic sediment breccias include massive sandstone with dolomite cement, which is common in the fractures and cavities of the reefal facies (see above section), and a wide variety of calcite-cemented features including pebble conglomerates to lithic sandstones. Koša and Hunt (2006a) have related several of these latter fills in Slaughter Canyon to multiple karsting events.

Figure 11: Chaotic polymict breccia in the seaward fault damage zone Photo oriented facing stratigraphically up. Field book is 19 cm (7.5 in) on the long edge.

Dolomite Distribution

During mapping of syndepositional faults and fractures, two types of dolomite were identified in the Rattlesnake Canyon field area. The first generation is a fabric-retentive dolomite that weathers gray to tan on the outcrop (Type I Dolomite), and the second is a fabric-destructive dolomite that makes distinct white haloes around syndepositional faults and fractures (Type II Dolomite). These dolomites were mapped across the canyon wall, and samples were collected from the seven regions to provide a representative suite of each type, as well as the host rock, for petrographic and geochemical analysis (Figure 12). The results of the dolomite mapping will be described for each sampling region below.

Region SA – G24 Reef

Samples through region SA show partial dolomitization of the reef facies, with heavily dolomitized matrix muds, but well preserved calcitic bryozoans, forams, isopachous marine cements, and micritic peloids in a majority of samples. However, a few samples are completely comprised of fabric-destructive dolomite; the heaviest dolomitization is always directly adjacent to syndepositional faults and fractures or reef cavities—especially where siliciclastic fills abound—and decreases away in all directions (Figure 12). In general, all of the dolomite in this transect appears to be Type II, as it appears consistently as white haloes around fractures and cavities, but the preservation of calcitic allochems makes determining the nature of the dolomite somewhat deceptive by visual inspection alone.

Region SB – G25 Reef to Shelf Crest, Seaward Fault

Samples through the SB sampling region also contain a mix of dolomitized and undolomitized rock, with fabric-destructive dolomite demonstrating a distinct spatial tie

to the Cave Graben faults. Reef samples near the base of the seaward fault, both inside and outside of the graben are dolomitized, with similar white haloes around syndepositional fractures and reef cavities. As the transect passes up into the outer shelf, samples taken from inside the graben are still heavily dolomitized, but samples outside of the graben become predominantly limestone host rock, with well-preserved calcitic allochems and marine cements. Within the limestone portions of the outcrop, small white dolomite haloes on the centimeter scale can still be observed around syndepositional deformation features. Near the top of the sampling region, in the shoreface and shelf crest facies, fabric-preservative, gray to tan dolomite becomes the dominant mineralogy both within and outside of the graben (Figure 12).

Region SC – G25 Outer Shelf to Shoreface

Region SC crosses the G25 outer shelf and shoreface facies updip of the Cave Graben, which are comprised of skeletal material and generally contain much less mud than the reef itself. It was chosen to observe the distribution of each type of dolomite within grain-dominated beds that may have been more porous and permeable to dolomitizing fluids over time. Samples from this transect are heavily dolomitized by both generations of dolomite, though a few limestone samples still remain. Type I dolomite is prevalent throughout the shelf crest facies tract and most of the upper foreshore, while fabric-destructive dolomite is, again, spatially tied to syndepositional fractures and the Landward Fault. Portions of this sampling region also contains unique, finger-like bodies of fabric-destructive dolomite which extend into sand beds and grain-dominated facies away from faults and fractures for up to tens of meters (Figure 12). Similar geometries were also observed in Dark Canyon, and were attributed to high fluid flux through the most permeable beds intersected by deformation features (Frost et al., 2012).

Region SD – G25 Reef to Shelf Crest, Landward Fault

Sampling region SD contains samples that cover the G25 reef, outer shelf, and shelf crest, but due to cliff steepness and climbing limitations, they were not collected in a single vertical succession. The first five samples span the lower reef inside the graben, and are heavily dolomitized with fabric-destructive dolomite. This dolomite is linked to syndepositional fractures and the landward fault, especially the 30-40 cm aperture fracture strands located in the reef directly downdip from the landward fault. It is also observed as patchy spots within the reef slightly away from fractures. The second five samples cut across the outer shelf facies and contain a mix of the two dolomite types, while the remaining samples cover the shelf crest facies, and are mostly comprised of fabric preservative replaced pisoids and algal laminites (Figure 12). Samples from this region also contain a small fraction of clastic material (mostly 5% or less, but up to 50% near the Landward Fault and in the large fracture strands) that is cemented with dolomite.

Region SLFB – G24 and G25 Reef to Outer Shelf

Region SLFB is a shorter transect than the other three vertically sampled regions, collected in an effort to bridge the vertical gap between the top of region SA and the bottom of region SC in the G24/25 reef to outer shelf. This region is immediately adjacent to the roll-over of the G24 margin, and is also located within 20 meters of the Landward Fault, providing an opportunity to compare dolomitization outside the graben to dolomite inside the graben (transect SD), and dolomitization of the G24 reef to that of the G25 reef. A majority of the samples from Region SLFB are partially replaced by dolomite; however, calcitic bryozoans and fusulinid forams still retain their original texture well, as with the reef samples of region SA. These samples were also not specifically collected from haloes around syndepositional fractures, so the presence of the dolomite is attributed to the samples' close proximity to the Landward Fault.

Region RS – Syndepositional Fracture Interface

All of the samples from transect RS are heavily dolomitized by fabric-destructive dolomite and were taken specifically from haloes around a major fracture strand just updip of the landward fault damage zone; most have been broken into various breccias/compound breccias, and re-cemented by sparry calcite cement. The fracture fills include very fine to fine, angular quartz sand that weathers beige on the outcrop (similar to the clastic fills in the G24 reef); marine cements and allochems that are heavily recrystallized; and deep red to bright yellow micrite which appears in both the vertical fracture strand and in horizontal sheetcrack-like offshoots of the main fracture. A noticeable amount of metal oxides are also present in the fracture fills.

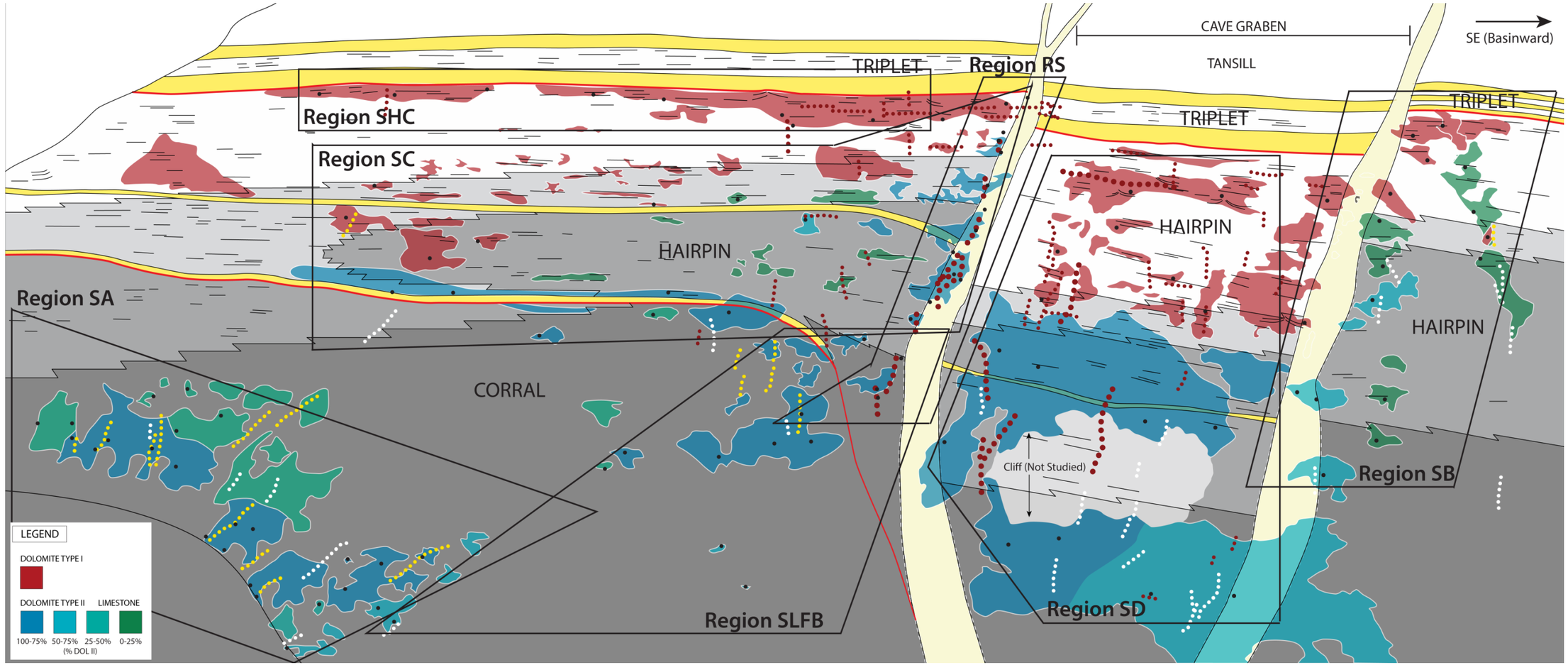

Figure 12: Distribution of dolomite across the outcrop window, as specifically observed on the outcrop. Areas lacking color are covered or inaccessible due to steepness of cliff faces; size of colored patches simply reflects exposure and is not an estimate of overall dolomite extent. Sample locations are indicated by black dots. Percentages of Type II dolomite were supplemented with estimations from petrographic data.

DISCUSSION

Type I dolomite is pervasive through the shelf crest and foreshore facies tracts in both high frequency sequences in Rattlesnake Canyon, and shows a distinct decrease in abundance both down the canyon wall and towards the basin. This geometry suggests that the dolomitizing fluid responsible for the first generation of dolomite was sourced from the interior of the platform, and circulated towards the basin (Figure 13). There is almost certainly some fault and fracture influence in the distribution of this dolomite, as it is pervasive through the growth-thickened strata of the G25 shelf crest, and would necessarily have to travel across and down the landward fault to reach these strata. However, it does not show a strong preference for faults and fractures like the second generation, and instead reflects flow largely along bedding.

Comparatively, previous studies of the diagenesis of syndepositional fault and fractures in Slaughter Canyon have observed that Type II dolomite is not uniformly distributed, neither in terms of a single fault with multiple generations of fill, nor across the spectrum of deformation features in an outcrop window. Instead, it is preferentially linked to syndepositional faults, fractures, and reef cavities that are filled with siliciclastic material, due to their enhanced permeability (Koša and Hunt, 2006a; Melim, 1991; Yurewicz, 1976).

Type II dolomite is distributed similarly in the Rattlesnake Canyon window, with a strong preference for siliciclastic-filled fractures, portions of the faults, reef cavities, and sand beds (Figure 14). Haloes around these features can be over a meter in diameter, compared to decimeter-scale or non-existent around marine-cemented fractures and reef cavities. Haloes can also be present around the wackestone-filled fractures both in previously dolomitized and undolomitized strata, however, they are generally much

smaller in diameter than haloes around siliciclastic-filled fractures, averaging several centimeters with a maximum of fifteen centimeters diameter (e.g. sample SHC-2). The exceptions to this observation are the 30-40cm aperture wackestone-filled fracture strands located around the landward fault, all of which have meter-scale haloes. This strong preference for siliciclastic-filled fractures creates what appears to be a major halo in the G24 reef, but in reality, the halo is comprised of several smaller fracture haloes that have bled together to create a wider distribution.

Interparticle porosity-related permeability of depositional fabrics is also a control on the distribution of the fabric-destructive dolomite in Rattlesnake Canyon, though it is secondary to the control exerted by the presence of syndepositional faults and fractures. Where permeable faults and fractures intersect sandy or grain-dominated beds, fabric-destructive dolomite haloes may extend into the strata up to several meters away from the fracture. Similar control has been observed around fractures in Dark Canyon (Frost et al., 2012).

In combination, the two generations of dolomite create a volumetrically significant body of dolomite in and around the Cave Graben in Rattlesnake Canyon (Figure 15). The reef facies tracts in both high frequency sequences are heavily dolomitized compared to equivalent strata elsewhere in the Guadalupe Mountains, due to the presence of numerous syndepositional fractures and siliciclastic-filled reef cavities. In comparison, the outer shelf remains largely limestone, except around syndepositional faults and fractures. Finally, the foreshore and shelf crest facies tracts are also heavily dolomitized by what appears to be a fluid fluxing basinward from the interior of the platform.

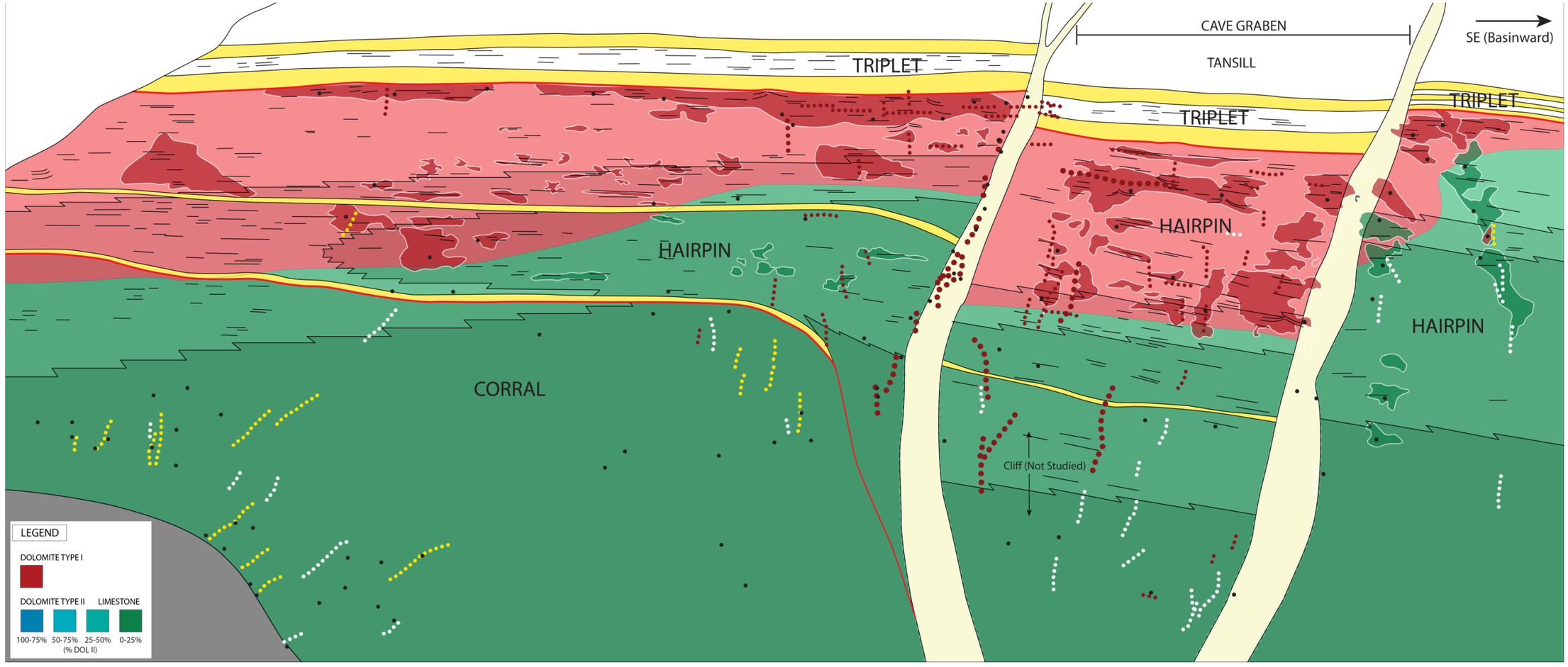

Figure 13: Interpreted distribution of Type I dolomite on the outcrop, using sample control points (black dots) and field mapped dolomitized zone data. Red represents Type I dolomite, while green represents undolomitized strata. Note the decreased abundance of dolomite basinward.

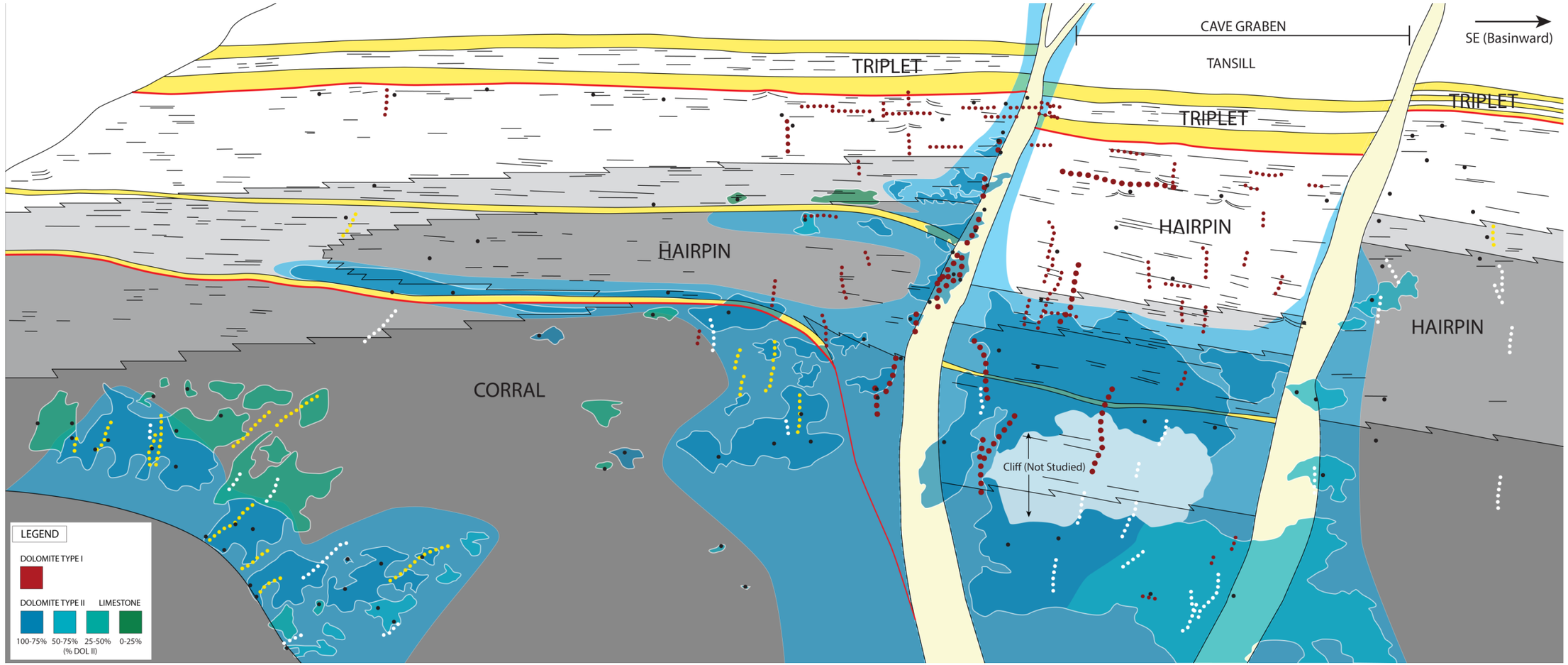

Figure 14: Interpreted distribution of Type II dolomite on the outcrop, using sample control points (black dots) and field mapping data. Note the strong preference for heavily fractured zones, the landward and seaward faults, and permeable strata such as sand beds and grainstones.

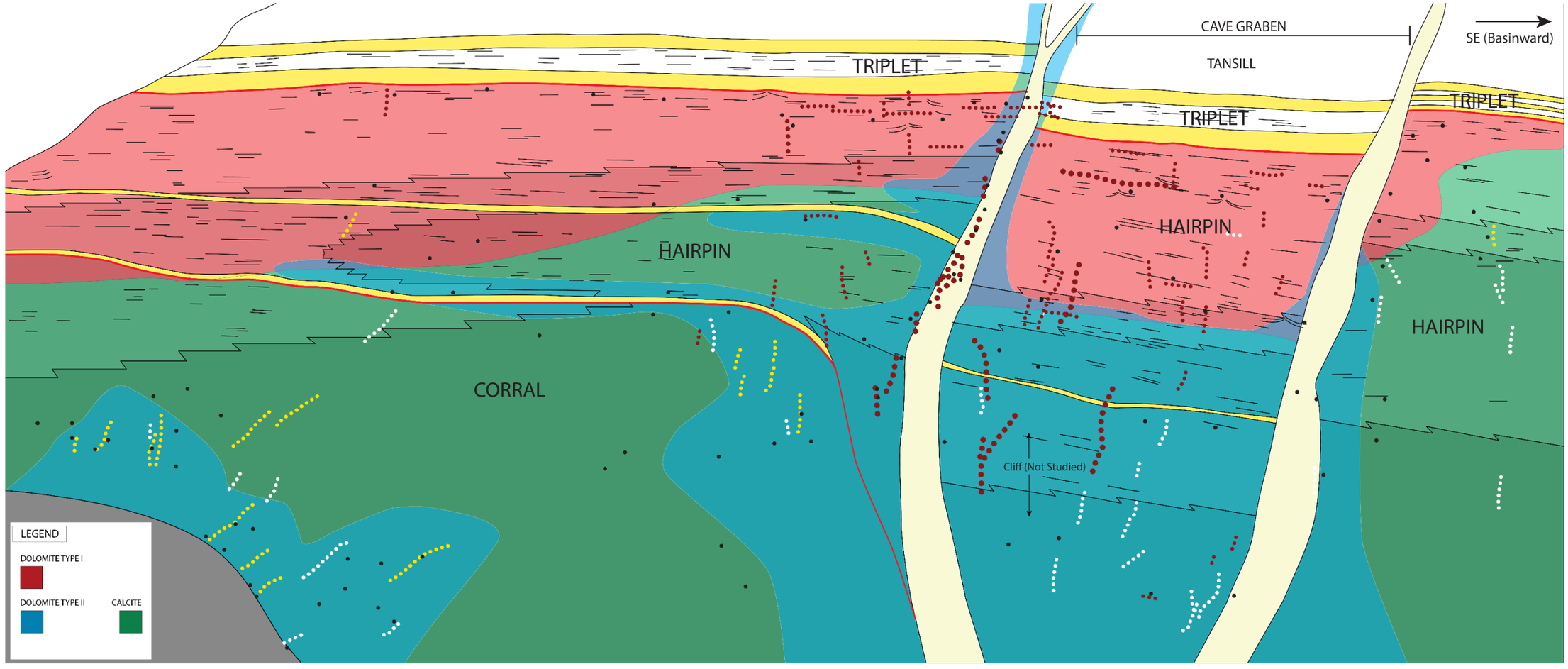

Figure 15: Composite dolomite distribution in Rattlesnake Canyon outcrop window, with sample control points (black dots) and mapped fracture distribution.

CHAPTER 3 — PETROGRAPHY

Following collection of a representative sample suite of each dolomite type and the undolomitized host limestone, petrographic analysis was performed to determine a paragenetic sequence for diagenesis in Rattlesnake Canyon, and to provide temporal context for the two generations of dolomite visible in the field. The resulting paragenetic sequence provides critical qualitative evidence for the timing of dolomitization, which can be used in combination with quantitative geochemical data to determine the most likely fluid source for dolomitization. Additionally, understanding the timing of dolomitization, and relating it to the spatial distribution of dolomite around faults and fractures is an indicator of which time periods faults and fractures may have influenced fluid flow. The following chapter will discuss the paragenesis, and will introduce evidence for fluid source and flow timing preceding the complete analysis in Chapter 4.

METHODOLOGY

Petrographic characterization of the diagenetic products present in Rattlesnake Canyon was performed using standard 30 μm polished thin sections. Each section was half stained in Alizarin Red S for 45 seconds following a 10-15 second etch in 2% hydrochloric acid. Analysis was then performed on a Nikon Eclipse E400 polarized light microscope, and a Nikon microscope with a Technosyn 8200 MKII cold-cathode luminoscope, operated at 55-75 mTorr, 6.0 kV, and between 300 and 1000 nA. CL photomicrographs were taken over long exposures ranging from seven to eleven seconds.

Initial observations were made to determine a generalized paragenetic sequence, based on crosscutting relationships. This sequence includes (1) botryoidal and isopachous marine cementation, (2) micritization of grains, (3) replacement of mud and grains by fabric-retentive dolomite, (4) recrystallization of early dolomite and dolomitization of

host limestone by fabric-destructive dolomite, (5) pore-filling calcite. CL microscopy confirmed each of the first four steps, and identified an additional three sub-phases within the pore filling calcite episode: (a) a dully luminescent phase, (b) a brightly luminescent orange-banded phase and (c) a non-luminescent phase. Each of these episodes of diagenesis will be discussed in detail below.

CEMENTS AND DIAGENETIC PRODUCTS

Early Marine Cements

Recrystallized Botryoids

Botryoidal calcite cements are common in both the reef facies and the shelf crest facies of the G24 and G25 high frequency sequences; however, due to the extensive diagenesis of strata in Rattlesnake Canyon, most of these cements have a variable amount of their original fibrous habit preserved. Most frequently observed are radial arrays of linearly elongate but much coarser dolomite crystals that have recrystallized the original cements; several of the arrays have crystals between two to three mm in length. The replacement crystals are usually slightly cloudy and associated with dark, fibrous fluid inclusions that create “ghosts” of the original texture. Square tipped crystal terminations can be seen in samples that have micrite drapes over the botryoids, which is characteristic of cements that were originally bladed aragonite, and suggests that the botryoidal cement was both syndepositional and precipitated from Permian sea water. Botryoids in this study typically have patchy, moderately bright orange-red to red luminescence, with bright red rims. Figure 16, below, shows three examples of dolomitized botryoids from the G25 shelf crest facies in plane polar and CL light.

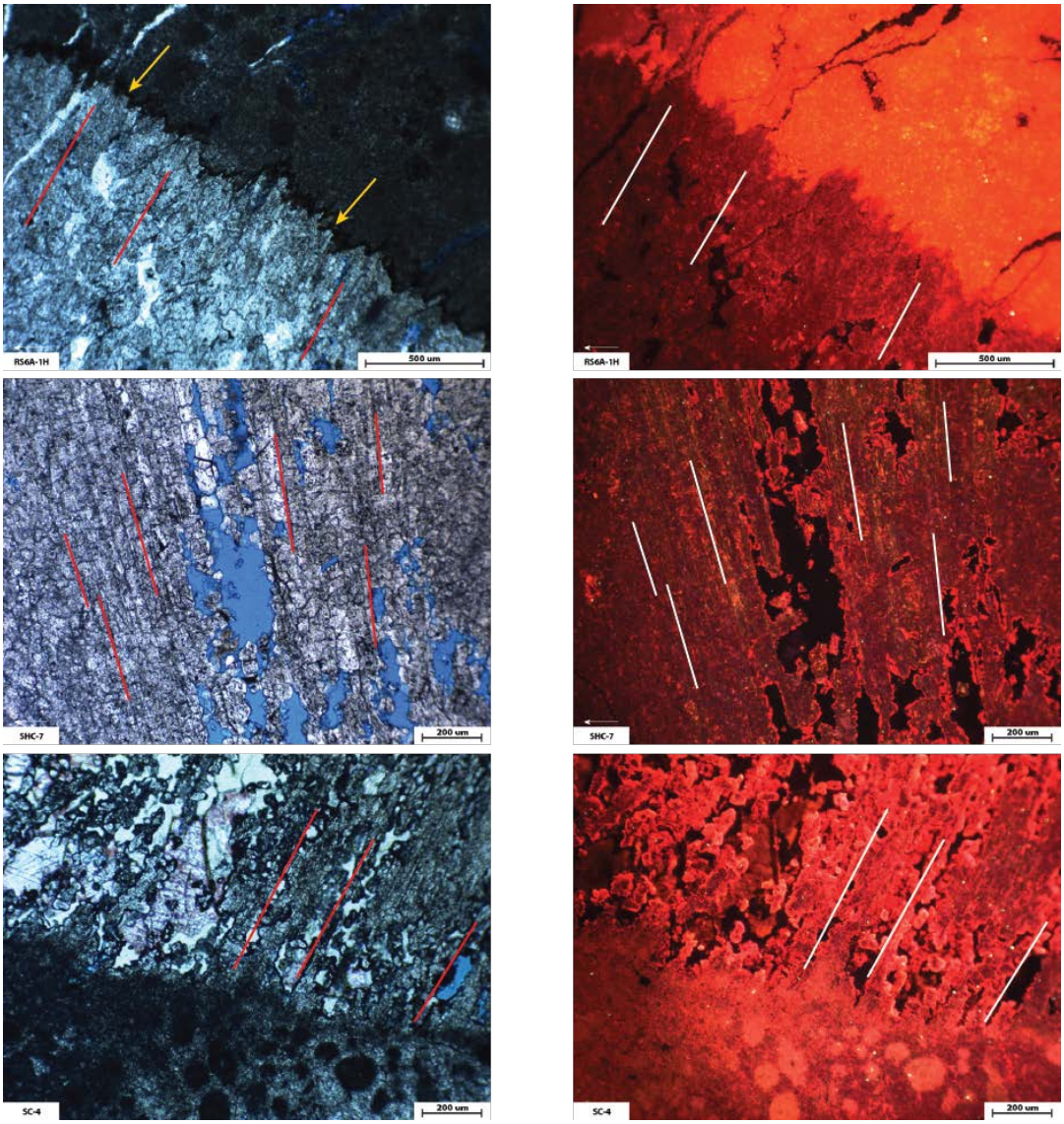

Figure 16: Dolomitized botryoids in plane and cathodoluminescent light. (Top) Micrite drape over botryoid luminesces bright orange, while coarse dolomite botryoid shows patchy red luminescence. Square tips of relict bladed aragonite can be seen beneath the micrite (yellow arrows). Scale is 500 µm. (Middle) Botryoid with coarse elongate dolomite crystals with relict bladed texture, patchy red luminescence, and bright red luminescent rims. Scale is 200 µm. (Bottom) Botryoid with coarse elongate dolomite crystals, also showing relict bladed texture, adjacent to microcoprolite-rich sheet crack fill. Scale is 200 µm.

In the reef, these botryoidal cements typically fill cavities, while in the shelf crest, they grow within sheet cracks that are not otherwise filled with sediment. These botryoidal cements are also found lining the inside of syndepositional deformation features, including the decimeter-scale vertical fracture strands running parallel to the Landward Fault in the G25 reef. The presence of primarily marine cements inside the deformation features is strong evidence that they were active very early in the history of the platform. Similarly recrystallized botryoids have been identified across the Guadalupe Mountains, including in Dark Canyon (Budd et al., 2013; Mazzullo, 1999), Slaughter Canyon (Bishop et al., 2014), McKittrick Canyon (Given and Lohmann, 1985; Mruk, 1989; Scholle et al., 1992), and in the subsurface (Garber et al., 1989).

Isopachous Radial Calcite

In addition to the precipitation of botryoidal cements, several generations of isopachous calcite precipitated in pore linings across all facies, and around grains in the outer shelf grainstones and grain-dominated packstones. In this study, up to five individual generations can be counted, and elsewhere in the Guadalupe Mountains, there are as many as nine (Mruk, 1985, 1989). These cements are either low Mg calcite or dolomite in Rattlesnake Canyon, and take the form of bladed to loafish, variably included crystals up to half a millimeter in length. Luminescence depends on the current mineralogy: low Mg calcite cements are largely non-luminescent, which dolomitized relict isopachous cements are typically have dull orange or red luminescence. Figure 17 shows several examples of these isopachous cements.

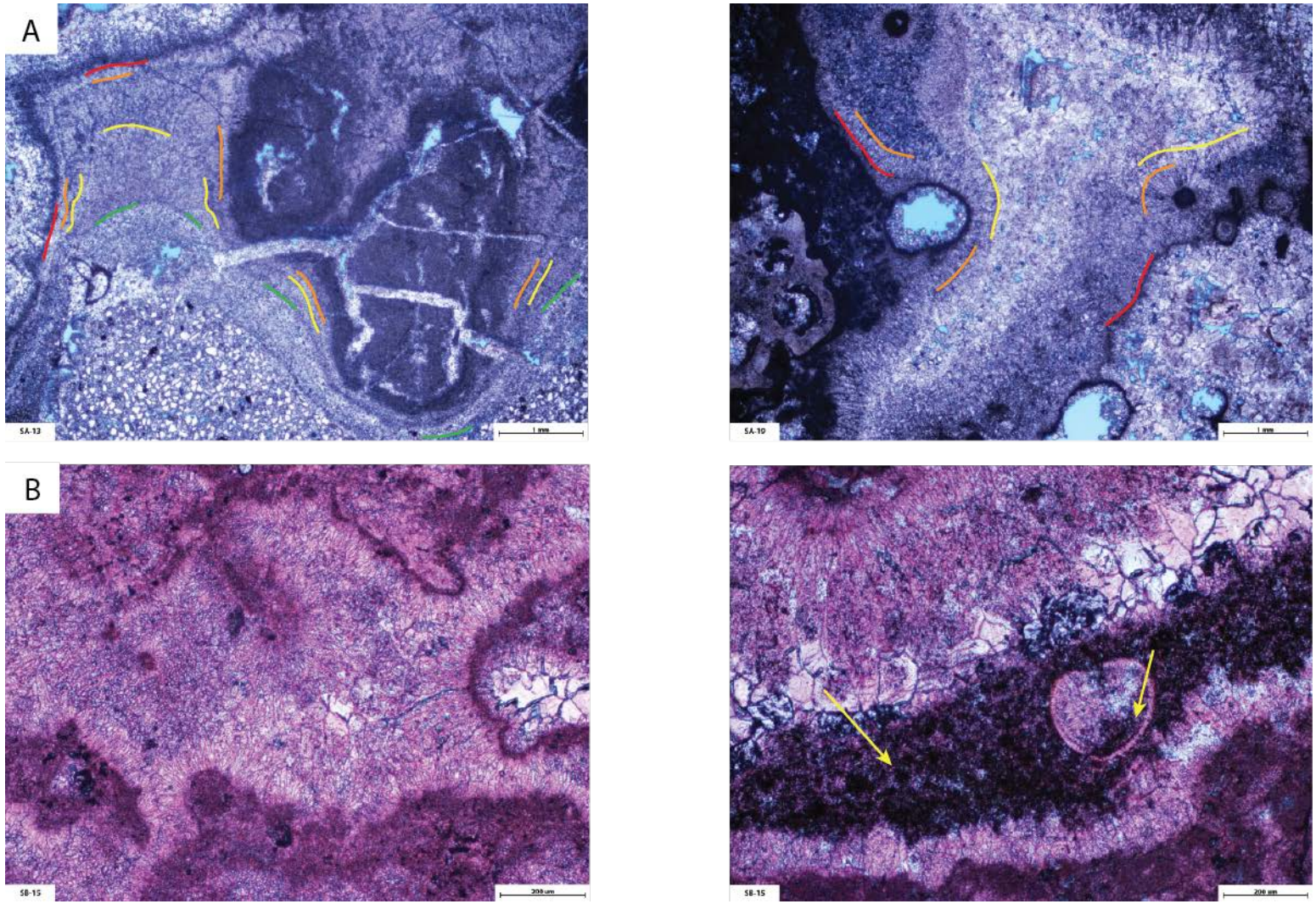

Figure 17: See below for complete caption

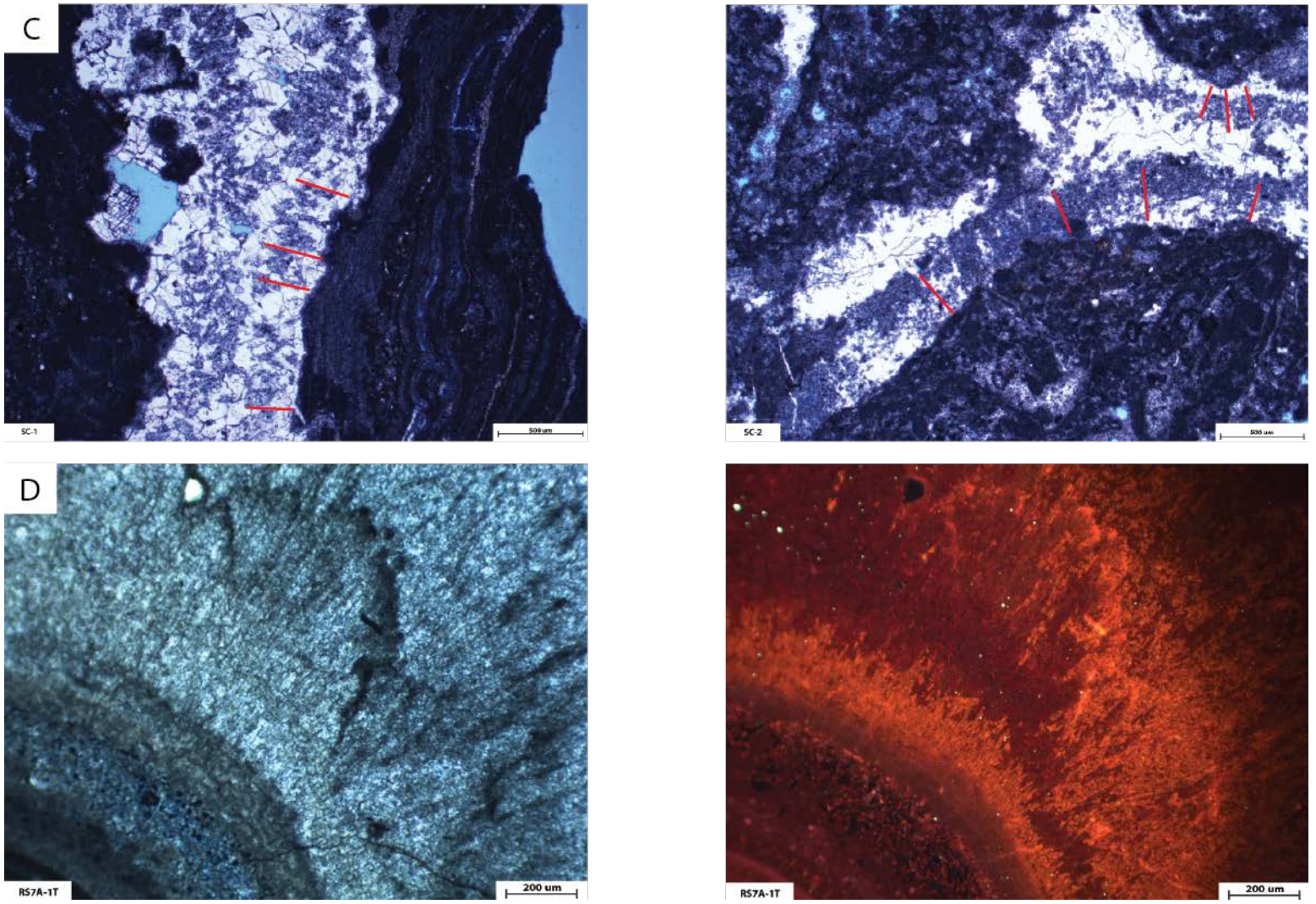

Figure 17: See below for complete caption

Figure 17—Previous Pages: Isopachous calcite and dolomitized calcite cements in plane polar and cathodoluminescent light. (A) Multigenerational isopachous calcite cement. Generations are separated and partially outlined by different colored lines. Both are from the G24 reef facies. Scale is 1 mm for both. (B) Rounded tips of bladed calcite cements (left) with geopetal peloidal drapes (right; yellow arrows), suggestive of syndepositional, high Mg calcite origin. Slides have been stained with Alizarin Red S. Both are from an undolomitized portion of the G25 reef. Scale is 200 µm for both. (C) Microdolomitized remnants of primary isopachous calcite cements. Red lines indicate elongation direction of original crystals. Both are from the outer shelf facies of the G25. Scale for both is 500 µm. (D) Dolomitized isopachous cements around a pisoid in the G25 shelf crest facies. Dolomitized cements show several generations, with moderately bright red to orange luminescence. Scale for both is 200 µm.

Isopachous calcite cements are common across the Guadalupe Mountains in both the subsurface (Garber et al., 1989) and in outcrop (Bishop et al., 2014; Given and Lohmann, 1985, 1986; Melim, 1991; Melim and Scholle, 2002; Mruk, 1989). They are considered syndepositional due to the cross cutting relationships they show with both dolomite and pore-filling calcite phases; in fact, many samples from this study show thick isopachous rinds on grains and in cavities without any evidence for earlier botryoidal cementation. Most well-exposed examples also show preservation of curved crystal tips, which suggests a high Mg calcite origin. This morphology and likely mineralogy, in combination with the crosscutting relationships, suggests that the isopachous cements are primary, occurring simultaneously to or following only the growth of marine botryoids. Some studies have identified both radiaxial fibrous calcite and fasicular optic calcite cements (Bishop et al., 2014; Rahnis and Kirkland, 1999); the former is identifiable in this study as well.

Fabric-Retentive Dolomite – Dolomite Type I

The earliest phase of dolomitization for which there is evidence in Rattlesnake Canyon is a generation of fabric-retentive replacement dolomite that ranges from 2-3 μm to 30 μm. When visible, the crystal boundaries are non-planar, and the centers are dusty and included with what may be undigested calcite. They luminesce an earthy, dull orange to red. This generation of dolomite is pervasive throughout the G24 and G25 shelf crest facies tracts in and around the Cave Graben, as evident by dolomitized but texturally well-preserved pisoids. Skeletal grains and matrix components are also commonly replaced by the fabric-retentive dolomite in the foreshore facies tract, though this is mostly observed up-dip of the graben. Figure 18 shows examples of fabric-retentive dolomite in several facies.

The fabric-retentive dolomite in Rattlesnake Canyon has also been identified elsewhere in the Guadalupe Mountains, including in the Yates further towards the head of Rattlesnake Canyon in the shelfal strata (Mutti and Simo, 1993; Mutti and Simo, 1994), in Dark Canyon in Tansill shelfal strata and associated with syndepositional deformation features (Budd et al., 2013; Frost et al., 2012), in the Yates Formation of Slaughter Canyon (Koša and Hunt, 2006a; Koša et al., 2003), in the Yates and Seven Rivers of McKittrick, Pine, and Bear Canyons (Melim, 1991; Melim and Scholle, 1989, 2002), in the Gulf PDB-04 research core (Garber et al., 1989).

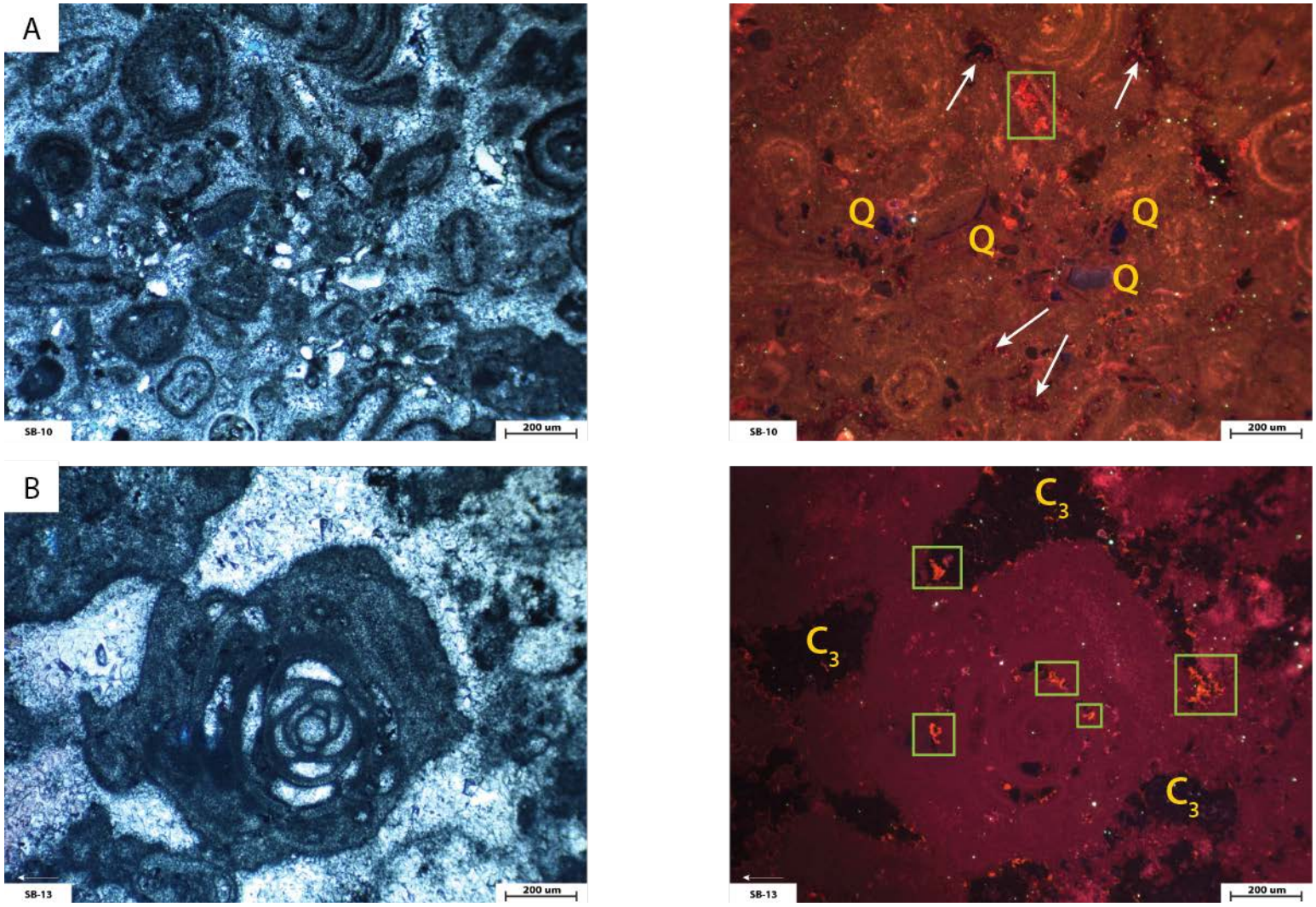

Figure 18: See below for complete caption

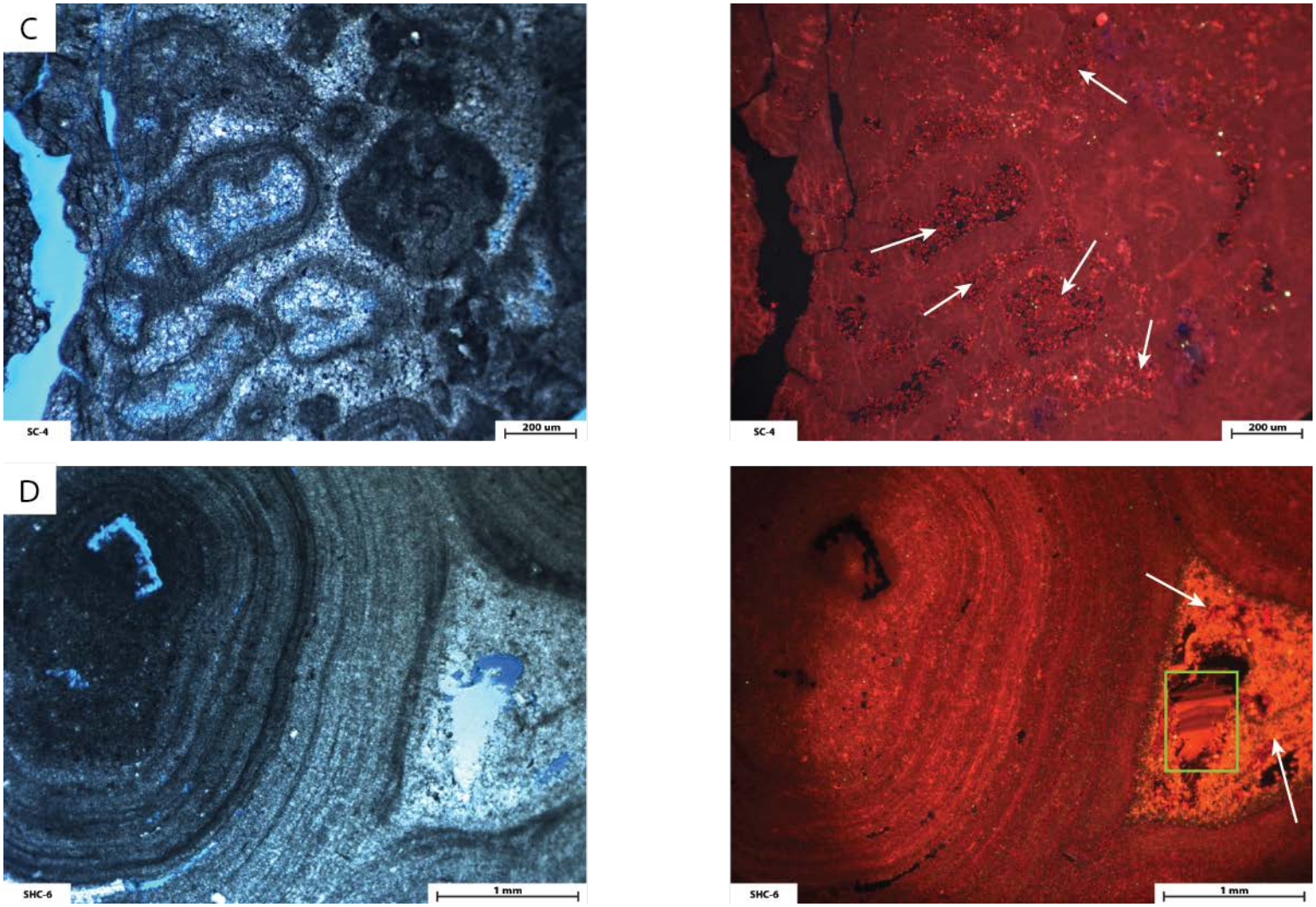

Figure 18: See below for complete caption

Figure 18—Previous Pages: Fabric-retentive dolomite (Dolomite Type I) in plane polar and cathodoluminescent light. (A) Skeletal hash of the G25 outer shelf facies. Dolomite selectively replaces micritized skeletal fragments and shows and earthy orange luminescence. A second phase of bright dolomite cement lines pores (white arrows), and late pore filling calcite luminesces bright orange (green box). Scale is 200 µm. (B) Dolomitized foram of G25 outer shelf. Late calcite spare luminesces bright orange (green boxes). Scale is 200 µm. (C) Dolomitized algal fragments of the G25 foreshore in recrystallized dolomite matrix. Matrix is recrystallized by second phase dolomite, and shows euhedral habit and bright red luminescence (white arrows). Scale is 200 µm. (D) Dolomitized pisoid from the G25 shelf crest. Pore is lined by the second phase of brightly luminescent dolomite (white arrows), and filled by banded orange calcite spar (green box).

Fabric-Destructive Dolomite – Dolomite Type II

The second phase of dolomitization in Rattlesnake Canyon is composed of euhedral to subhedral dolomite crystals ranging from 20-220 μm in size. These crystals are heavily included, appearing dusty in the centers, are commonly completely fabric-destructive, and post-date stylolitization. The crystals luminesce bright red to bright orange, often with a dull, patchy center and a single brighter band around the rim (Figure 19). In combination, these factors suggest that this coarser, texturally destructive dolomite replaced either an earlier generation of dolomite or the host limestone. However, some of this dolomite also lines pores (Figure 18D) and could easily be a primary cement precipitating simultaneously to replacement.

The best exposures of this second phase of dolomite are in the reef facies of the G24 and G25, especially around clastic-filled syndepositional fractures and reef cavities, in the fractures and wall rock immediately adjacent to the Landward Fault, and in outer shelf facies near sand beds. This distribution strongly suggests that the second phase of dolomitization was controlled by the presence of syndepositional deformation features and permeable siliciclastic bodies to a much greater extent than the fabric-retentive dolomite. It also confirms field observations, which identified white haloes of dolomite around sand-filled fractures, beds, and cavities both inside and outside of the Cave Graben.

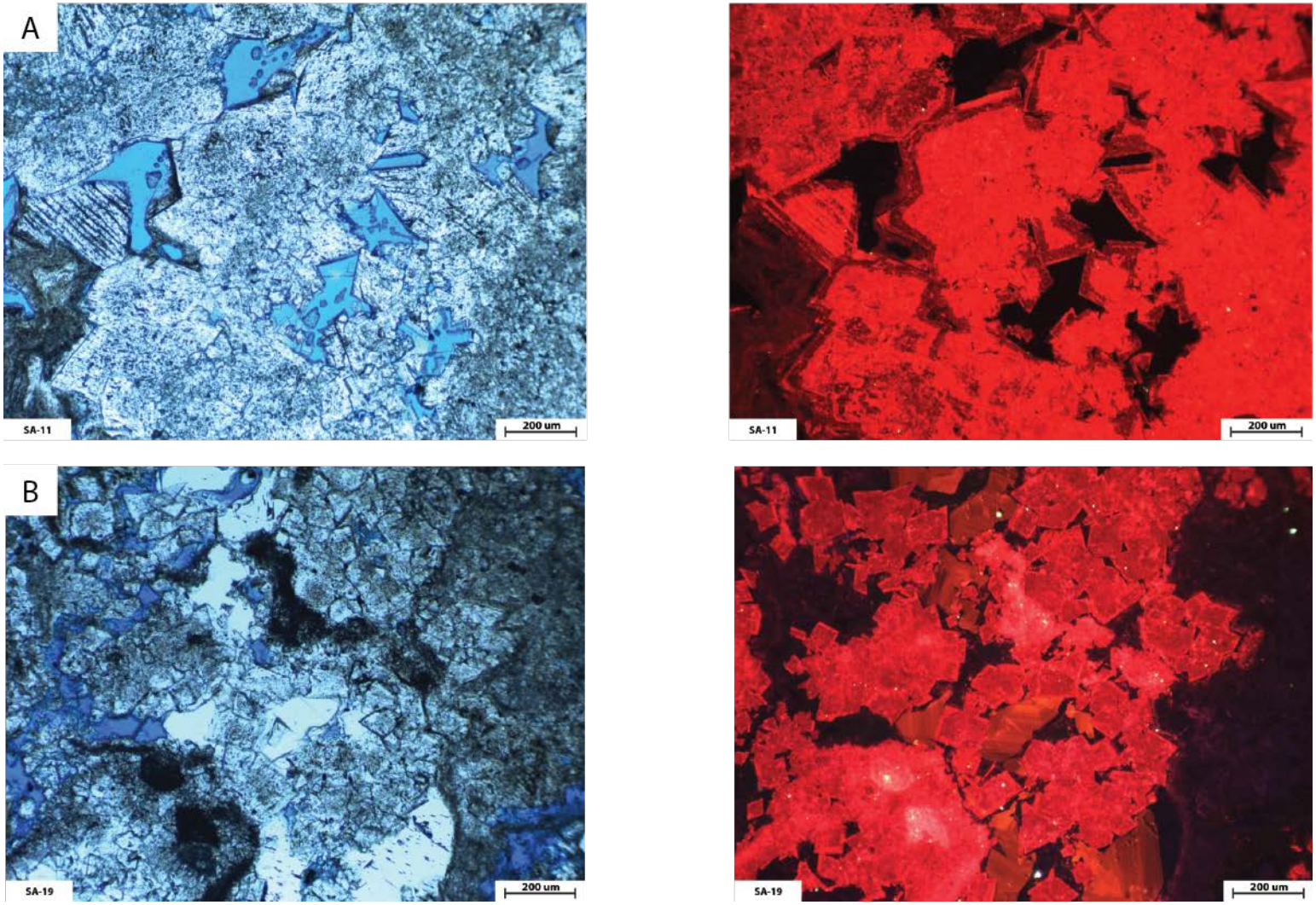

Figure 19: See below for complete caption

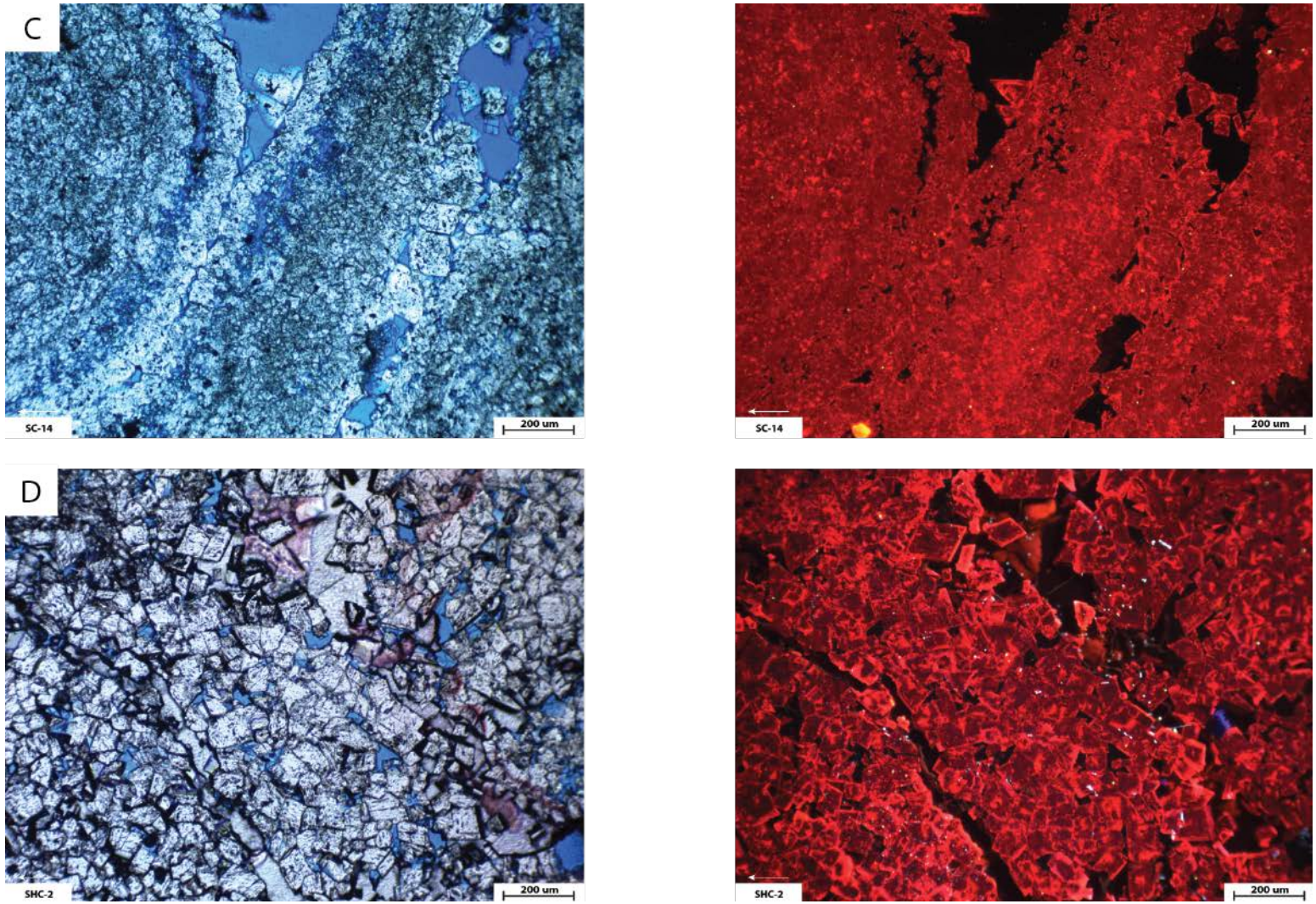

Figure 19: See below for complete caption

Figure 19—Previous Pages: Fabric-destructive dolomite crystals in plane polar and cathodoluminescence light. (A) Brightly luminescent euhedral dolomite from sand-filled fracture halo in the G24 reef. Note bright red outer rim. (B) Brightly luminescent euhedral dolomite from sand-filled fracture halo in the G24 reef. Orange banded calcite fills pores, non-luminescent calcite near right side of photo. (C) Dolomite replacement of skeletal grain, from G25 outer shelf. (D) Brightly luminescent euhedral dolomite from fracture halo in the G25 shelf crest. Scale for all is 200 µm.

The coarse, fabric-destructive dolomite has also been recognized in other regions of the Guadalupe Mountains. Melim (1991; 2002) identified a red luminescent, fabric-destructive dolomite in the forereef facies of the Capitan margin largely in Pine, Bear, and McKittrick Canyons; however, these works suggest that this fabric-destructive dolomite is rare. Mutti and Simo (1993; 1994) also identified the fabric-destructive dolomite in Slaughter, Rattlesnake, and Walnut Canyons, but also imply that dolomite Type II is rare, and further suggest that it is largely confined to the inner shelf facies and as thin cement rinds inside fenestral pores. Bishop and others (2014) similarly identified it in the pisolite shelf crest facies of Slaughter Canyon as both a replacement texture and a pore lining cement, while Budd and others (2013) saw the same in the outer shelf facies in Dark Canyon. Finally, Garber and others (1989) identified coarse, fabric-destructive dolomite in the subsurface. This study therefore provides a unique example of the distribution and abundance of dolomite Type II.

Pore Filling Calcite

Several generations of post-depositional calcite spar have also been identified in the Guadalupe Mountains, most of which fall into one of three classifications first created by Mruk (1985). Calcite Spar I is a non-luminescent to dully-luminescent zoned bladed to equant calcite that fills primary and secondary pores. This calcite is included and may overlie dolomite or pore-lining calcite, as well as replacing evaporites or filling dissolution molds. Calcite Spar II is a moderately luminescent to brightly luminescent equant to subequant zoned calcite that syntaxially overgrows Calcite Spar I and has three distinct medium/bright orange/yellow couplets overlying a dull zone. This calcite may fill pores in addition to or instead of Calcite Spar I, and is heavily included. Finally, Calcite Spar III is a non-luminescent equant spar that syntaxially overgrew Calcite Spar II,

following a period of dissolution and corrosion. This spar often fills solution pits in Calcite Spar II and forms euhedral rims on wavy, partially dissolved cores of Calcite Spar I and II. Figure 20 shows examples of all three late calcite spars.

Calcite spars are very common across the Guadalupe Mountains as well. Several studies have investigated their source, distribution, and their timing of precipitation. Mruk (1989) identified Calcite Spar I mainly in the reef facies as syntaxial overgrowths on echinoderm fragments, partial pore fill in reef cavities, and as circumgranular coatings on skeletal fragments; Calcite Spar II as a pore-filling cement in the reef and forereef; and Calcite Spar III occurs in abundance in pores of the reef and forereef, especially where dolomitization is also prevalent. Spar I is interpreted to have precipitated in the meteoric phreatic zone (Given and Lohmann, 1985, 1986; Mruk, 1989), while Spar II precipitated in a shallow burial environment with slightly elevated temperatures, from water ranging from slightly saline to marine (Mruk, 1989). Spar III is attributed to warm, saline basin-derived fluids circulating during uplift of the platform in Tertiary (Mruk, 1989). Recent works have also taken these classifications and applied them to the history of syndepositional fracturing (Budd et al., 2013), which has led them to the conclusion that syndepositional deformation features reactivate and remain open permeability conduits over extensive periods of geologic time.

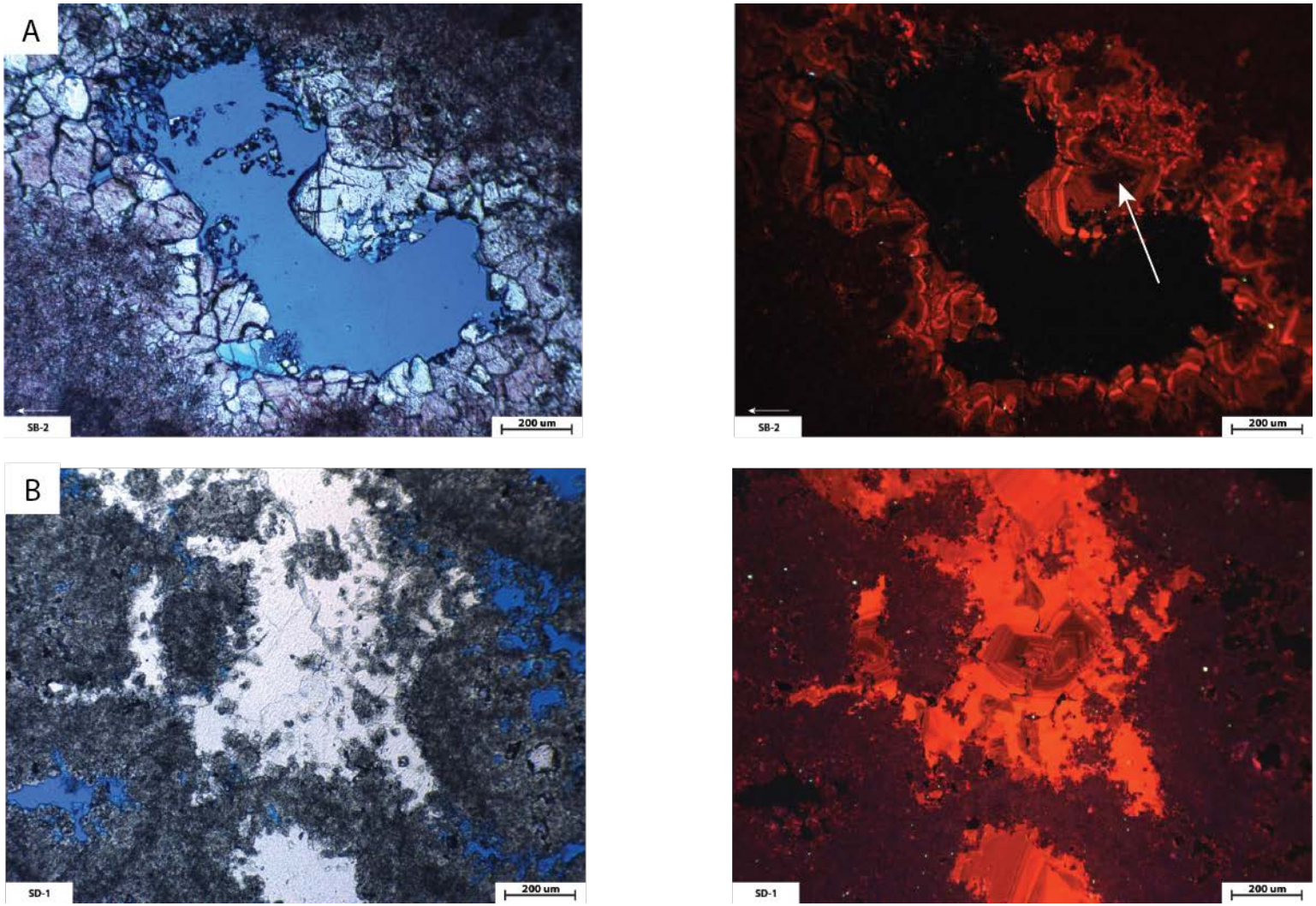

Figure 20: See below for complete caption

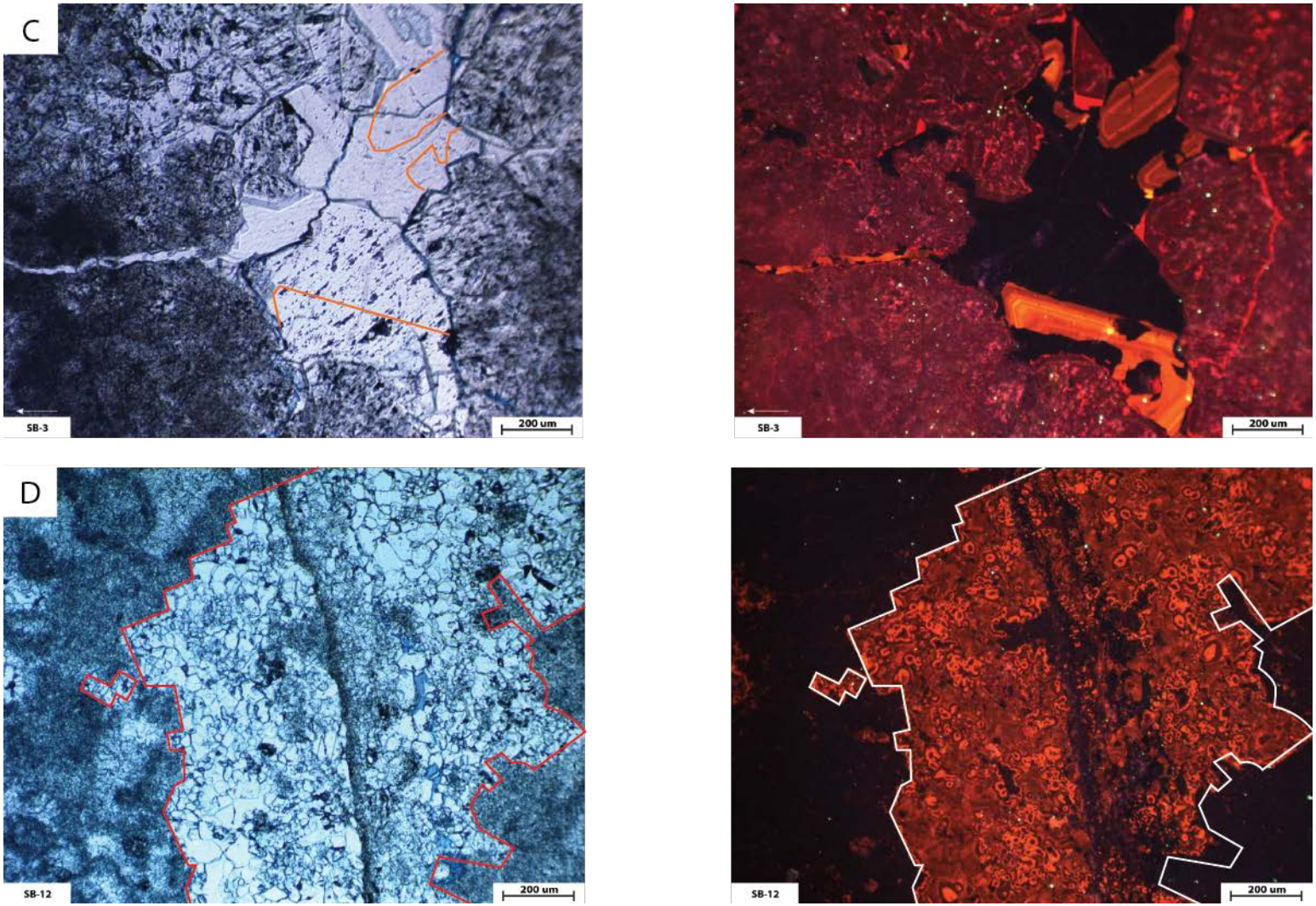

Figure 20: See below for complete caption

Figure 20—Previous Pages: Pore-filling calcite spars in plane polar and cathodoluminescence light. (A) Spar I cores (white arrow) beneath Spar II overgrowths, from G25 reef facies. (B) Pore-filling Spar II, with initial dull growth band followed by several bright zones. (C) Cores of Spar II underlying syntaxial non-luminescent overgrowths of Spar III. Spar II cores outlined in orange on plane light photomicrograph. Note solution pits in the Spar II cores, filled with non-luminescent Spar III (right). (D) Pseudomorphic Spar I and II after anhydrite. Former anhydrite crystal boundaries are outlined on plane polar photomicrograph in red, and on CL photomicrograph in white. Mottled luminescence in calcite suggests multiple nucleation points for replacement.

PARAGENETIC SEQUENCE

Efforts to determine a paragenetic sequence for the diagenetic events of the Guadalupe Mountains, either in whole or in part, have been made several times in past literature. Rahnis and Kirkland (1999, p.176) nicely summarized these works, providing a composite paragenetic sequence for diagenesis in the Guadalupe Mountains that includes "aragonitic botryoids, [radiaxial-fibrous calcite], two phases of dolomite (Melim, 1991), three phases of calcite spar (Mruk, 1985), anhydrite, magnesite (Scholle et al., 1992), and kaolinite (Melim, 1991)." More recent works have amended this generalized paragenetic sequence to include syndepositional faulting and fracturing, variable intensities and phases of recrystallization, and inclusion of earlier evaporite phases, e.g., Budd et al., 2013; Bishop et al., 2014.

The main focus of this study is the extensive dolomitization in Rattlesnake Canyon. However, the other portions of the paragenesis provide constraint on the timing of initial fracturing (e.g., syndepositional cements in fractures), and can offer unique cross –cutting relationship evidence that helps constrain the timing of dolomitization (e.g., dolomitized botryoids postdating stylolitization). Table 3 reflects a comparative paragenetic sequence for diagenetic events to include both early works and the contributions of other more recent publications, for comparison to events identified in this study. The following section will use a combination of previously published data and observations from this study to create a paragenetic sequence for this study.

Table 3: Comparative paragenetic sequences for syndepositional and post-depositional diagenesis of the Yates/Tansill Formations in the Guadalupe Mountains. Question marks in parentheses indicate uncertainty in nomenclature; question marks without parentheses indicate uncertainty in timing.

Comparative Paragenetic Sequences							
		General	**Dark Cyn**	**Slaughter Cyn**	**Slaughter Cyn**	**Rattlesnake Cyn**	**Rattlesnake Cyn**
Timing/Fluid Type		*Rhanis and Kirkland, 1999*	*Budd et al., 2013*	*Koša et al., 2003; Koša et al., 2006b*	*Bishop et al., 2014*	*Mutti and Simo, 1993; 1994*	*This Study*
Syndepositional	*Marine*	Neomorphosed Botryoid	Marine Cements	Marine Cements	Neomorphosed Botryoid	Fibrous Marine Cement	Recrystallized Botryoid
		Isopachous Calcite			Isopachous Calcite/RFC & FOC/IRP	Isopachous Marine Cement	Isopachous Calcite/RFC & FOC
						Laminated Dolomicrite	
	Meteoric					Selective Leaching of Allochems	
			Faulting/Fracturing	Faulting/Fracturing /Karst I		Faulting/Fracturing	Faulting/Fracturing
	Hypersaline	Fabric-Retentive Dolomite	Fabric-Retentive Dolomite	Fabric-Retentive Dolomite	Fabric-Retentive Dolomite	Fabric-Retentive Dolomite	Fabric-Retentive Dolomite
Post-depositional	*Mesosaline*	Fabric-Destructive Dolomite	Dolomite Cement	Fabric-Destructive Dolomite	Fabric-Destructive Dolomite	Fabric-Destructive Dolomite/Clear Dolomite	Fabric-Destructive Dolomite
	Meteoric		Dissolution		Dissolution		
		Calcite Spar I	Calcite Spar I	Calcite Spar (I?)	Calcite Spar I		Calcite Spar I
				Reactivation of Faults and Fractures/Karst II			
	Hypersaline	Anhydrite/Kaolinite	Anhydrite/Gypsum			Calcite Spar IRP/I/II	
	Meteoric			Regional Karst III?			
	Post-burial/ Meteoric	Calcite Spar II and III	Calcite Spar II and III	Late Calcite Spars (II and III?)	Calcite Spar II and III/Kaolinite	Calcite Spar III/Kaolinite	Calcite Spar II and III

Rattlesnake Canyon Sequence

In the G24 and G25 members in Rattlesnake Canyon, the earliest phases of diagenesis are marine cementation. Many of the reefal and shelf crest outcrops contain botryoidal cements, which, while presently dolomitized, show relict bladed texture suggesting an originally aragonitic mineralogy. These cements are followed by, or concurrent to, a generation of isopachous calcite cements, which are present in all facies but most common around the rims of reef cavities and around grains in the outer shelf and foreshore facies. These isopachous crusts are comprised of bladed to loafish low Mg calcite crystals that show relict texture suggestive of a high Mg precursor, and can be up to five generations thick in the outcrop window.

During marine cementation, the G24 was heavily fractured (Figure 21). These fractures were then filled with either marine cements, including isopachous calcite crusts, or by very fine siliciclastics sourced from the middle shelf, which prograded over the G24 platform margin during a relative lowstand of sea level following the G24 sequence boundary. Some of these fractures may have reactivated during the deposition of the Hairpin member, propagated up into the shelfal strata above, and were subsequently filled with shelfal-sourced skeletal material such as fusulinid forams and marine cements.

The G25 reef was similarly fractured during deposition, and the fractures are also filled with a combination of marine cements and shelf-sourced siliciclastics (Figure 22). The largest of these reefal fractures propagate up into the shelfal strata and show evidence of multiple reactivations, including both marine skeletal fills and oxidized micrite fills, often juxtaposed. These multi-generational fractures are commonly located around the landward fault and the G24 shelf margin. The margin likely provided a rigid structure over which the younger G25 shelfal deposits may have flexed and fractured.

Concentrations of syndepositional fractures over a single flexure point is not uncommon; Frost (2007) and Frost and Kerans (2009, 2010) observed similar clusters of fractures that had developed in older strata and propagated over a flexure point into younger rocks in Devonian reefs of the Canning Basin.

The top of the G25 represents not only a sequence boundary, but also a relatively substantial exposure event that lead to small-scale karstification and fracturing during the lowstand (Borer and Harris, 1989; Mutti and Simo, 1993; Mutti and Simo, 1994) (Figure 23). Preceding this exposure event, but nearing the end of G25 deposition, the faults of the Cave Graben system activated, as demonstrated by growth thickening of the shelf crest facies belt in the graben (Mathisen, in progress). Following the development of these structures, the platform top became exposed. Both the faults and the abundant horizontal and vertical fractures in the shelf crest facies tract were then filled with a deep red to bright yellow micritic sediment rich in monospecific ostracod carapaces and microcoprolites, which is suggestive of a stressed environment in which only a few particular species could survive.

Throughout all the previous events, it has been suggested that a meso- to hypersaline reflux engine located in the back reef lagoon provided a constant source of dolomitizing fluid, which is responsible for the fabric preservative dolomite that is pervasive across the outcrop window (Budd et al., 2013; Mazzullo, 1999; Melim, 1991; Melim and Scholle, 1989, 2002; Mutti and Simo, 1993; Mutti and Simo, 1994; Scholle et al., 1992; this study). Based on the fact that the fabric-retentive dolomitization follows marine cementation, but precedes all other calcite cementation, a syndepositional to immediately post depositional reflux mechanism is likely.

The possible influence of a hypersaline lagoon is also supported by the presence of evaporite minerals, which are abundant in the subsurface (Garber et al., 1989), and

pseudomorphically replaced by calcite in the outcrop (Figure 20) (Budd et al., 2013; Melim and Scholle, 1989; Mutti and Simo, 1993; Mutti and Simo, 1994; this study). These evaporite minerals are always associated with zones of dolomitization where observed in the outcrop window.

Following evaporite cementation, the deposition of the Triplet member of the Yates Formation, Tansill strata, and Ochoan-age evaporites buried the G24 and G25 up to a maximum of 1.4 km in depth (Scholle et al., 1992). This deposition led to slight reactivation of the graben faults, into which marine cements and Ocotillo Silt (Tansill-age clastic material, G28) later migrated. Additionally, during burial, a second phase of dolomitization occurred, recrystallizing dolomitized strata immediately proximal to reactivated syndepositional faults, syndepositional fractures filled with clastic material (and to a lesser extent, marine cement), and facies with high original interparticle porosity (Figure 23). While it is difficult to isolate this event into a specific time period, several samples show that fabric-destructive dolomite postdates stylolitization (Figure 16), which is a strong indicator that the diagenesis occurred post-depositionally.

Finally, nearing the end of burial and during Tertiary exhumation, major reactivation on both faults of the Cave Graben occurred, dissolution and karsting on a massive scale widened faults and fractures and led to the formation of major cavern networks, and precipitation of the pore-filling calcites took place (Mathisen, in progress). The first calcites are assumed to be precipitated from warm basinal fluids, while the non-luminescent overgrowth phase is attributed to the presence of a meteoric freshwater lens which developed during uplift (Budd et al., 2013; Scholle et al., 1992). These calcites are common across the Guadalupe Mountains, and have even been identified inside caverns as sparry calcite precipitates (Hill, 1999; Lundberg et al., 2000).

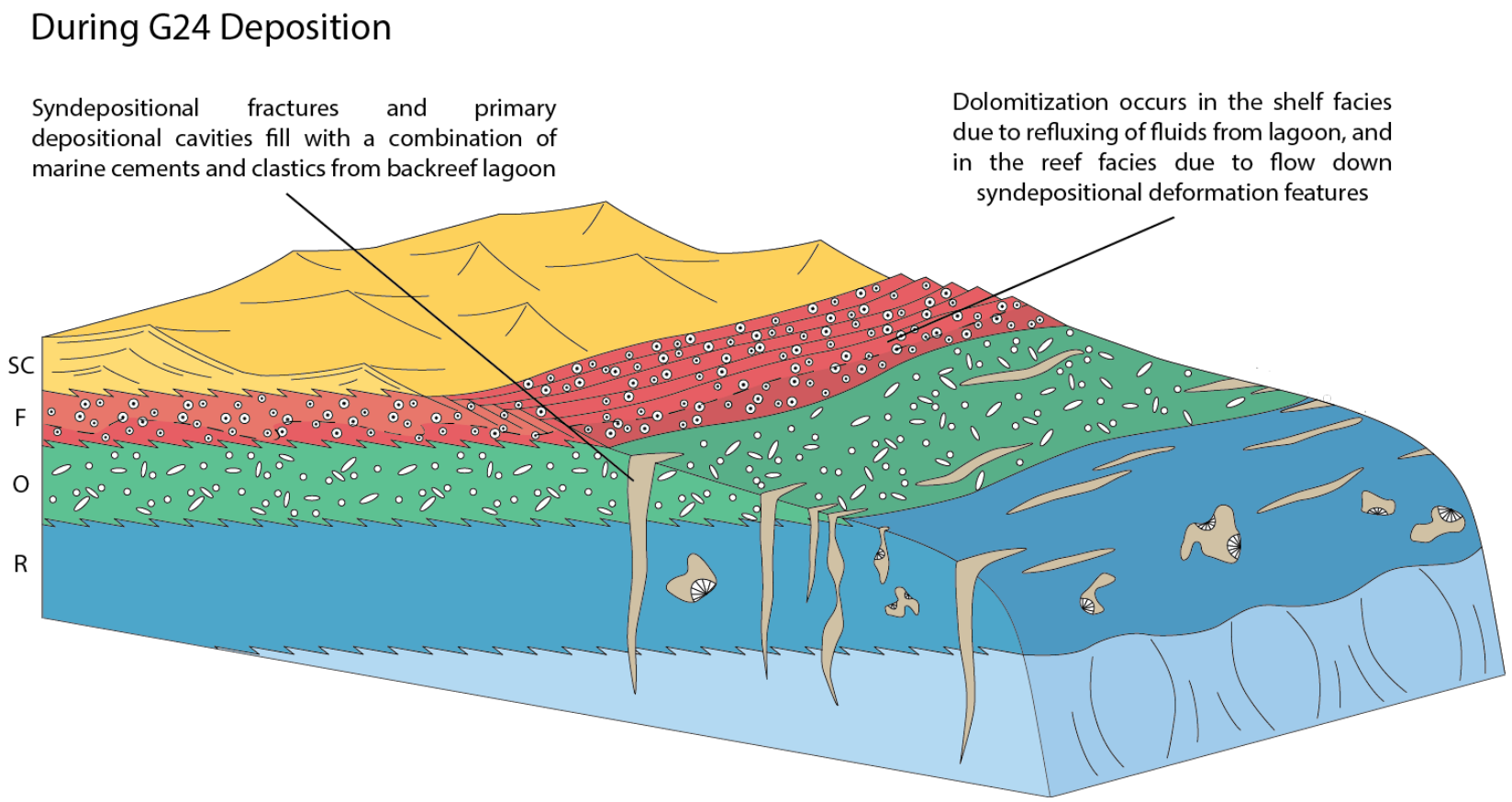

Figure 21: Schematic representation of the syndepositional deformation and diagenesis occurring during G24 deposition. Syndepositional fractures initiate in the G24 reef, and fill with a combination of marine cement and shelf-derived clastic material. Dolomitizing fluid penecontemporaneously passes through permeable zones of partially cemented shelf facies.

During G25 Deposition

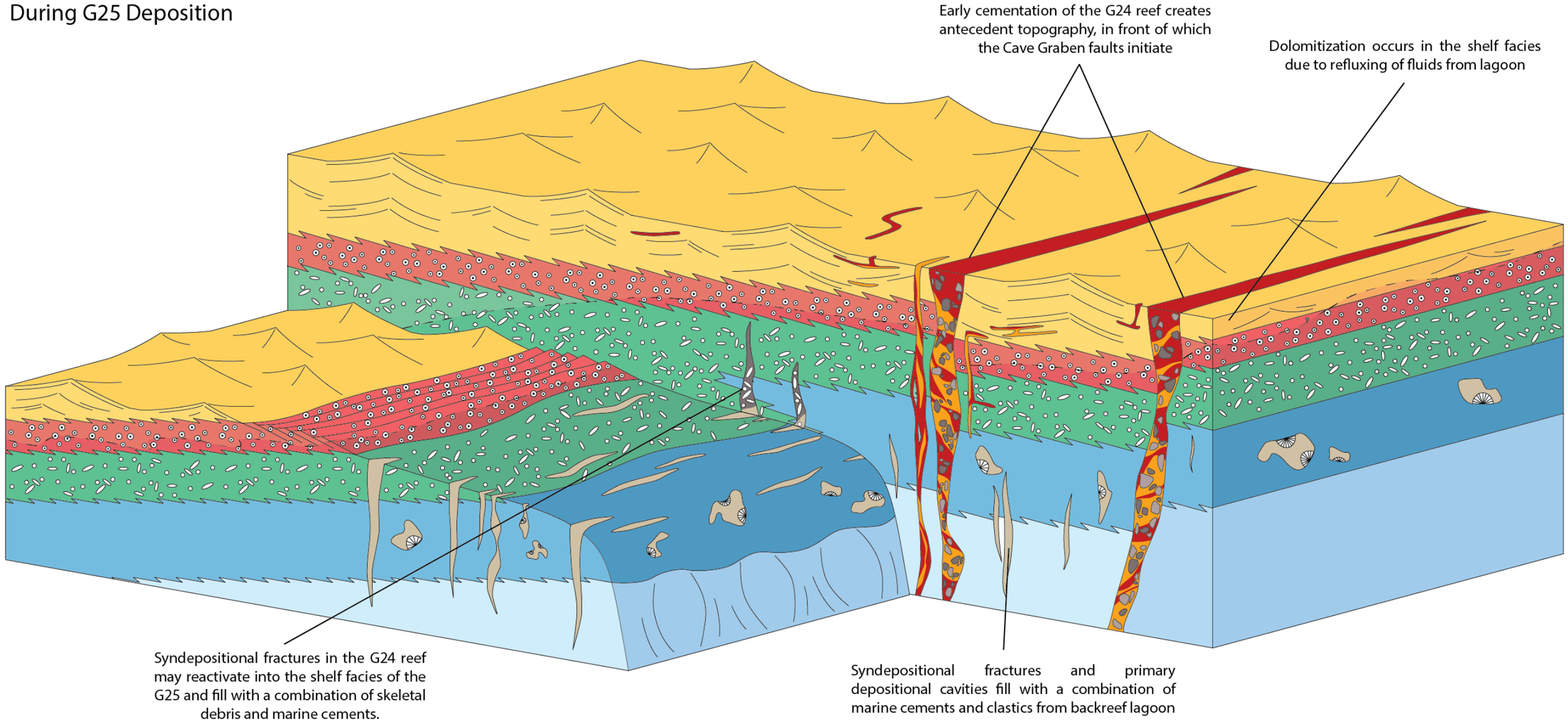

Figure 22: Schematic representation of syndepositional deformation and diagenesis occurring during G25 deposition. The early cemented, rigid G24 shelf margin provides antecedent topography over which the G25 shelf strata flex. This flexure allows the Cave Graben faults to form. Faults are first filled with a layer of early marine cement. Pre-existing fractures may reactivate and propagate upward in to the shelfal strata of the G25. Dolomitizing fluid continues to penecontemporaneously pass through the shelfal strata.

After G25 Deposition/Shallow Burial

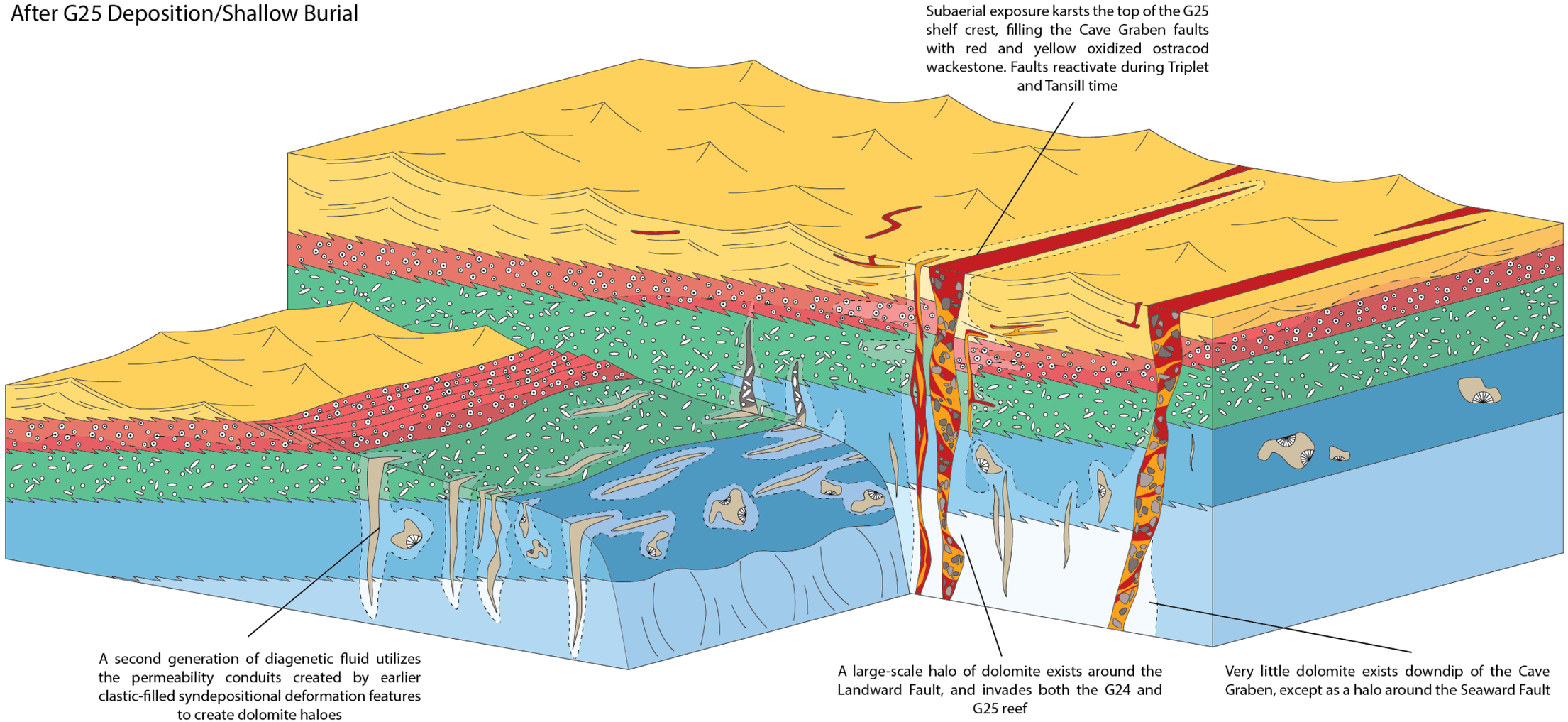

Figure 23: Schematic representation of the syndepositional deformation and diagenesis occurring after deposition of the G25/during burial. Karsting and meteoric dissolution widens the Cave Graben faults, which fill with oxidized wackestone. Further activation and offset occurred during subsequent burial. Dolomitization occurs during burial within and around syndepositional faults and fractures, especially those filled with clastic sediments that retained higher permeability. Fingers of dolomite extend along sequence boundary sands (not shown) and into grainy permeable beds where syndepositional deformation features intersect.

In general, the paragenetic sequence determined from samples in the G24 and G25 window for this study is very similar to those sequences which have previously been constructed, both in Rattlesnake Canyon and elsewhere in the Guadalupe Mountains. The overall timing of cementation, faulting and fracturing, and dolomitization are consistent with earlier studies, including Melim's dolomitization studies (1991; 1989), Koša and Hunt's faulting and fracturing studies (2002; 2006a; 2003; 2000), and combination studies by Frost and others (2012), and Budd and others (2013). The petrographic cross-cutting relationships suggest that the fabric-retentive dolomite generation formed immediately after syndepositional cementation, while the fabric-destructive generation of dolomite formed during burial. The following chapter will present geochemical data, and will use these interpreted times of dolomitization as additional constraint on the most likely sources of dolomitizing fluid responsible for each generation.

CHAPTER 4 — GEOCHEMICAL ANALYSIS

Having established a qualitative petrographic paragenetic sequence for calcite and dolomite generations present in Rattlesnake Canyon, trace element and stable isotope data were collected from Type I and Type II dolomite, and luminescent calcite to provide quantitative evidence for the source of the fluids. Trace element data were collected in the UT Microprobe Laboratory on a JEOL JXA-8200 WD/ED Combined Electron Microprobe; calibration standard information and operating conditions can be found in Table 4 and Table 5. Carbon and oxygen isotope data were collected at the Bureau of Economic Geology on a Thermo-Finnigan Delta V Isotope Ratio Mass Spectrometer with a GasBench II prep device. Operating conditions can be found in Table 6.

Table 4: Calibration standards used during calcite and dolomite trace element analysis.

Standard Calibration Data			
Element	**Detector**	**Crystal**	**Calibration Standard**
Ca	2	TAP	T-48 Dolomite
Mg	3	PETH	T-53 Calcite
Mn	4	LIFH	UNSM R2460 Siderite
Fe	5	LIFH	UNSM R2460 Siderite

Table 5: Microprobe operating conditions for calcite and dolomite Mn^{2+} and Fe^{2+} trace element analysis.

Microprobe Operating Conditions	
Voltage	15 KeV
Beam Current	10.031 nA
Probe Diameter	15 um

Table 6: Mass spectrometer operating conditions for dolomite stable isotopic analysis.

Mass Spectrometer Operating Conditions	
Standard Name	UT Vein Calcite
Standard Weight	~325 µg
Digestion Temp	50°C
Digestion Duration	13 hr
Filament Type	Tungsten (W)

TRACE ELEMENT ANALYSIS

Cathodoluminescence in carbonate minerals is due to the inclusion of manganese and other foreign ions into the crystal lattice. Commonly these elements are only present in trace amounts, with luminescence visible at as little as 10 – 20 ppm Mn^{2+}, assuming that total iron concentrations are less than 150 ppm (Machel and Burton, 1991; Machel et al., 1991). It has been proven that, in addition to Mn^{2+}, Pb^{2+}, several rare earth elements including Eu^{3+} and Tb^{3+}, Cu^{2+}, Zn^{2+}, and Ag^{+} also activate luminescence in carbonates. These ions can subsequently be sensitized by additional lattice substitutions such as Pb^{2+}, $Ce^{2+/4+}$, or quenched by the inclusion of Fe^{2+}, Ni^{2+}, and Co^{2+} (Machel, 1985). However, since Mn^{2+} is perhaps the most common activator of luminescence and the colors observed in my sample are consistent with a Mn^{2+}/Fe^{2+} system, only manganese and iron were analyzed for this study and are assumed to be the only substantial activator and quencher.

Previous works have acknowledged that manganese substitutes readily for magnesium in dolomite (Banner and Hanson, 1990; Barber, 1974; Wildeman, 1970), has a distribution coefficient greater than unity (Swart, 2009), and is generally enriched in diagenetic waters (Banner and Hanson, 1990; Land, 1980), but have also indicated that manganese partitioning is dependent on the rate of precipitation, the Mn^{2+}/Ca^{2+} of the parent solution (Morse and Mackenzie, 1990), and the system E_h conditions (Banner and Hanson, 1990). This wide variety of controls on Mn^{2+} partitioning into dolomite makes the interpretation of a fluid composition from trace element data challenging, which will be considered below.

Sample Selection and Methods

As discussed in the previous chapter, there is a noticeable qualitative increase in luminescence between the Type I fabric-retentive dolomite common to the shelf crest facies belt, and Type II sub- to euhdral, fabric-destructive replacement dolomite that is abundant in the G24 and G25 reef and demonstrates a distinct spatial tie to syndepositional faults and fractures. Five thin sections were chosen as representation of these two end-members for trace element analysis: three from the top bench of the G25 (Hairpin) shelf crest tepee-pisolite facies, one from the G24 (Corral) Reef, and one from the G25 (Hairpin) Reef. The three "SHC" samples from the G25 shelf crest contain both Type I and Type II dolomite; the former is present in replaced pisoids, while the latter is present as patchy linings to pore throats, as replaced botryoids around sheet cracks and fractures, and occasionally as porosity-occluding fill. Alternatively, both reef samples are comprised almost entirely of Type II dolomite, which has destructively replaced the original reef fabric. One sample, SA-11, is from approximately 100 m landward of the Cave Graben fault system, while the other, SD-5, is from immediately adjacent to the Landward Fault and has the brightest luminescence of any sample collected throughout the study. These thin sections were coated with a 20 μm thick layer of sputtered carbon to prevent charging during analysis.

For each sample, three to four multi-spot transects were analyzed, each with a minimum of 15-20 spots spaced between 20-30 um apart. In the three shelf-crest samples, these transects were designed to begin within a pisoid that had dull luminescence and was categorized as Type I dolomite, and to end within a Type II dolomite botryoid or pore lining. For comparison, at least two transects each of exclusively Type I and Type II dolomite were also analyzed from the three samples. Next, similar transects of at least 15-20 spots spaced 25-30 um apart were analyzed from each reef sample, though because

both reef samples are comprised entirely of Type II dolomite, these transects simply crossed from the centers of crystals to the edges. Finally, a single transect was analyzed through the dully luminescent pore-filling calcite. Figure 24 shows examples of two transects on the secondary electron images generated by the electron microprobe, both through Type II dolomite.

Results

Data from the electron microprobe were returned as percent oxides CaO, MgO, MnO, and FeO, to total 100%. Accuracy and precision were determined based on a set of calibration standards analyzed prior to the unknowns (Table 4). The dolomite standard (T-48 dolomite) was also re-analyzed as an internal standard multiple times throughout the total duration of the microprobe run. This internal standard was used to monitor and correct for instrumental drift. The data for each unknown were then filtered on two criteria: (1) any spot that returned a total percent oxide less than 95% was excluded, and (2) any spot that returned a negative MnO or FeO value was also excluded. The remaining data points from each transect were included in the analysis.

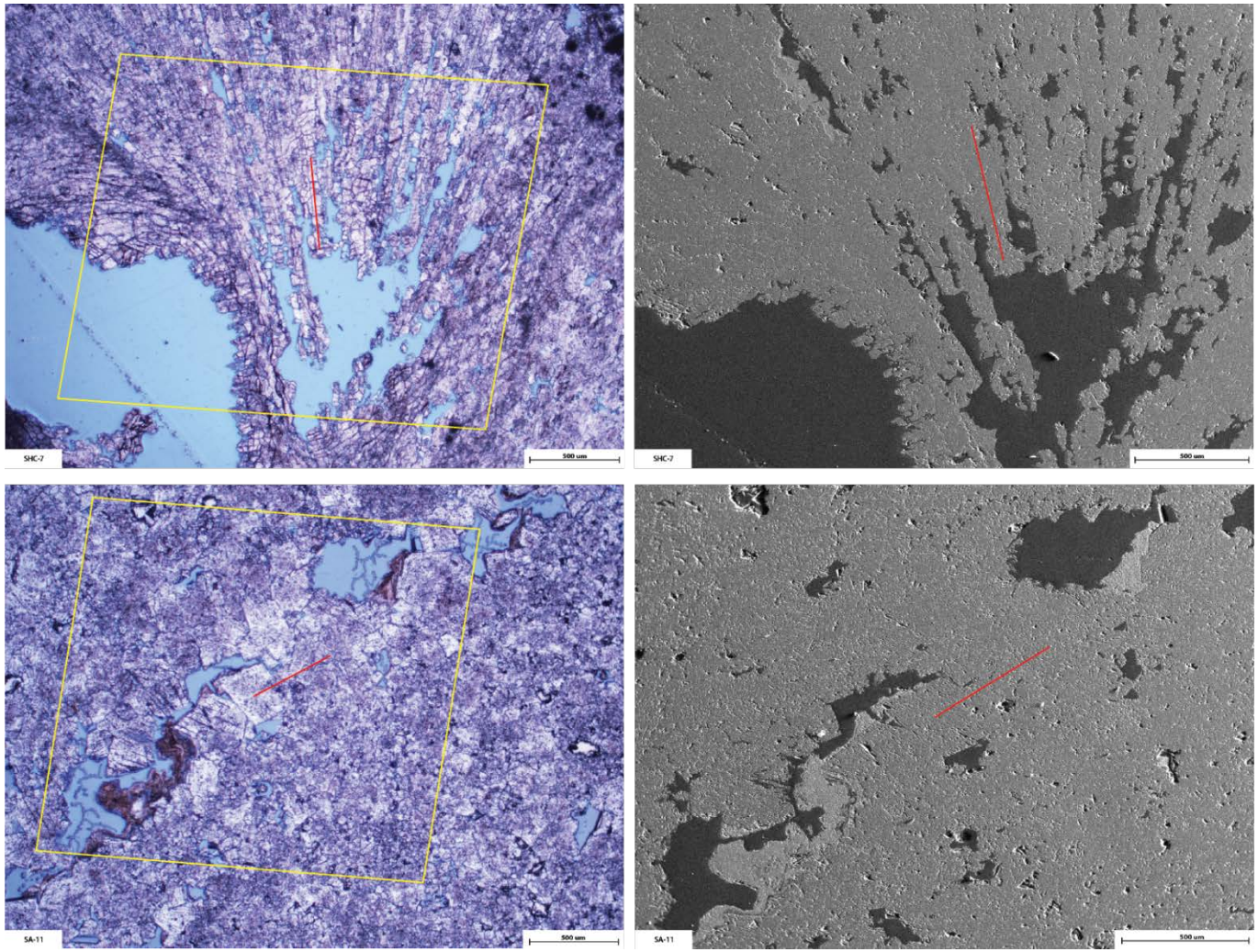

Figure 24: Plane polar and secondary electron images of two microprobe transects. SE image outlined in yellow on plane polar photomicrographs; transects indicated by red lines.

Data show that Type I dolomite contains up to an order of magnitude less Mn^{2+} and up to an order of magnitude more Fe^{2+} than Type II dolomite (Figure 25). Either of these differences can explain the increased brightness seen in Type II dolomite: lower concentrations of iron may have less of a quenching effect on the luminescence for two samples with equal quantities of manganese; and higher concentrations of manganese may activate a stronger luminescence for two samples with equal quantities of iron. There is a small amount of overlap between the Type I and Type II zones which may be an artifact of the large spot size used to prevent sample destruction during analysis.

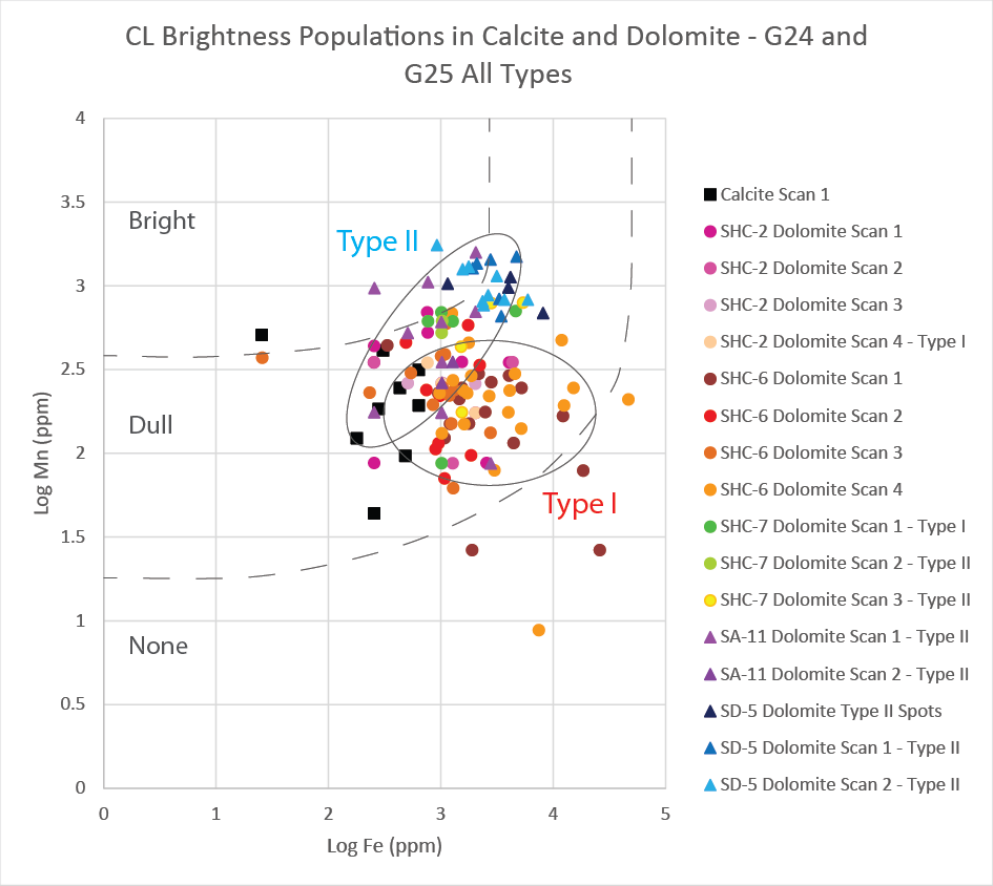

Figure 25: Log-log plot of Mn^{2+} and Fe^{2+} concentrations for all samples. Scans lacking a "Type I" or "Type II" modifier in the legend indicate transects that cross from Type I into Type II dolomite. Samples with a circular marker are from the G25 shelf crest facies tract, while samples with a triangular marker are from the G24 and G25 reef. Brightness zones after Machel and Burton (1991).

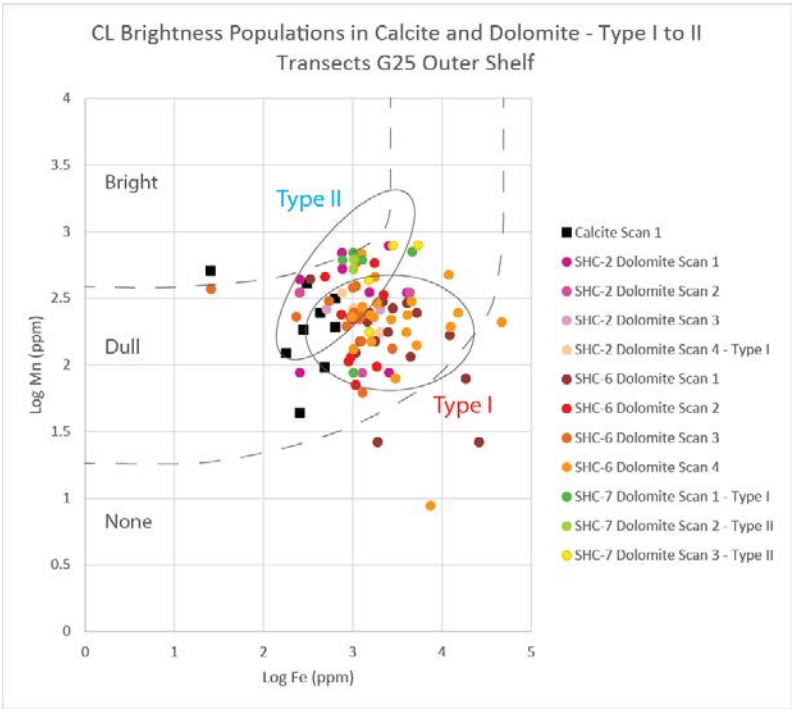

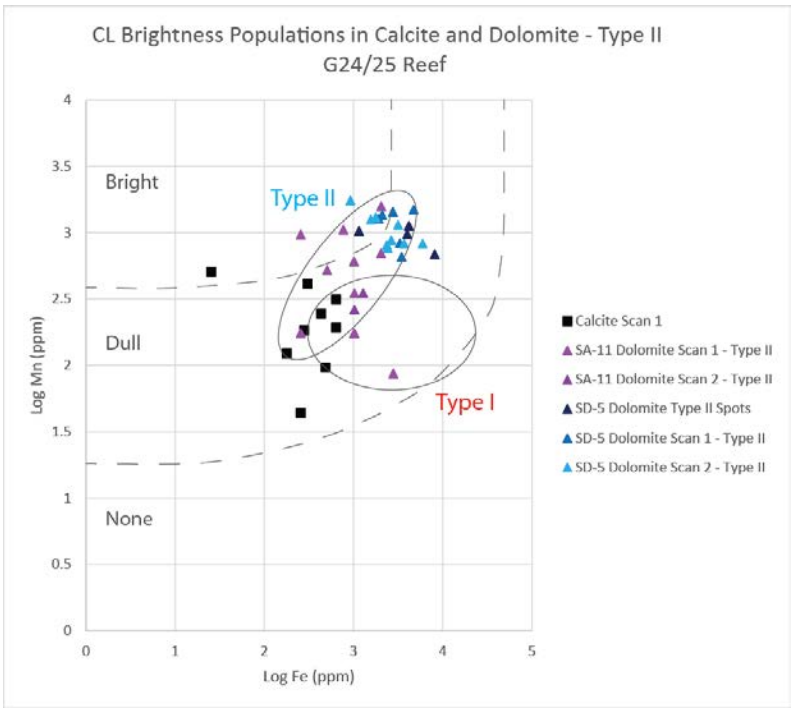

Figure 26: Log-log plots of the Mn^{2+} and Fe^{2+} concentrations in all samples, separated by facies belt. (Top) All samples from the G25 shelf crest, including Type I and Type II dolomite only scans, and I-II transects. (Bottom) All samples from the G24 and G25 reef, both of which were previously classified as exclusively Type II dolomite from CL and petrographic analysis.

Two distinct populations are visible when the analyses are separated by facies belt, and consequently, dolomite type (Figure 26). A majority of the spots from the G25 shelf crest, which is dominantly Type I dolomite with patchy Type II pore linings, cluster squarely in the dull zone of the plot, though there are scattered spots approaching the Type II and bright sectors (as the transects crossed between dolomite types). Alternatively, both the G24 and G25 reef samples that are purely Type II dolomite fall much closer to the bright zone, contain measurably higher concentrations of Mn^{2+}, and frequently also hold much lower concentrations of iron, increasing their luminescence.

Analysis

The identification of two distinct dolomite trace element populations, showing up to an order of magnitude of difference for Mn^{2+}, is possible evidence that supports the interpreted syndepositional and burial dolomitization events in Rattlesnake Canyon. The Type I dolomite is interpreted to have formed very early in the life of the platform, postdating only syndepositional marine cementation. As such, this dolomitization event was likely occurring in oxidizing surface conditions, which may have prevented manganese from effectively partitioning into the dolomite crystals and contributed to the low trace element concentrations and dull luminescence. Comparatively, Type II dolomite is interpreted to have formed during burial, as it postdates stylolitization and has much coarser crystals. The subsurface conditions are much more likely to be reducing, which would have allowed manganese to partition into dolomite efficiently. This could easily explain the higher concentration of manganese and the bright luminescence of dolomite II. These results do not, however, provide distinct evidence for a specific fluid source; stable isotope analysis will address this question in the following section.

STABLE ISOTOPE ANALYSIS

Stable carbon and oxygen isotopes were analyzed in an effort to gain insight into the fluid sources of each diagenetic phase. Carbon isotopes in shallow water carbonates tend to be biologically mediated, and largely influenced by organisms, vegetation, or soil processes. Additionally, because of the relative insolubility of CO_2 and depending on the water/rock ratio, most diagenetic phases inherit the carbon isotope signature of the precursor mineral than that of the diagenetic fluid (Banner, 1986; Land, 1980) due to the proportion of ions in the rock versus the fluid. Oxygen isotopes, on the other hand, are strongly water-buffered and are highly temperature dependent, making them generally more difficult to interpret in dolomitized strata due to a poor understanding of kinetic controls on dolomite recrystallization (Land, 1983). However, because they are water buffered, the oxygen isotope ratios are more useful in determining a diagenetic environment than the carbon isotope ratios are. As such, the oxygen isotope data in this study will be interpreted in tandem with petrographic observation, knowledge of the sequence stratigraphy of the Yates Formation, and with the above trace element data, so that uncertainty from one data set may be tempered by data from another.

Stable isotopes are also useful indicators of paleoenvironment and ocean conditions. Given and Lohmann (1985) used carbon and oxygen isotope ratios to investigate early marine aragonite and high Mg calcite cements from multiple canyons along the Permian Reef, and concluded that the composition of aragonite in equilibrium with seawater in the Permian Basin during the Guadalupian was +5.2‰ $\delta^{13}C$ and –2.8‰ $\delta^{18}O$, relative to the Vienna Pee Dee Belemnite global carbonate standard, or -1.4‰ $\delta^{18}O$ relative to VSMOW (at 25°C). These values are significantly enriched compared to Permian marine calcite compositions outside the Guadalupe Mountains (+2‰ $\delta^{13}C$, -5‰ $\delta^{18}O$ VPDB) (Veizer et al., 1999), which the authors attribute to a slightly restricted basin

architecture preceding Ochoan time. The Permian Basin isotopic values +5.2‰ $\delta^{13}C$ and –2.8‰ $\delta^{18}O$ will be used as the Permian marine carbonate benchmark for this study, though it is worth noting that due to differences in fractionation behavior, direct comparison of aragonite and dolomite should be done with caution.

Sample Preparation and Methodology

Samples for isotopic analyses were drilled from the thin section billets using a variety of micro-burrs. Separation of the two dolomite phases during drilling was performed when possible, but several of the thin sections show evidence for a variable degree of recrystallization between Type I dolomite to Type II dolomite. In these cases, bulk sampling was performed, and data returned are expected to fall between those of the two end members in a similar fashion to the trace element concentrations; these will be classified as “mixed” dolomite.

All dolomite samples were then leached in a 1 M solution of acetic acid, buffered by ammonium acetate (pH of approximately 5), for 10 minutes before being thoroughly rinsed with de-ionized water, centrifuged, and placed in a drying oven for one hour (Baker and Burns, 1985; Burns and Baker, 1987; Malone et al., 1994). This process removes calcite phases with minimal destruction of dolomite, effectively preventing interference from the preserved limestone, late luminescent calcite and modern tufa calcite that were inadvertently sampled during bulk collection. Four of these samples were run through an Olympus BTX Benchtop XRD before and after the acid leach process to confirm the efficiency of the procedure, the results of which can be seen in Figure 27. Note that the BTX XRD uses a cobalt radiation source, and the peaks are therefore shifted slightly to the right along the 2θ axis compared to standard *K*α intensity spectra generated by a copper-source XRD.

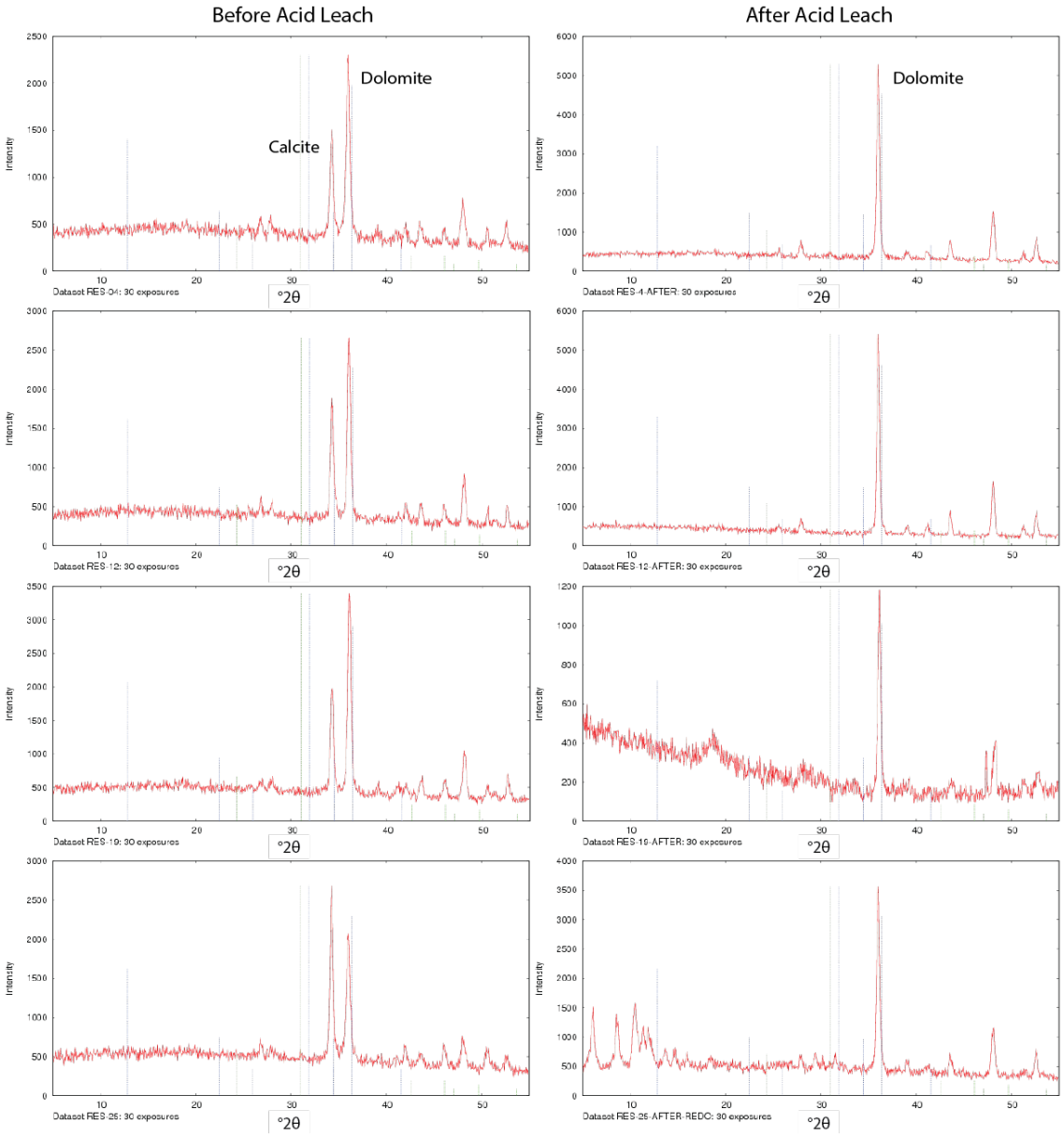

Figure 27: XRD intensity spectra for four mixed mineralogy samples, analyzed before and after leaching in a 1M buffered acetic acid solution (pH approximately 5). The main dolomite peak plots at approximately 36° 2θ, with the main calcium peak located immediately to the left. Sample RES-19-AFTER (right column, second from bottom) is noisy due to a slightly smaller sample volume. Sample RES-26-AFTER-REDO (right column, bottom) contains a small amount of residual calcium acetate salt in the low 2θ range that will not interfere with stable isotopic analysis.

After drying, samples were weighed at between 300 and 350 μg on average into 12 mL Exetainer vials, capped, and placed in a gas bench prep device. Each vial was purged with dry He gas for 3 minutes, then acidified with anhydrous phosphoric acid. The sample material was allowed to equilibrate for 13 hours at 50°C. Liberated carbon dioxide gas was then sampled from each vial and directed into the Delta V.

Results

Carbon and oxygen isotope ratios are reported in standard delta notation with respect to the Vienna Pee Dee Belemnite (VPDB) global calcium carbonate standard, with a analytical error of the mean of less than 0.1‰. Precision and accuracy for these analyses was based on the repeated analysis of an internal lab standard, UT Calcite, which is a vein calcite from Utah with a $\delta^{13}C$ value of 1.9‰ and a $\delta^{18}O$ value of -18.4‰ relative to VPDB, as well as the replicate analyses of three unknown samples. Data were corrected for $\delta^{17}O$ interference using the Craig correction factor (1957), and no instrumental drift correction or phosphoric acid fractionation correction were necessary. Samples that returned a voltage lower than 11V were excluded from final analysis.

Carbon and oxygen isotope data show that the two previously suggested dolomite types have distinct, though slightly overlapping isotopic signatures (Figure 28). In general, dolomite Type I has higher carbon and oxygen ratios compared to Permian marine carbonate and other dolomite, with average values of 6.8‰ $\delta^{13}C$ and 2.8‰ $\delta^{18}O$ VPDB. Comparatively, dolomite Type II is slightly oxygen-depleted compared to the earlier generation of dolomite, with average values of 6.2‰ $\delta^{13}C$ and 1.5‰ $\delta^{18}O$ VPDB. These average values for each can be seen in Table 7, while the entire dataset is presented in Appendix B.

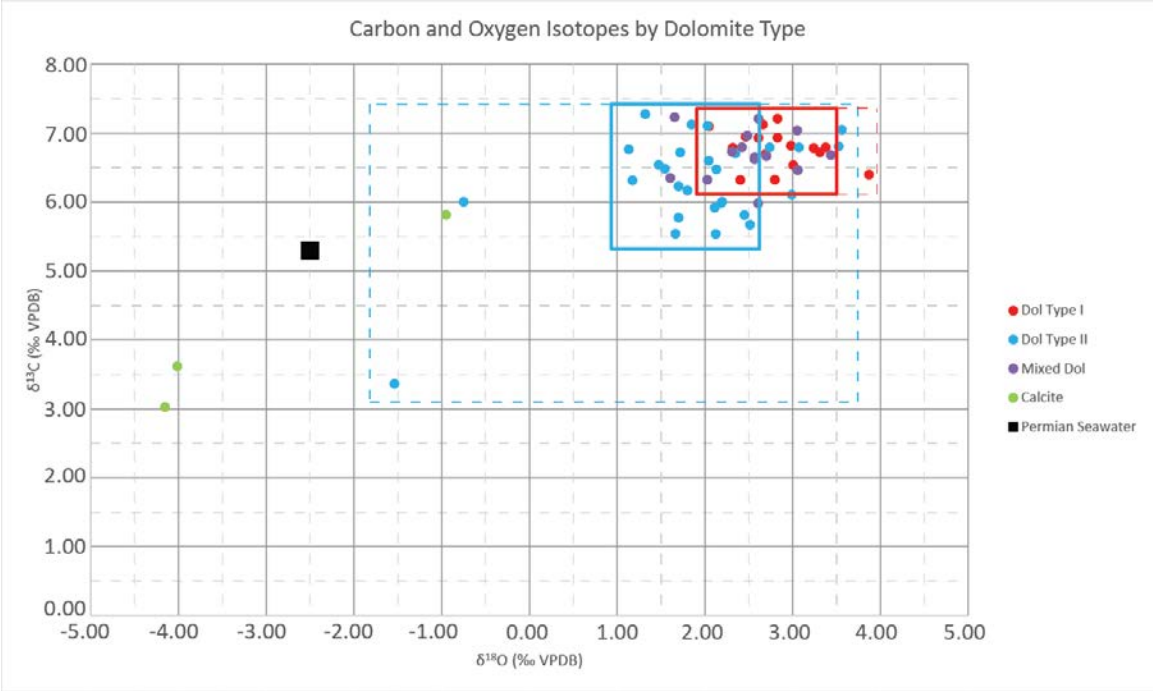

Figure 28: Carbon and oxygen isotopes ratios, grouped by dolomite type. Dolomite Type I is outlined in solid red; outliers fall within limits of dashed box. Dolomite Type II is outlined in solid blue; outliers fall within limits of dashed box. Dolomite samples with conflicting characteristics, (e.g., partial fabric destruction but dull luminescence, or fabric-retention but bright luminescence) are classified as "mixed" dolomite (purple). Calcite samples from undolomitized facies shown in green. Permian aragonite (Given and Lohmann, 1985) represented by black square.

Table 7: Average stable isotope ratios and 2σ standard deviation by dolomite type. Limestone refers to a mixture of stabilized low Mg calcite from undolomitized reef facies and minor late pore filling component (proportions unknown); Permian Aragonite refers to values determined for primary marine aragonite by Given and Lohmann, (1985).

Average Isotope Values by Dolomite Type		
Isotope Ratio	**Average Value (‰)**	**Standard Deviation (2σ)**
$\delta^{18}O$ – Dol I	2.84	0.91
$\delta^{13}C$ – Dol I	6.78	0.55
$\delta^{18}O$ – Dol II	1.53	3.04
$\delta^{13}C$ – Dol II	6.24	1.50
$\delta^{18}O$ – Mixed Dol	2.31	1.82
$\delta^{13}C$ – Mixed Dol	6.67	0.69
$\delta^{18}O$ – Limestone	-3.04	3.62
$\delta^{13}C$ – Limestone	4.16	2.94
$\delta^{18}O$ – Permian Aragonite	-2.80	–
$\delta^{13}C$ – Permian Aragonite	5.20	–

Stable isotopes also show some clustering based on the facies from which the sample was taken (Figure 29). In general, shelf crest samples have higher $\delta^{13}C$ regardless of dolomite type, while the reef, foreshore, and outer shelf samples are slightly depleted in ^{13}C, comparatively. These elevated $\delta^{13}C$ ratios in the shelf crest samples are comparable to $\delta^{13}C$ taken from the Tansill shelf crest facies in Dark Canyon (Frost et al., 2012), to $\delta^{13}C$ from the Yates shelf crest further updip in Rattlesnake Canyon (Mutti and Simo, 1993; Mutti and Simo, 1994), and to backreef Yates and Tansill $\delta^{13}C$ from the southern portion of the Guadalupe Mountains (Melim, 1991). They are, however, slightly enriched compared to reef, outer shelf, and forereef samples from Dark Canyon and McKittrick Canyon (Frost et al., 2012; Melim, 1991).

Partitioning by facies is similarly observed in the oxygen isotope ratios, though not as clearly as in the carbon isotopes. Shelf crest and reef oxygen values are the most variable, with both populations falling between +1 and +3‰ VPDB (the former favoring the light end, and the latter favoring the heavier), while foreshore samples are between +2 and +3‰, and outer shelf facies are the most depleted at between +1 and +2‰ (Figure 29). Again, these clusters are comparable to samples from Tansill strata in Dark Canyon, which shows oxygen-enriched reef facies, depleted outer shelf facies, and intermediate shelf crest facies (Frost et al., 2012). There may additionally be a correlation between the degree of recrystallization of dolomite Type II, and the depletion of oxygen isotopes, as first suggested by Melim (1991). For example, reef samples with the lowest $\delta^{18}O$ isotopes tend to be those that have been completely recrystallized by fabric-destructive dolomite, while the reef samples that show ^{18}O enrichment, despite being classified as dolomite Type II due to very bright luminescence, are generally slightly better preserved and have much smaller crystal sizes.

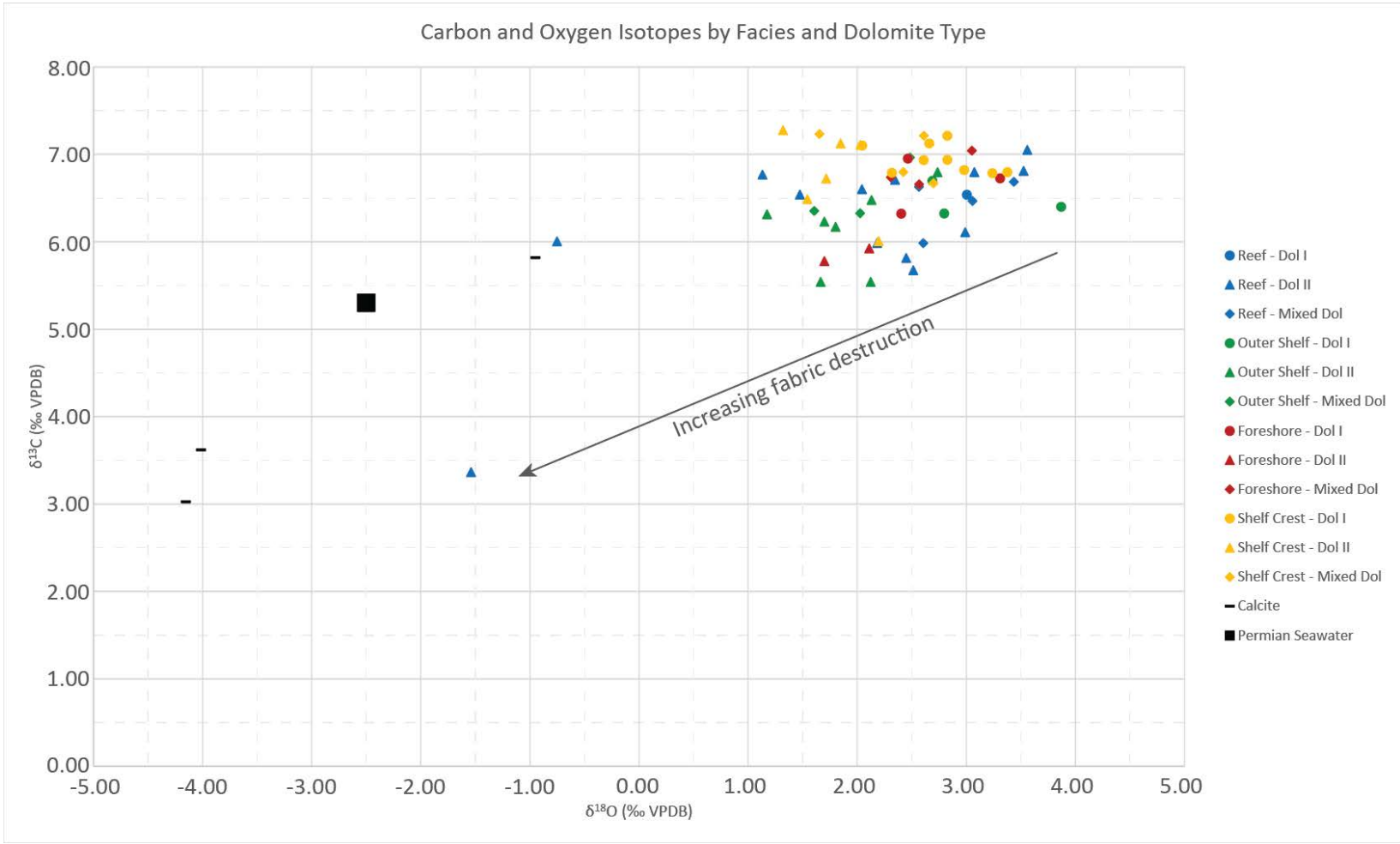

Figure 29: Carbon and oxygen isotope ratios, colored by dolomite type and by facies. Circles are used to identify dolomite Type I, triangles are used to identify dolomite Type II, and diamonds are used to identify "mixed" dolomite. Permian Aragonite value from Given and Lohmann, (1985).

Sources of error that may have contributed to the dramatic shift in the two outlying points shown above are uncertain. The acid leach preparation procedure eliminates contamination from calcite during sampling, and weighing materials including spatulas, weighing paper, and vials were all thoroughly cleaned before and during use to prevent contamination after acid leaching. It is also unlikely that the data points are the result of an operation error in the mass spectrometer—several samples that did not generate enough carbon dioxide to meet the 11V cutoff plotted in the same region as the outliers, but they were culled from the data before analysis. The remaining outliers did not fall below this 11V cutoff. With these two main sources of error eliminated, one must assume that the two outlying points are legitimate data that are simply anomalous compared to the majority of the population, but further analysis will both include and exclude them in an effort to address all possible likely scenarios.

Analysis and Interpretation

Interpreting a dolomitizing fluid source and timing of migration is difficult, due to the poor understanding of dolomitization kinetics and the strong temperature control on oxygen isotope fractionation. To make an estimate of the fluid composition, with which the dolomite is assumed to be in equilibrium, an estimate of the fluid temperature must be made. This is done using the fractionation equation determined by Land (1985), which is:

$$10^3 \ln \alpha = \frac{2.78 \times 10^{-6}}{T^2} + 0.91$$

The term $10^3 \ln \alpha$ is a term that represents the difference in per mil (‰) between the dolomite and its corresponding fluid, at equilibrium, at temperature (T) in degrees Kelvin. Though this equation was derived from higher-temperature experimental generation of dolomite, it is still considered the best approximation for calculations in low temperature dolomitization.

Estimates of the temperatures of dolomitization were made twice, once for each dolomite, based several assumptions. Based on published values for the Permian Basin, a standard geothermal gradient of 25°C/km was used, as well as a surface temperature minimum of 20°C (Scholle et al., 1992) and a conservative maximum of 30°C (Moore and Peoples (1990) suggest maximum surface temperatures in the Kazanian may have even exceeded 40°C), and a maximum burial depth of 0.75 kilometers for the upper Capitan (Scholle et al., 1992) (Figure 30). Additionally, Type I dolomite was assumed to have been generated at near-surface conditions, based on cross cutting relationships and crystal size, while Type II dolomite was assumed to be generated during maximum burial, as it postdates stylolitization but presents little other evidence to constrain burial depth.

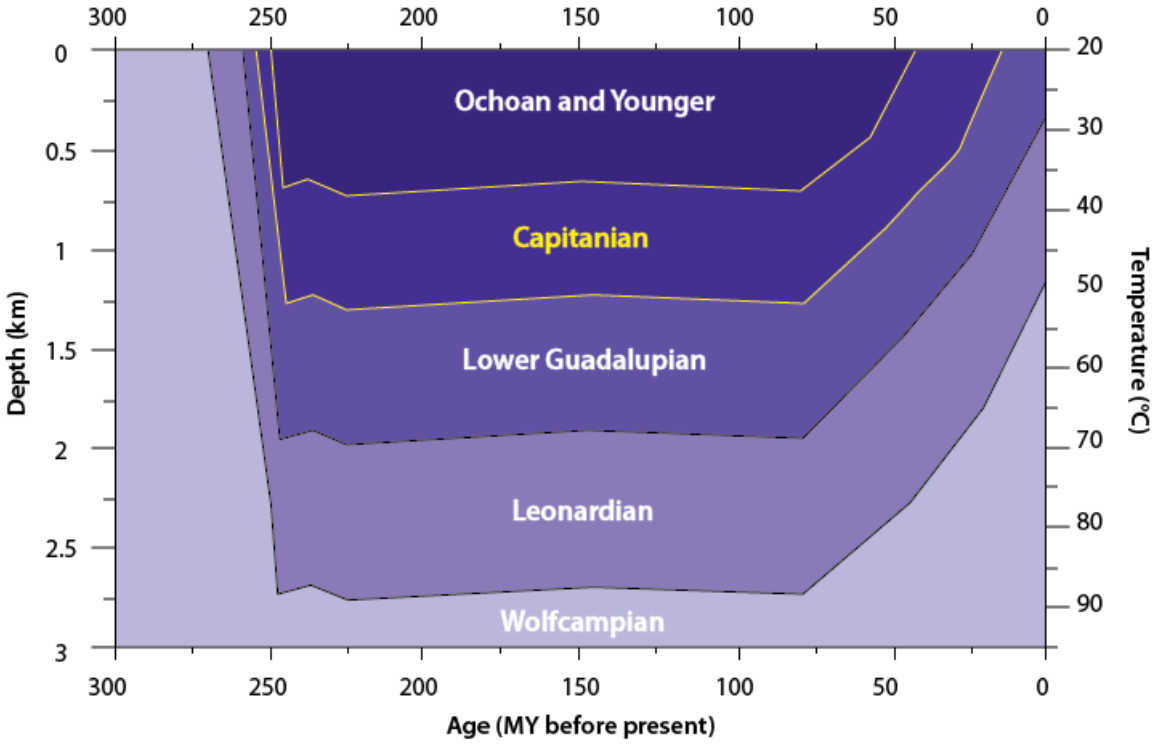

Figure 30: Burial history plot for the Capitan margin, modified from Scholle et al., (1992).

Following these assumptions with the understanding that uncertainty in the fractionation factor may be as great at ±2‰, the ranges for dolomitizing fluid compositions fall from -0.3‰ to +3.7‰ $\delta^{18}O$ with respect to the global marine water standard Vienna Standard Mean Ocean Water (VSMOW) for dolomite Type I, and from -0.3‰ to +6.8‰ $\delta^{18}O$ VSMOW for dolomite Type II (Figure 31). These values are slightly to moderately enriched in comparison to the value for Permian seawater presented by Given and Lohmann (1985), which when converted to $\delta^{18}O$ VSMOW provides a range of 0.0‰ (requiring an elevated fluid temperature of 31°C) to -1.4‰ (at a "standard" surface temperature of 25°C). They also correspond well to the values for dolomite Type I determined by Melim (1991), though she used a much more conservative temperature range of 27 to 31°C.

The enrichment of oxygen in dolomitizing fluids compared to Permian seawater could be the result of evaporative concentration. When marine waters in the middle shelf evaporate, ^{16}O preferentially fractionates into the gaseous phase while ^{18}O remains in the fluid. This has the dual effect of increasing the oxygen isotope ratio of the fluid and its density, providing the hydraulic head necessary to circulate it into the subsurface. If all data points are included for each dolomite type, the same concentrated marine water could be responsible for both episodes of dolomitization provided that there was a ~20°C increase in temperature between dolomitization events, which is not an unrealistic expectation. However, if the two outliers from the dolomite Type II population are removed, the Type II fluid composition ranges shift to the right to a dramatically more ^{18}O enriched composition.

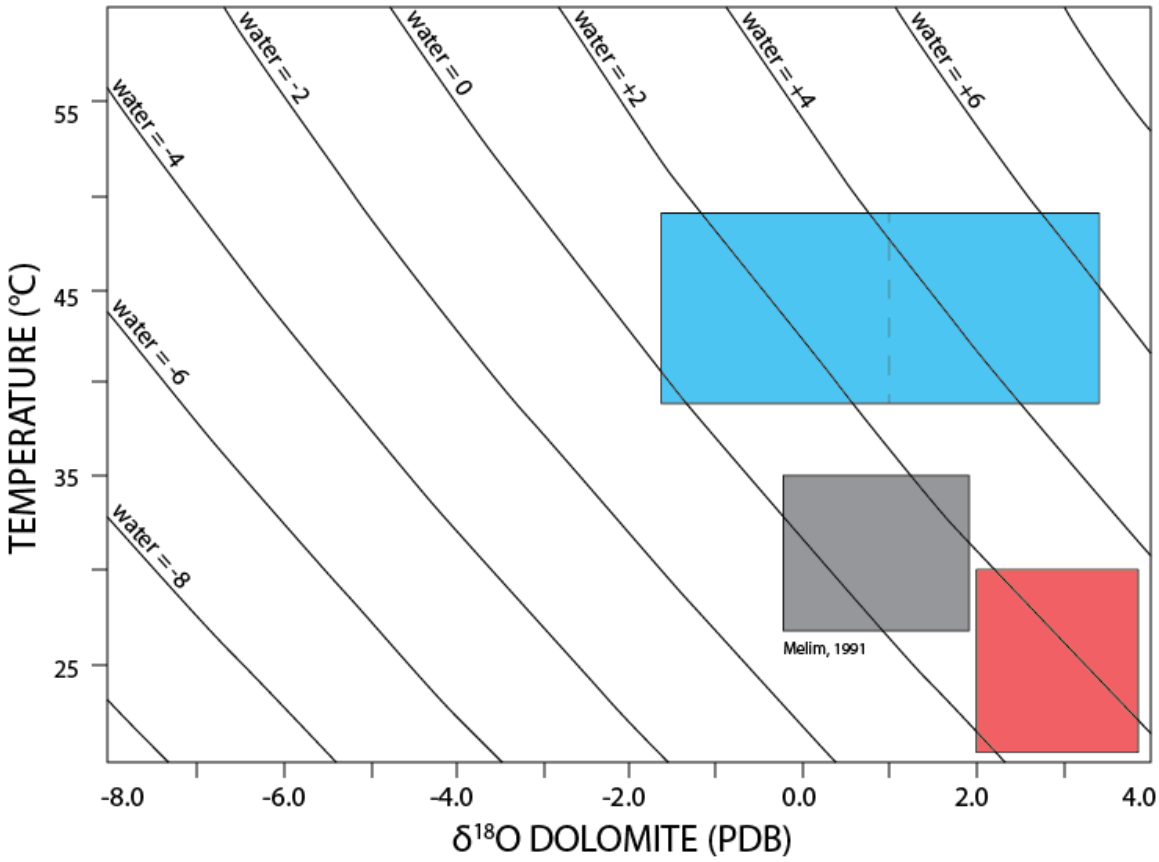

Figure 31: Plot of $\delta^{18}O$ dolomite (VPDB) and fluid temperature (°C), contoured in $\delta^{18}O$ water (VSMOW), with dolomite Type I shaded red, and dolomite Type II shaded blue (box to the right of the dashed line indicates VPDB range for Type II excluding two outliers). Plot generated from the fractionation equation presented above, and modified from Melim (1991), with her dolomite A (equivalent to dolomite Type I) shaded in gray. Temperatures used to generate the dolomite ranges are discussed above, and conversions between the Pee Dee Belemnite standard and the Standard Mean Ocean Water standard were found using the conversion factor $\delta^{18}O_{SMOW} = 1.03086\ \delta^{18}O_{PDB} + 30.86$, derived by Friedman and O'Neil (1977).

CHAPTER 5 – DISCUSSION AND CONCLUSIONS

Having generated quantitative stable isotope and trace element data, as well as making qualitative petrographic and outcrop observations of the timing and distribution of dolomite, two generalized dolomitization models can be proposed for the Cave Graben study window. These models will be described below, and then compared to the previously published models for fault-controlled dolomitization to determine if the behavior, sources, and timing of dolomitizing fluids are the same for strata in different portions of the depositional profile, and in younger Guadalupian strata.

DOLOMITE HYDROLOGIC MODELS

To generate dolomitization models, the combined field observations, petrographic data, and geochemical data for each generation of dolomite will be compared to the expected patterns for marine, reflux, mixing zone, and hydrothermal dolomitization that were presented in Chapter 1, with appropriate modification for inclusion of syndepositional faults and fractures where necessary. Each dolomite generation will be compared to all four dolomitization mechanisms, with the least well supported mechanisms presented first.

Type I Dolomite

Convection of normal marine water is an unlikely mechanism and fluid source for Type I dolomite, based on both the distribution of dolomite and the geochemical trends observed in this study. Type I dolomite is substantially more abundant in the proximal portions of the shelf, while it decreases and even disappears towards the basin. Similarly, authors have observed oxygen isotope enrichment near the inner shelf and depletion towards the basin, which is inconsistent with what a constant flux of normal marine seawater would produce.

Mixing zone dolomitization is also likely incapable of creating the distribution of dolomite observed in the Guadalupe Mountains. The mixing zone would have probably resulted from the combination of a freshwater lens that developed in the shelf crest (Neese, 1989; Parsley and Warren, 1989) and normal marine water circulating in the platform below, however, the zone would be narrow and the chance of it producing pervasive dolomite throughout the upper Capitan is slim. Furthermore, the isotope geochemistry of the dolomite does not support a fluid composition that contains substantial amounts of ^{18}O-depleted meteoric water, but in fact suggests the opposite.

Hydrothermal burial dolomitization directly contradicts cross-cutting relationships and textural/geochemical evidence that suggest early dolomitization. The dolomite crystals are very small, which is consistently recognized for systems with a very high flow rate for diagenetic fluids and low-temperature waters, compared to scalenohedral and relatively coarse dolomites that are considered characteristic of long-lived, high-temperature burial diagenesis. Additionally, the distribution of dolomite is atypical for a basin-sourced burial fluid. Finally, the enriched oxygen isotope ratios of Type I dolomite are contradictory to what one would expect from a high temperature water.

Seepage reflux could easily explain the distribution of dolomite in the Yates Formation, and in fact has been recognized in earlier Guadalupian strata (Garcia-Fresca, 2009), but could be attributed to a variety of brines that may have existed during deposition, as noted by Melim (1991). The Castile and Salado evaporites have both been investigated as a source of brine, but neither presented as the most likely dolomitizing fluid source. The Castile itself contains minimal dolomite, making it an unlikely source for dolomitizing brine (Anderson et al., 1972; Kirkland et al., 2000), and was located entirely in the basin, making it impossible to circulate down through the shelf. On the other hand, the Salado Formation was clearly capable of generating dolomitizing brines,

as it does contain dolomite (Lowenstein, 1988), but circulating these brines deep into the Capitan may have been difficult due to porosity-occluding cementation only slightly below the surface of the top Salado (Casas and Lowenstein, 1989), and requiring deep circulation of Salado fluid contradicts the indicators of shallow dolomitization.

Alternatively, hypersaline brines from the backreef lagoon could easily be responsible for the dolomitization of the Yates Formation, as they were available in abundance and derived from marine fluid with plenty of reactive magnesium. Hypersaline brines are typically associated with evaporite minerals, and evaporites are common in the Guadalupe Mountains penecontemporaneous to or immediately following dolomitization (e.g., evaporite molds within a fine dolomitized matrix). Zones that lack evaporites may be explained by dilution of hypersaline brine towards the platform margin, if it mixed with marine or meteoric water during dolomitization, which would also provide the oxygen isotope depletion observed from shelf to basin. The refluxion of brines matches the distribution of dolomite, which is typically most abundant in the upper shelfal facies and would have been active penecontemporaneously to deposition and deformation, as cross-cutting relationships imply.

Mesosaline brines from directly behind the reef have alsobeen previously attributed to the formation of dolomite in the Guadalupe Mountains based on a lack of observed evaporites in the forereef slope (Melim, 1991; Melim and Scholle, 1989, 2002). However, as noted by the authors, mesosalinity (defined as salinity below the gypsum saturation point, or 35 to 120‰ salinity/112 to 120% enriched compared to seawater) requires a delicate mass balance that must be maintained for as long as dolomitization was occurring. The authors suggest several mechanisms for achieving this steady state of mesosalinity, including undercurrents and storm flooding of the platform, suggesting that it is the simplest model for dolomitization in the Guadalupe Mountains. This study does

not disagree, but finds the complicated requirements for preserving mesosalinity in the lagoon suspect, and lacks fluid inclusion analysis to definitely confirm or deny a mesosaline fluid composition.

Ultimately, evaporatively concentrated lagoonal brines are the most likely fluid source for the first generation of dolomite in the Yates Formation, and probably passed through the shelf by density-driven reflux with minor influence of syndepositional faults and fractures. Both hypersaline and mesosaline brines could account for the enriched oxygen isotope ratios, as they would have each formed from seawater and would have concentrated ^{18}O during drawdown and evaporation. That said, without specific, direct evidence for one salinity condition over the other, this study will decline to speculate.

Type II Dolomite

The hydrologic mechanism responsible for Dolomite Type II has been less heavily scrutinized in previous works, and the most thorough studies, Melim (1991) and Frost et al. (2012), provide contradictory interpretations: the former suggests a modified mixing zone interpretation that occurred during maximum burial, while the latter suggests penecontemporaneous reflux similar to the first generation of dolomite. Data from this study preclude penecontemporaneous dolomitization for the second generation, based on cross-cutting relationships, but could potentially concur with a modified mixing-zone theory. As before, each mechanism will be evaluated in turn.

Both normal marine circulation and hydrothermal dolomitization suffer from the same shortcomings as they do for the first generation. The distribution of Type II dolomite is not consistent with circulation of normal marine fluid; neither are the isotopic ratios and trace element values. But perhaps the most condemning evidence of all is the fact that normal marine water did not exist in the Delaware Basin during Ochoan time.

Basin-derived burial fluids could be responsible, but magnesium content could be a limiting factor. Also basin-derived waters would likely be very hot compared to what petrographic textures actually suggest—even from samples directly adjacent to the fault—and fluid-less thermal recrystallization cannot explain the spatial link between the second generation of dolomite and syndepositional deformation features. Third, Type II dolomite decreases in abundance downward where entire shelf-to-basin depositional profiles are visible, suggesting that the fluids came from above (Melim, 1991).

Melim proposed that a mixture of meteoric and connate waters could explain the slightly depleted signature of Type II dolomite and the distribution of the second generation of dolomite. There were only a few periods of time during burial where meteoric fluids could have entered the system in any great volume, including the Cretaceous and during Tertiary uplift. Crosscutting relationships and the presence of undolomitized meteoric pore filling calcite suggest that earlier meteoric fluids would be more likely responsible for dolomitization. This modified mixing-zone mechanism could be sufficient to generate the second generation of dolomite, but the distribution of such dolomite is in question. Meteoric fluids would have infiltrated from the west, and should be more abundant in that direction, which was not observed in this study. The fluids also would need to me regionally mixed in order to avoid simply forming a narrow zone of dolomite precipitation just like a lens-sourced mixing zone.

Seepage reflux could be a potential mechanism for the second dolomite as well as the first, despite the differences in fluid chemistry discussed above. However, as the second dolomite formed during burial, a backreef lagoonal brine is no longer a viable source of dolomitizing fluid. Instead, the sources of refluxing brines would have only been the Castile and Salado Formations. As before, the Castile produced minimal intra-formation dolomite and was confined to the basin, so it is not likely to be the source of

dolomite II any more than it is the source of dolomite I. But, the distinct fault and fracture control on dolomite Type II may eliminate the issues presented for Salado refluxion, namely early cementation and lack of downward permeability pathways. Syndepositional deformation features were active and at least partly permeable all the way from deposition, through burial and into Tertiary uplift, and if they propagated all the way up to the overlying Salado Formation, brines could have easily circulated down into the underlying platform. The presence of small, discontinuous lateral "fingers" of dolomite Type II extending away from vertical deformation features supports a vertical migration of fluids as well—any lateral migration should be reflected as bed-bound dolomite in the field, which was not observed.

Geochemical evidence could support a Salado-sourced brine as the dolomitizing fluid. Salado evaporites came from a brine concentrated enough to precipitate halite and potash, which implies intense evaporation and resulted in an ^{18}O enriched fluid (Castile calcite laminations plot at +5‰ $\delta^{18}O$ VPDB (Magaritz et al., 1983), and the Salado fluids were even more concentrated). Because oxygen isotopes in rock are usually water-buffered, it is intuitive to assume that the resulting dolomite would also be heavy compared to the first generation. But intuition may be misleading; the dolomite oxygen isotope ratios are slightly depleted relative to the first generation of dolomite despite the fact that corresponding oxygen isotope ratios of the fluid may have actually been enriched relative to those of the first generation (Figure 31). Depletion relative to VPDB in the crystals could simply due to the elevated temperature of the fluid. Care must be taken to consider the potential error associated with the dolomite fractionation equation when estimating a fluid composition; however, in combination with field and petrographic evidence, the interpretation of a Salado-source brine is reasonable.

Based on both the enrichment of the second dolomitizing fluid and the spatial relationship to syndepositional faults and fractures, it appears more reasonable to assume that downward passage of Salado evaporative brine through the deformation features is the most likely mechanism for the formation of Type II dolomite. Were there to be an influx of meteoric fluid from the west, as suggested in Melim's mixing hypothesis, one might expect a decrease in dolomite basinward, or a possible oxygen isotope enrichment basinward as connate waters became more dominant. In this study, neither was observed.

CONCLUSION

The interpretation of concentrated seawater as the main dolomitizing fluid for the first generation of dolomite is consistent with fluid source interpretations across the Guadalupe Mountains (Frost et al., 2012; Melim, 1991; Melim and Scholle, 2002; Mutti and Simo, 1993; Mutti and Simo, 1994; Parsley and Warren, 1989), though questions as to the concentration of fluid salinity exist, based on the observation of evaporites. In combination with field geometries of dolomite bodies, and the distribution of dolomite on the outcrop it is also likely that seepage reflux of the brines was the main mechanism for transporting diagenetic fluid, with minor enhancement where syndepositional deformation features provided a more permeable conduit.

The precipitation of the second generation of dolomite from Salado evaporative brines does not correspond to previously-published studies of dolomitization, perhaps because these studies have encountered this dolomite in much smaller abundances and have assumed that they follow the same permeability paths as the first generation (Melim, 1991). The increased volume of the second generation of dolomite in this study provides a clearer picture of the interaction between dolomitizing fluid II and permeability conduits in the platform margin. This study suggests that, not only is Type II dolomite

common, but that was likely sourced from a highly enriched, warm fluid during burial, and mostly migrated vertically, with only a minor lateral component.

The key difference between the results of this study and the results of previous dolomitization work is the spatial distribution of dolomites in and around the Cave Graben fault system. Previous works have identified the relationship between syndepositional deformation features and dolomite halos, but few have recognized the true extent of the impact these features can have on the porosity and permeability conditions of the platform margin through time. Clastic-filled fractures, faults, primary reef cavities and sand beds were especially permeable, and allowed for extensive dolomitization of both the reefal and shelfal facies updip of and within the Cave Graben at a scale which has largely been undocumented elsewhere in the Guadalupe Mountains. Comparatively, marine cemented faults and fractures were less permeable and prevented the transport of dolomitizing fluids into the formation, as is demonstrated by their abundance in the reefal facies downdip of the Cave Graben and a corresponding absence of large volumes of dolomite.

The second generation of dolomite occurs almost solely around syndepositional deformation features, and demonstrates that the permeability conditions of the surrounding strata changed during burial while the increased permeability of the faults and fractures did not. Where the first generation of dolomite is pervasive through the shelf crest strata well away from syndepositional faults and fractures and suggests dominantly bed-parallel flow, only meter-scale haloes of the second dolomite exist in the shelf crest around syndepositional faults and fractures. This suggests that syndepositional deformation features exerted a main control on dolomite fluid flow once they were open and during reactivation, where the original depositional fabrics that were not around a

syndepositional fault or fracture have no opportunity to change once they became cemented to a prohibitive level for fluid flow.

Data presented here are interpreted to show that syndepositional deformation features can exert a primary influence on the distribution of diagenetic products, and dramatically influence the vertical (and to an indirect extent, the horizontal) porosity and permeability of the shelf margin over time. Additionally, the combination of Melim's study, this study, and Frost and others' study suggest that syndepositional fault control on the distribution of late dolomite occurs in a wide variety of Permian strata at a significant volume (perhaps up to 50%, as this study suggests), which is a dolomitization pattern that is not typically considered in outcrop studies—especially where the earliest dolomite is present, and recognizing later overprinting in the outcrop may be difficult without thin sections. As such, ignoring the effect of syndepositional faulting and fracturing on long-term diagenetic and porosity and permeability trends could result in a serious misunderstanding of the controls on diagenetic phase distribution both in outcrop, and in analogous subsurface reservoirs.

APPENDIX A – FRACTURE DATA

Syndepositional Fracture Data					
Fracture ID	**Orientation (trend)**	**Aperture (cm)**	**Fill Type**	**HFS**	**Facies**
RS1A	79	2	Silt	G24	R
RS1B	84	5	Silt	G24	R
RS2A	83	13	Wckstn	G25	R
RS3A	Cavity	60	Skeletal	G25	R
RS2B	65	54	Wckstn	G25	OS
RS2C	68	100	Silt/Wckstn	G25	OS
RS2D	75	50	Silt/Wckstn	G25	OS
RS2E	76	42	Silt/Wckstn	G25	OS
RS4A	61	30	Wckstn	G25	OS
RS5A	65	37	Wckstn	G25	OS
RS5B	69	37	Wckstn/Marine Cement	G25	OS
RS6A	Horizontal	19	Wckstn	G25	FS
RS6B	71	7	Wckstn	G25	FS
RS6C	85	30	Wckstn	G25	FS
RS6D	78	14	Wckstn	G25	SC
RS7A	Horizontal	10	Wckstn	G25	SC
RS8A	Horizontal	10	Wckstn	G25	SC
RS9A	61	28	Wckstn	G26	SC
RS10A	Horizontal	7	Marine Cement	G26	SC
RS11A	Horizontal	6	Wckstn	G26	SC
RS12A	Horizontal	7	Wckstn	G26	SC
RS13A	75	13	Sand	G27	SC
RS14A	Horizontal	25	Marine Cement	G27	SC
RS15A	72	6	Marine Cement	G27	R
RS16A	71	2	Marine Cement	G27	R
RS17A	Horizontal	3	Sand	G27	R
RS18A	Horizontal	3	Marine Cement	G27	R
RS19A	84	6	Sand	G27	R
RS19B	87	1	Sand	G27	R
RS20A	80	1	Sand	G27	R
RS21A	62	5	Sand	G27	R
RS22A	66	2	Sand	G27	R
RS23A	64	3	Marine Cement	G27	
RS24A	76	3	Marine Cement	G27	

RS25A	68	35	Sand	G27	
RS26A	71	38	Sand	G27	
RS27A	72	17	Marine Cement	G27	
RS28A	81	12	Sand	G27	
RS29A	65	6	Wckstn	G25	SC
RS30A	Horizontal	5	Wckstn	G25	SC
RS31A	Horizontal	5	Wckstn	G25	SC
RS32A	Horizontal	3	Wckstn	G25	SC
RS33A	Horizontal	3	Wckstn	G25	SC
RS34A	Horizontal	4	Wckstn	G25	SC
RS33B	Horizontal	7	Wckstn/Marine Cement	G25	SC
RS33C	Horizontal	10	Wckstn/Marine Cement	G25	SC
RS35A	Horizontal	30	Wckstn	G25	FS
RS36A	Horizontal	2	Wckstn	G25	OS
RS37A	38	2	Wckstn	G25	OS
RS38A	Horizontal	4	Wckstn	G25	OS
RS39A	Cavity	50	Wckstn/Silt	G25	OS
RS40A	69	7	Marine Cement	G25	OS
RS41A	72	8	Silt	G25	OS
RS42A	84	8	Marine Cement	G24	R
RS43A	78	3	Wckstn/Skeletal	G24	R
RS44A	64	11	Wckstn/Silt	G24	R
RS45A	59	8	Silt	G24	R
RS46A	82	7	Silt	G24	R
RS47A	Horizontal	10	Wckstn	G27	SC
RS47B	Horizontal	10	Wckstn	G27	SC
RS47C	Horizontal	7	Wckstn	G27	SC
RS47D	Horizontal	11	Wckstn	G27	SC
RS47E	Horizontal	12	Wckstn	G27	SC
RS47F	Horizontal	13	Wckstn	G26	SC
RS48A	Horizontal	6	Wckstn	G26	SC
RS49A	76	38	Sand	G26	SC
RS50A	Horizontal	6	Wckstn	G26	SC
RS51A	68	8	Wckstn	G26	SC
RS52A	Horizontal	3	Wckstn	G25	SC
RS52B	Horizontal	3	Wckstn	G25	SC
RS53A	Horizontal	3	Wckstn	G25	SC
RS53B	Horizontal	8	Wckstn	G25	SC

RS54A	Horizontal	11	Wckstn	G25	SC
RS54B	Horizontal	24	Wckstn	G25	SC
RS54C	Horizontal	20	Wckstn	G25	SC
RS55A	69	10	Wckstn	G25	SC
RS55B	Horizontal	7	Wckstn	G25	SC
RS56A	Horizontal	7	Wckstn	G25	SC
RS57A	Horizontal	4	Wckstn	G25	SC
RS58A	Horizontal	10	Wckstn	G25	SC
RS59A	Horizontal	5	Wckstn	G25	SC
RS60A	Horizontal	10	Wckstn	G26	SC
RS61A	Horizontal	9	Wckstn	G26	SC
RS62A	Horizontal	20	Wckstn	G27	SC
RS63A	Horizontal	7	Wckstn	G27	SC
RS64A	48	6	Wckstn/Marine Cement	G27	SC
RS65A	63	11	Wckstn	G27	SC
RS66A	Horizontal	3	Wckstn	G25	SC
RS67A	47	10	Marine Cement	G25	SC
RS68A	68	5	Marine Cement	G25	SC
RS69A	70	6	Wckstn/Marine Cement	G25	SC
RS70A	64	3	Marine Cement	G25	OS
RS71A	71	3	Marine Cement	G25	OS
RS72A	74	15	Marine Cement	G25	OS
RS73A	70	6	Wckstn	G25	SC
RS74A	Horizontal	5	Wckstn/Marine Cement	G25	SC
RS75A	72	1	Wckstn/Marine Cement	G25	SC
RS76A	71	3	Marine Cement	G25	SC
RS77A	66	13	Wckstn	G25	FS
RS77B	75	33	Wckstn	G25	FS
RS77C	66	4	Wckstn	G25	OS
RS78A	78	13	Wckstn	G25	FS
RS79A	Horizontal	12	Wckstn	G25	SC
RS80A	Horizontal	3	Wckstn	G25	SC
RS81A	76	37	Wckstn/Sand	G25	SC
RS81B	75	46	Wckstn/Sand	G25	SC
RS82A	63	25	Wckstn/Sand	G25	SC
RS83A	78	9	Wckstn	G25	FS
RS84A	84	27	Wckstn/Sand	G25	FS
RS85A	Horizontal	7	Wckstn	G25	FS

RS86A	81	13	Wckstn	G25	FS
RS87A	70	8	Wckstn	G25	SC
RS88A	69	8	Wckstn	G25	SC
RS89A	67	40	Wckstn/Sand	G25	SC
RS90A	71	45	Wckstn	G25	SC
RS91A	70	35	Wckstn	G25	SC
RS92A	Horizontal	10	Wckstn	G25	SC
RS93A	72	3	Wckstn	G25	SC
RS94A	Horizontal	7	Wckstn	G25	SC
RS95A	60	10	Wckstn	G25	SC
RS96A	69	9	Wckstn	G25	SC
RS97A	61	48	Wckstn	G25	OS
RS97B	60	37	Wckstn	G25	G25
RS97C	61	21	Wckstn	G25	OS
RS97D	61	10	Wckstn	G25	OS
RS97E	64	10	Wckstn	G25	OS
RS98A	73	Cavity	Silt	G25	R
RS99A	Cavity	Cavity	Silt	G25	R
RS100A	78	9	Wckstn	G25	R
RS101A	71	1	Marine Cement	G25	R
RS102A	79	10	Wckstn	G25	R
RS103A	Horizontal	13	Silt	G25	R
RS104A	78	1	Marine Cement	G25	R
RS105A	176	2	Marine Cement	G25	R
RS106A	170	6	Silt	G25	OS
RS107A	100	1	Silt	G25	OS
RS108A	64	4	Marine Cement	G25	OS
RS108B	53	3	Marine Cement	G25	OS
RS109A	62	4	Marine Cement	G25	OS
RS110A	61	6	Marine Cement	G25	OS
RS111A	Horizontal	10	Marine Cement	G25	FS
RS112A	Horizontal	5	Marine Cement	G25	SC
RS113A	65	12	Silt	G24	R
RS113B	68	7	Silt	G24	R
RS114A	74	3	Marine Cement	G24	R
RS115A	81	1	Marine Cement	G24	R
RS116A	78	4	Silt	G24	R
RS117A	69	6	Silt	G24	R

RS118A	66	7	Marine Cement	G24	R
RS119A	66	7	Silt	G24	R
RS120A	62	12	Silt	G24	R
RS120B	63	16	Silt	G24	R

All syndepositional fracture data. The alphabetic modifier at the end of each fracture name reflects whether or not the data point represents a unique fracture, or a splay from a previously identified fracture. Individual fractures are classified as RS#A, while fractures with splays are first classified as RS#A, then each splay is sequentially classified using RS#B, C, D, as necessary. Syndepositional fracture data was collected using a Brunton compass; because most fractures had variable dip, all trends are reported using the lower of the two potential azimuths. Facies included are reef (R), outer shelf (O), foreshore (F), shelf crest (SC).

APPENDIX B – STABLE ISOTOPE VALUES

Carbon and Oxygen Isotope Ratios for All Analyzed Dolomite, Calcite Samples						
Sample Name	**$d^{13}C$-VPDB**	**$d^{18}O$-VPDB**	**Field Sample ID**	**Facies**	**Dol Type - Texture**	**Dol Type-CL**
Permian SW	**5.20**	**-2.80**				
RES-19	6.70	2.69	SB6	O	1	1
RES-20	6.40	3.87	SB7	O	2	1
RES-21	6.32	2.40	SB8	F	2	1
RES-30	6.80	3.38	SB18	SC	1	1
RES-31	6.82	2.98	SC1	SC	1	1
RES-32	6.79	3.24	SC2	SC	1	1
RES-33	6.94	2.83	SC3	SC	M	1
RES-36	6.73	3.31	SC7	F	M	1
RES-37	6.32	2.80	SC8	O	2	1
RES-39	6.95	2.46	SC11	F	1	1
RES-48	6.54	3.01	SD4-1	R	1	1
RES-54	6.93	2.61	SD11	SC	M	1
RES-55	6.79	2.32	SD12	SC	2	1
RES-56	7.13	2.66	SD13	SC	M	1
RES-59	7.21	2.83	SD16	SC	1	1
RES-62	7.10	2.04	SHC3-1	SC	1	1
RES-02	5.99	2.18	SA2	R	M	2
RES-04	3.36	-1.54	SA5	R	2	2
RES-05	5.81	2.45	SA6	R	2	2
RES-07	6.80	3.07	SA9	R	2	2
RES-08	7.05	3.56	SA10	R	2	2
RES-08-DUP	6.71	2.35	SA10	R	2	2
RES-09	6.54	1.47	SA11	R	2	2
RES-10	6.11	2.99	SA12	R	M	2
RES-11	5.67	2.51	SA13	R	2	2
RES-12	6.00	-0.75	SA18	R	2	2
RES-13	6.77	1.13	SA20	R	2	2
RES-14	6.81	3.52	SB1	R	M	2
RES-16	6.80	2.74	SB3	O	2	2
RES-17	5.54	1.66	SB4	O	2	2
RES-34	6.31	1.17	SC4	O	2	2
RES-40	5.92	2.11	SC12	F	2	2
RES-41	5.78	1.70	SC13	F	2	2

RES-42	6.48	2.13	SC14	O	2	2
RES-46	6.60	2.04	SD2	R	2	2
RES-49	5.54	2.12	SD5	O	2	2
RES-50	6.23	1.70	SD7	O	2	2
RES-51	6.17	1.80	SD8	O	2	2
RES-61	6.49	1.54	SHC2	SC	2	2
RES-63	6.01	2.20	SHC3-2	SC	2	2
RES-64	6.72	1.72	SHC4	SC	M	2
RES-65	7.28	1.32	SHC6	SC	M	2
RES-66	7.13	1.85	SHC7	SC	2	2
RES-67	7.11	2.03	SHC8	SC	2	2
RES-15	3.62	-4.01	SB2	O	C	C
RES-18	3.03	-4.15	SB5	F	C	C
RES-24	5.82	-0.95	SB12	O	C	C
RES-01	6.47	3.06	SA1	R	1	M
RES-06	6.68	3.43	SA7	R	1	M
RES-28	7.21	2.61	SB16	SC	M	M
RES-28-DUP	7.23	1.65	SB16	SC	M	M
RES-29	6.67	2.70	SB17	SC	M	M
RES-38	6.35	1.60	SC9	O	M	M
RES-43	5.98	2.60	SC15	R	M	M
RES-44	6.96	2.48	SC18	O	M	M
RES-47	6.63	2.57	SD3	R	M	M
RES-52	6.32	2.03	SD9	O	2	M
RES-53	6.66	2.57	SD10	F	2	M
RES-57	7.04	3.05	SD14	F	M	M
RES-57-DUP	6.74	2.31	SD14	F	M	M
RES-58	6.80	2.42	SD15	SC	M	M
RES-22	6.06	-0.01	SB9			
RES-23	6.74	2.21	SB10			
RES-25	6.84	0.68	SB13			
RES-26	5.49	-1.91	SB14			
RES-35	5.09	-3.38	SC6			
RES-60	6.37	-0.46	SHC1			

All carbon and oxygen stable isotopic analyses. Samples highlighted in yellow were excluded from analysis due to insufficient sample size and low voltage. Samples with a hyphenated field sample ID indicate samples that had both Type I and Type II dolomite in the same sample; the number following the hyphen indicates which generation was sampled. Facies included are reef (R), outer shelf (O), foreshore (F), shelf crest (SC). "Dol Type – Texture' is a classification based on visual inspection of the degree of recrystallization/fabric destruction in a sample. 'Dol Type – CL" is a classification based on the intensity and color of luminescence, and was used for the analysis as it proved to be a more reliable indicator. Dolomite types include Type I (1), Type II (2), dolomite that has contradictory characteristics or variable recrystallization, "Mixed Dol" in the text (M), and calcite (C), which is a mix of stabilized low-Mg calcite and late pore filling calcite in unknown proportions. Permian seawater value from Given and Lohmann (1985).

BIBLIOGRAPHY

Aby, S. B., 1994, Relation of bank-margin fractures to sea-level change, Exuma Islands, Bahamas: Geology, v. 22, p. 1063-1066.

Adams, J. E., and M. L. Rhodes, 1960, Dolomitization by Seepage Refluxion: AAPG Bulletin, v. 44, p. 1912-1920.

Anderson, R. Y., W. E. Dean, Jr, D. W. Kirkland, and H. I. Snider, 1972, Permian Castile Varved Evaporite Sequence, West Texas and New Mexico: GSA Bulletin, v. 83, p. 59-86.

Assereto, R. L., and C. G. S. C. Kendall, 1977, Nature, origin, and classification of peritidal tepee structures and related breccias: Sedimentology, v. 24, p. 153-210.

Badiozamani, K., 1973, The Dorag Dolomitization Model - Application to the Middle Ordovician of Wisconsin: Journal of Sedimentary Petrology, v. 43, p. 965-984.

Baker, P. A., and S. J. Burns, 1985, Occurence and Formation of Dolomite in Organic-Rich Continental Margin Sediments: AAPG Bulletin, v. 69, p. 1917-1930.

Banner, J. L., 1986, Petrographic and Geochemical Constraints on the Origin of Regionally Extensive Dolomites of the Mississippian Burlington and Keokuk Formations, Iowa, Illinois, and Missouri, State University of New York, Stony Brook, New York, 382 p.

Banner, J. L., and G. N. Hanson, 1990, Calculation of simultaneous isotopic and trace element variations during water-rock interaction with appllications to carbonate diagenesis: Geochimica et Cosmochimica Acta, v. 54, p. 3123-3137.

Barber, C., 1974, Major and Trace Element Associations in Limestones and Dolomites: Chemical Geology, v. 14, p. 273-280.

Bishop, J. W., D. A. Osleger, I. P. Montanez, and D. Y. Sumner, 2014, Meteoric diagenesis and fluid-rock interaction in the Middle Permian Capitan backreef: Yates Formation, Slaughter Canyon, New Mexico: AAPG Bulletin, v. 98, p. 1495-1519.

Borer, J. M., and P. M. Harris, 1989, Depositional Facies and Cycles in Yates Formation Outcrops, Guadalupe Mountains, New Mexico, Subsurface and Outcrop Examination of the Capitan Shelf Margin, Northern Delaware Basin, p. 13.

Borer, J. M., and P. M. Harris, 1991, Lithofacies and Cyclicity of the Yates Formation, Permian Basin: Implications for Reservoir Heterogeneity: AAPG Bulletin, v. 75, p. 726-779.

Budd, D. A., E. L. Frost, III, K. W. Huntington, and P. F. Allwardt, 2013, Syndepositional deformation features in high-relief carbonate platforms: long-lived conduits for diagenetic fluids Journal of Sedimentary Research, v. 82, p. 12-36.

Burns, S. J., and P. A. Baker, 1987, A Geochemical Study of Dolomite in the Monterey Formation, California: Journal of Sedimentary Petrology, v. 57, p. 128-139.

Carballo, J. D., L. S. Land, and D. E. Miser, 1987, Holocene Dolomitization of Supratidal Sediments by Active Tidal Pumping, Sugarloaf Key, Florida: Journal of Sedimentary Petrology, v. 57, p. 153-165.

Carpenter, D. G., S. A. Guidry, J. D. Degraff, and J. Collins, 2006, Evolution of Tengiz Rim/Flank Reservoir Quality: New Insights from Systematic, Integrated Core Fracture and Diagenesis Investigations.

Casas, E., and T. K. Lowenstein, 1989, Diagenesis of Saline Pan Halite: Comparison of Petrographic Features of Modern, Quaternary, and Permian Halites: Journal of Sedimentary Petrology, v. 59, p. 724-739.

Choquette, P. W., and R. P. Steinen, 1980, Mississippian Non-Supratidal Dolomite, Ste. Genevieve Limestone, Illinois Basin: Evidence for Mixed Water Dolomitization, *in* D. H. Zenger, J. B. Dunham, and R. L. Ethington, eds., Concepts and Models of Dolomitization: SEPM Special Publications, Society of Economic Paleontologists and Mineralogists, p. 163-196.

Cozzi, A., 2000, Synsedimentary tensional features in Upper Triassic shallow-water platform carbonates of the Carnian Prealps (northern Italy) and their importance as paleostress indicators: Basin Research, v. 12, p. 133-146.

Craig, H., 1957, Isotopic standards for carbon and oxygen and correction factors for mass-spectrometric analysis of carbon dioxide: Geochimica et Cosmochimica Acta, v. 12, p. 133-149.

Daugherty, D. R., 1986, Characteristics and origins of joints and sedimentary dikes of the Bahama Islands, Miami University, Department of Geology.

Della Porta, G., J. A. M. Kenter, and J. R. Bahamonde, 2004, Depositional facies and stratal geometry of an Upper Carboniferous prograding and aggrading high-relief carbonate platform (Cantabrian Mountains, N Spain): Sedimentology, v. 51, p. 267-295.

Dunham, R. J., 1972, Capitan Reef, New Mexico and Texas: Facts and questions to aid interpretation and group discussion, Society for Economic Paleontologists and Mineralogists (SEPM), Permian Basin Section.

Esteban, M., and L. C. Pray, 1977, Upper Guadalupian facies, Permian Reef Complex, Guadalupe Mountains, New Mexico and west Texas: SEPM Field Conference Guidebook, v. 2, Society for Economic Paleontologists and Mineralogists.

Folk, R. L., and L. S. Land, 1975, Mg/Ca Ratio and Salinity: Two Controls over Crystallization of Dolomite: AAPG Bulletin, v. 59, p. 60-68.

Friedman, I., and J. R. O'Neil, 1977, Compilation of stable isotope fractionation factors of geochemical interest, *in* M. Fleischer, ed., Data of Geochemistry, United States Geological Survey.

Frost, E. L., III, 2007, Facies heterogeneity, platform architecture and fracture patterns of the Devonian reef complexes, Canning Basin, Western Australia, University of Texas at Austin, 172 p.

Frost, E. L., III, D. A. Budd, and C. Kerans, 2012, Syndepositional deformation in a high-relief carbonate platform and its effect on early fluid flow as revealed by dolomite patterns: Journal of Sedimentary Research, v. 82.

Frost, E. L., III, and C. Kerans, 2009, Platform margin trajectory as a control on syndepositional fracture patterns, Canning Basin, Western Australia Journal of Sedimentary Research, v. 79, p. 44-55.

Frost, E. L., III, and C. Kerans, 2010, Controls on syndepositional fracture patterns, Devonian reef complexes, Canning Basin, Western Australia: Journal of Structural Geology, v. 32, p. 1231-1249.

Garber, R. A., G. A. Grover, and P. M. Harris, 1989, Geology of the Capitan Shelf Margin - Subsurface Data from the Northern Delaware Basin, *in* P. M. Harris, and G. A. Grover, eds., Subsurface and Outcrop Examination of the Capitan Shelf Margin, Northern Delaware Basin: SEMP Core Workshop: San Antonio, Society for Economic Paleontologists and Mineralogists, p. 3-270.

Garcia-Fresca, B., 2009, Outcrop-constrained Flow and Transport Models of Reflux Dolomitization, University of Texas at Austin, 199 p.

George, A. D., N. Chow, and K. M. Trinajstic, 2009, Syndepositional fault control on lower Frasnian platform evolution, Lennard Shelf, Canning Basin, Australia: Geology, v. 37, p. 331-334.

Gisquet, F., J. Lamarche, M. Floquet, J. Borgomano, M. Jean-Pierre, and B. Caline, 2013, Three-dimensional structural model of composite dolomite bodies in folded area (Upper Jurassic of the Etoile massif, southeastern France): AAPG Bulletin, v. 97, p. 1477-1501.

Given, R. K., and K. C. Lohmann, 1985, Derivation of the Original Isotopic Composition of Permian Marine Cements: Journal of Sedimentary Petrology, v. 55, p. 430-439.

Given, R. K., and K. C. Lohmann, 1986, Isotopic evidence for the early meteoric diagenesis of the reef facies, Permian reef complex of west Texas and New Mexico: Journal of Sedimentary Petrology, v. 56, p. 183-193.

Guidry, S. A., M. Grasmueck, D. G. Carpenter, A. M. Gombos, Jr., S. L. Bachtel, and D. A. Viggiano, 2007, Karst and early fracture networks in carbonates, Turks and Caicos Islands, British West Indies: Journal of Sedimentary Research, v. 77, p. 508-524.

Hanshaw, B. B., W. Back, and R. G. Deike, 1971, A geochemical hypothesis for dolomitization by groundwater: Economic Geology, v. 66, p. 710-724.

Hardie, L. A., 1987, Dolomitization: A Critical View of some Current Views: PERSEPCTIVES: Journal of Sedimentary Petrology, v. 57, p. 166-183.

Harman, C. A., 2011, Quantified Facies Distribution and Sequence Geometry of the Yates Formation, Slaughter Canyon, New Mexico, University of Texas at Austin, 157 p.

Hill, C. A., 1996, Geology of the Delaware Basin Guadalupe, Apache and Glass Mountains, New Mexico and West Texas, Society for Economic Paleontologists and Mineralogists (SEPM), Permian Basin Section, 480 p.

Hill, C. A., 1999, Origin of Caves in the Capitan, *in* A. H. Saller, P. M. Harris, B. L. Kirkland, and S. J. Mazzullo, eds., Geologic Framework of the Capitan Reef: SEPM Special Publication: Tulsa, Society for Economic Paleontologists and Mineralogists, p. 211-222.

Humphrey, J. D., 1988, Late Pleistocene mixing zone dolomitization, southeastern Barbados, West Indies: Sedimentology, v. 35, p. 327-348.

Hunt, D. W., W. M. Fitchen, and E. Koša, 2002, Syndepositional deformation of the Permian Capitan reef carbonate platform, Guadalupe Mountains, New Mexico, USA: Sedimentary Geology, v. 154, p. 89-126.

Illing, L. V., 1959, Deposition and Diagenesis of Some Upper Paleozoic Carbonate Sediments in Western Canada, 5th World Petroleum Congress, New York, p. 30.

Jones, N. B., 2012, Integrated Lidar and Outcrop Study of Syndepositional Faults and Fractures in the Capitan Formation, Guadalupe Mountains, New Mexico, USA, University of Texas at Austin, 172 p.

Kerans, C., and K. Kempter, 2002, Heirarchical Stratigraphic Analysis of a Carbonate Platform, Permian of the Guadalupe Mountains, *in* T. U. o. T. a. A. Bureau of Economic Geology, ed.: Datapages Discovery Series, American Association of Petroleum Geologists.

Kerans, C., and S. W. Tinker, 1999, Extrinsic Stratigraphic Controls on Development of the Capitan Reef Complex, Geological Framework of the Capitan Reef: SEPM Special Publications, Society of Economic Paleontologists and Mineralogists (SEPM), p. 15-36.

Kerans, C., C. Zahm, S. Hiebert, A. Parker, and N. B. Jones, 2012, Advances in the Integrated Stratigraphic and Structural Model of the Guadalupian Mixed Clastic-Carbonate Strata, Guadalupe Mountains: RCRL Annual Meeting Field Trip Guidebook, Bureau of Economic Geology, The University of Texas at Austin, 111 p.

King, P. B., 1942, Permian of West Texas and southeastern New Mexico: AAPG Bulletin, v. 26, p. 535-763.

King, P. B., 1948, Geology of the southern Guadalupe Mountains, Texas, US Government Printing Office.

Kirkland, D. W., R. E. Denison, and W. E. Dean, Jr, 2000, Parent Brine of the Castile Evaporites (Upper Permian), Texas and New Mexico: Journal of Sedimentary Research, v. 70, p. 749-761.

Kohout, F. A., 1967, Ground-water Flow and the Geothermal Regine of the Floridian Plateau: Gulf Coast Association of Geological Societies Transactions, v. 17, p. 339-354.

Kohout, F. A., H. R. Henry, and J. E. Banks, 1977, Hydrogeology related to geothermal conditions of the Floridian Plateau, Florida Bureau of Geology Special Publication.

Koša, E., and D. W. Hunt, 2005, Growth of syndepositional faults in carbonate strata: Upper Permian Capitan platform, New Mexico, USA: Journal of Structural Geology, v. 27, p. 1069-1094.

Koša, E., and D. W. Hunt, 2006a, Heterogeneity in fill and properties of karst-modified syndepositional faults and fractures: Upper Permian Capitan platform, New Mexico, USA: Journal of Sedimentary Research, v. 76, p. 131-151.

Koša, E., and D. W. Hunt, 2006b, The effect of syndepositional deformation within the Upper Permian Capitan Platform on the speleogenesis and geomorphology of the Guadalupe Mountains, New Mexico, USA: Geomorphology, v. 78, p. 279-308.

Koša, E., D. W. Hunt, W. M. Fitchen, M.-O. Bockel-Rebelle, and G. Roberts, 2003, The Heterogeneity of paleocavern systems developed along syndepositional fault zones: the Upper Permian Capitan Platform, Guadalupe Mountains, USA, Permo-Carboniferous Carbonate Platforms and Reefs, v. 83, AAPG, p. 291-322.

Koša, E., D. W. Hunt, G. Roberts, W. M. Fitchen, and M.-O. Bockel-Rebelle, 2000, Temporal and Spatial Variability in the Fill and Diagenesis of Syndepositional Fault Zones, Permian Capitan Reef Platform, Slaughter Canyon, Guadalupe Mountains, New Mexico: Implications for Platform Development, Diagenesis and Connectivity of Yates Reservoirs.: AAPG/EAGE International Research Conference.

Kurz, T. H., J. Dewit, S. J. Buckley, J. B. Thurmond, D. W. Hunt, and R. Swennen, 2012, Hyperspectral image analysis of different carbonate lithologies (limestone, karst and hydrothermal dolomites): the Pozalagua Quarry case study (Cantabria, North-west Spain): Sedimentology, v. 59, p. 632-645.

Land, L. S., 1973a, Contemporaneous Dolomitization of Middle Pleistocene Reefs by Meteoric Water, North Jamaica: Bulletin of Marine Science, v. 23, p. 64-92.

Land, L. S., 1973b, Holocene meteoric dolomitization of Pleistocene limestones, North Jamaica: Sedimentology, v. 20, p. 411-424.

Land, L. S., 1980, The isotopic and trace element geochemistry of dolomite: The state of the art, *in* D. H. Zenger, J. B. Dunham, and R. L. Ethington, eds., Concepts and Models of Dolomitization: SEPM Special Publications: Tulsa, Society for Economic Paleontologists and Mineralogists, p. 87-110.

Land, L. S., 1983, The application of stable isotopes to studies of the origin of dolomite and to problems of diagenesis of clastic sediments, Stable Isotopes in Sedimentary Geology, SEPM.

Land, L. S., 1985, The origin of massive dolomite: Journal of Geologic Education, v. 33, p. 112-125.

Lowenstein, T. K., 1988, Origin of depositional cycles in a Permian "saline giant": The Salado (McNutt Zone) evaporites of New Mexico and Texas: GSA Bulletin, v. 100, p. 592-608.

Luczaj, J. A., 2006, Evidence against the Dorag (mixing-zone) model for dolomitization along the Wisconsin arch - A case for hydrothermal diagenesis: AAPG Bulletin, v. 90, p. 1719-1738.

Luczaj, J. A., W. B. Harrison, III, and N. S. Williams, 2006, Fractured hydrothermal dolomite reservoirs in the Devonian Dundee Formation of the central Michigan Basin: AAPG Bulletin, v. 90, p. 1787-1801.

Lundberg, J., D. C. Ford, and C. A. Hill, 2000, A preliminary U-Pb date on cave spar, Big Canyon, Guadalupe Mountains, New Mexico, USA: Journal of Cave and Karst Studies, v. 62, p. 144-148.

Machel, H. G., 1985, Cathodoluminescence in Calcite and Dolomite and Its Chemical Interpretation: Geoscience Canada, v. 12, p. 139-147.

Machel, H. G., 2004, Concepts and models of dolomitization: a critical reappraisal, *in* C. J. R. Braithwaite, G. Rizzi, and G. Darke, eds., The Geometry and Petrogenesis of Dolomite Hydrocarbon Reservoirs: Special Publications: London, Geological Society of London, p. 7-63.

Machel, H. G., and J. H. Anderson, 1989, Pervasive Subsurface Dolomitization of the Nisku Formation in Central Alberta: Journal of Sedimentary Petrology, v. 59, p. 891-911.

Machel, H. G., and E. A. Burton, 1991, Factors governing cathodoluminescence in calcite and dolomite, and their implications for studies of carbonate diagenesis, *in* C. E. Barker, and O. C. Kopp, eds., Luminescence Microscopy and Spectroscopy: Quantitative and Qualitative Aspects, v. 25.

Machel, H. G., R. A. Mason, A. N. Mariano, and A. Mucci, 1991, Causes and Emission of Luminescence in Calcite and Dolomite, *in* C. E. Barker, and O. C. Kopp, eds., Luminescence Microscopy and Spectroscopy: Qualitative and Quantitative Applications: SEPM Short Course: Dallas, Society for Economic Paleontologists and Mineralogists, p. 9-26.

Magaritz, M., R. Y. Anderson, W. T. Holser, E. S. Saltzman, and J. Garber, 1983, Isotope Shifts in the Late Permian of the Delaware Basin, Texas, precisely timed by varved sediments: Earth and Planetary Science Letters, v. 66, p. 111-124.

Malone, M. J., P. A. Baker, and S. J. Burns, 1994, Recrystallization of dolomite: evidence from the Monterey Formation (Miocene), California: Sedimentology, v. 41, p. 1223-1239.

Mathisen, M., in progress, Spatial and Temporal Evolution of the Cave Graben Fault System, Guadalupe Mountains, New Mexico, The University of Texas at Austin, Austin.

Mattes, B. W., and E. W. Mountjoy, 1980, Burial Dolomitization of the Upper Devonian Miette Buildup, Jasper National Park, Alberta, *in* D. H. Zenger, B. H. Purser, and R. L. Ethington, eds., Concepts and Models of Dolomitization: SEPM Special Publications, Society of Economic Paleontologists and Mineralogists.

Mazzullo, S. J., 1999, Paleoenvironments, Cyclicity and Diagenesis in the Outer Shelf Tansill Formation in the Carlsbad Embayment (Dark Canyon), Northern Guadalupe Mountains, New Mexico, *in* A. H. Saller, P. M. Harris, B. L. Kirkland, and S. J. Mazzullo, eds., Geologic Framework of the Capitan Reef: SEPM Special Publication: Tulsa, Society for Economic Paleontologists and Mineralogists, p. 107-128.

Meissner, F. F., 1972, Cyclic Sedimentation in Middle Permian Strata of the Permian Basin, *in* J. G. Elam, and S. Chuber, eds., Cyclic Sedimentation in the Permian Basin: Publication, West Texas Geological Society, p. 203-232.

Melim, L. A., 1991, The origin of dolomite in the Permian (Guadalupian) Capitan Formation, Delware Basin, west Texas and New Mexico: Implications for dolomitization models, Southern Methodist University, 219 p.

Melim, L. A., and P. A. Scholle, 1989, Dolomitization Model for the Forereef Facies of the Permian Capitan Formation, Guadalupe Mountains, Texas-New Mexico, Subsurface and Outcrop Examination of the Capitan Shelf Margin, Northern Delaware Basin, v. CW13, Society of Economic Paleontologists and Mineralogists (SEPM), p. 407-413.

Melim, L. A., and P. A. Scholle, 2002, Dolomitization of the Capitan Formation forereef facies (Permian, west Texas and New Mexic): seepage reflux revisited: Sedimentology, v. 49, p. 1207-1227.

Moore, G. T., and C. J. Peoples, 1990, The paleoclimate of the Kazanian (early late Permian) world: AAPG Bulletin, v. 74, p. 724.

Morse, J. W., and F. T. Mackenzie, 1990, Geochemistry of Sedimentary Carbonates: Developments in Sedimentology: Amsterdam, Elsevier Science Publishers B.V.

Mruk, D. H., 1985, Cementation and Dolomitization of the Capitan Limestone (Permian), McKittrick Canyon, West Texas, University of Colorado, Boulder, 125 p.

Mruk, D. H., 1989, Diagenesis of the Capitan Limestone, Upper Permian, McKittrick Canyon, West Texas, *in* P. M. Harris, and G. A. Grover, eds., Subsurface and Outcrop Examination of the Capitan Shelf Margin, Northern Delaware Basin: SEPM Core Workshop: San Antonio, Society for Economic Paleontologists and Mineralogists, p. 387-406.

Mutti, M., and J. A. T. Simo, 1993, Stratigraphic Patterns and Cycle-Related Diagenesis of Upper Yates Formation, Permian, Guadalupe Mountains, Carbonate Sequence Stratigraphy: Recent Developments and Applications: AAPG Memoirs, American Association of Petroleum Geologists, p. 515-534.

Mutti, M., and J. A. T. Simo, 1994, Distribution, petrography and geochemistry of early dolomite in cyclic shelf facies, Yates Formation (Guadalupian), Capitan Reef Complex, USA, *in* B. H. Purser, M. E. Tucker, and D. H. Zenger, eds., Dolomites: A Volume in Honor of Dolomieu: International Association of Sedimentologists Special Publications, Blackwell Scientific Publications, p. 91-107.

Narr, W., D. J. Fischer, P. M. Harris, T. Heidrick, B. T. Robertson, and K. Payrazyan, 2008, Understanding and Predicting Fractures at Tengiz - A Giant, Naturally Fractured Reservoir in the Caspian Basin of Kazakhstan.

Neese, D. G., 1989, Peritidal Facies of the Guadalupian Shelf Crest, Walnut Canyon, New Mexico, Subsurface and Outcrop Examination of the Capitan Shelf Margin, Northern Delaware Basin, p. 295-303.

Newell, N. D., J. K. Rigby, A. G. Fischer, A. J. Whiteman, J. E. Hickox, and J. S. Bradley, 1953, The Permian Reef Complex of the Guadalupe Mountains, Texas and New Mexico - A Study in Paleoecology.

Parsley, M. J., and J. K. Warren, 1989, Characterization of an Upper Guadalupian barrier-island complex for the middle and upper Tansill Formation (Permian), east Dark Canyon, Guadalupe Mountains, New Mexico, *in* P. M. Harris, and G. A. Grover, eds., Subsurface and Outcrop Examination of the Capitan Shelf Margin, Northern Delaware Basin: SEPM Core Workshop: Tulsa, Society of Economic Paleontologists and Mineralogists, p. 279-286.

Rahnis, M. A., and B. L. Kirkland, 1999, Distribution, Petrography, and Geochemical Characterization of Radiaxial Calcite and Associated Diagenetic Events in the Capitan Formation, West Texas and New Mexico, *in* A. H. Saller, P. M. Harris, B. L. Kirkland, and S. J. Mazzullo, eds., Geologic Framework of the Capitan

Reef: SEPM Special Publication: Tulsa, Society for Economic Paleontologists and Mineralogists, p. 175-192.

Rush, J., and C. Kerans, 2010, Stratigraphic response across a structurally dynamic shelf: the latest Guadalupian composite sequence at Walnut Canyon, New Mexico, USA: Journal of Sedimentary Research, v. 80, p. 808-828.

Saller, A. H., 1984, Petrologic and geochemical constraints on the origin of subsurface dolomite, Enewetak Atoll: An example of dolomitization by normal seawater: Geology, v. 12, p. 217-220.

Saller, A. H., P. M. Harris, B. L. Kirkland, and S. J. Mazzullo, 1999, Geologic Framework of the Capitan Depositional System - Previous Studies, Controversies, and Contents of this Special Publication, *in* A. H. Saller, P. M. Harris, B. L. Kirkland, and S. J. Mazzullo, eds., Geologic Framework of the Capitan Reef: SEPM Special Publication, Society for Economic Paleontologists and Mineralogists, p. 1-14.

Scholle, P. A., D. S. Ulmer, and L. A. Melim, 1992, Late-stage calcites in the Permian Capitan Formation and its equivalents, Delaware Basin margin, west Texas and New Mexico: evidence for replacement of precursor evaporites: Sedimentology, v. 39, p. 207-234.

Sibley, D. F., and J. M. Gregg, 1987, Classification of Dolomite Rock Textures: Journal of Sedimentary Petrology, v. 57, p. 967-975.

Smart, P., R. J. Palmer, F. Whitaker, and V. P. Wright, 1987, Neptunian Dikes and Fissure Fills: An Overview an Account of Some Modern Examples, *in* N. P. James, and P. W. Choquette, eds., Paleokarst, Springer-Verlag, p. 149-167.

Stanton, R. J., Jr., and L. C. Pray, 2004, Skeletal-carbonate neptunian dikes of the Capitan reef: Permian, Guadalupe Mountains, Texas, USA: Journal of Sedimentary Research, v. 74, p. 805-816.

Swart, P. K., 2009, Trace Elements in Carbonates, University of Miami.

Tinker, S. W., 1998, Shelf-to-Basin Facies Distributions and Sequence Stratigraphy of the Steep-Rimmed Carbonate Margin: Capitan Depositional System,McKittrick Canyon, New Mexico and Texas: Journal of Sedimentary Research, Section B: Stratigraphy and Global Studies, v. 68, p. 1146-1174.

Veizer, J., D. Ala, K. Azmy, P. Bruckschen, D. Buhl, F. Bruhn, G. A. Carden, A. Diener, S. Ebneth, Y. Godderis, T. Jasper, C. Korte, F. Pawellek, O. G. Podlaha, and H.

Strauss, 1999, $^{87}Sr/^{86}Sr$, $\delta^{13}C$ and $\delta^{18}O$ evolution of Phanerozoic seawater: Chemical Geology, v. 161, p. 59-88.

Whitaker, F., and P. Smart, 1997, Groundwater circulation and geochemistry of a karstified bank - marginal fracture system, South Andros Island, Bahamas: Journal of Hydrology, v. 197, p. 293-315.

Wildeman, T. R., 1970, The Distribution of Mn^{2+} in Some Carbonates by Electron Paramagnetic Resonance: Chemical Geology, v. 5, p. 167-177.

Ye, H., L. Royden, C. Burchfiel, and M. Schuepbach, 1996, Late Paleozoic Deformation of Interior North America: The Greater Ancestral Rocky Mountains: AAPG Bulletin, v. 80, p. 1397-1432.

Yurewicz, D. A., 1976, Sedimentology, Paleoecology, and Diagenesis of the Massive Facies of the Lower and Middle Capitan Limestone (Permian), University of Wisconsin, Madison, Madison.